Final-state effects in X-ray spectra from transition metal oxides and silicates

A thesis submitted to the College of Graduate Studies and Research

in partial fulfillment of the requirements for the

Degree of Master of Science

in the Department of Chemistry

University of Saskatchewan

Saskatoon

By

MICHAEL WILLIAM GAULTOIS

Copyright © August 2011 Michael W. Gaultois. All rights reserved.

PERMISSION TO USE

In presenting this thesis in partial fulfillment of the requirements for a Postgraduate Degree from the University of Saskatchewan, I agree that the Libraries of this University may make it freely available for inspection. I further agree that permission for copying of this thesis in any manner, in whole or in part, for scholarly purposes may be granted by the professor or professors who supervised my thesis work or, in their absence, by the Head of the Department or the Dean of the College in which my thesis work was done. It is understood that any copying or publication or use of this thesis or parts thereof for financial gain shall not be allowed without my written permission. It is also understood that due recognition shall be given to me and to the University of Saskatchewan in any scholarly use which may be made of any material in my thesis.

Requests for permission to copy or to make other uses of materials in this thesis in whole or part should be addressed to:

Head of the Department of Chemistry

University of Saskatchewan

Saskatoon, Saskatchewan S7N 5C9

Canada

~ for Sheila ~

Acknowledgement

To my family. Mum, Dad, you guys put your life on hold to raise us, so any victory of mine is yours to share. Thank you for the years of diligence, good habits, work ethic, moral code, motivation, attitude, and DNA—Mum, thanks for my mtDNA goes solely to you. Teresa and Kathryn, if you ever read this, thank you; I won't mind if you quit reading half way, or just look at the pictures.

To my friends and extended family. You sent many cards, letters, clothes, toys, and Christmas baking that kept me company during the white nights in the lab. I am only as good as the people by whom I am surrounded, and I'm grateful to have exceptional mentors, friends, and family, whether out of compassion, pity, or genetics…respectively.

To my teachers and professors of past and present. You have stimulated my curiosity, focused my thinking, and have raised me as a scientist (a Master of Science?). This victory is also yours. Andrew, in addition to putting up with my shenanigans, you have provided [much needed] guidance and direction, and have been an incredible resource through this project. You were always patiently willing to answer my many questions, and kept an eye out for me in and out of the chemistry sphere. Arthur, this magical adventure started quite some time ago. Your gentle mentorship and training provided a strong foundation for my studies and research. I am privileged to have you both as teachers and mentors. To the many other professors at the University of Alberta and University of Saskatchewan who have willingly taught me and taken interest in my well-being: I am grateful to have had the opportunity to study, learn, and fraternize, and I will represent you proudly wherever I go.

The past year and a half in Saskatoon have been fantastic, due largely in part to the great support I've had from the people around me. I thank the office and support staff in the Department of Chemistry, for making the administrative tasks feel effortless, and for keeping an eye out for me. I thank Brenda, Dwight, Cathy (and *ex officio* staff member, Doug Surtees), and Rick, who supported not only our research, but also my appetite; research is impossible on an empty stomach. I thank my colleagues, including those in Computer Science, with whom I have shared many late nights in the office.

I also thank my roommate, David Barer, a great anchor from the outside world to give perspective to my isolated, miniscule, and entirely unimportant sphere of existence. Thanks for all your support outside of the lab, for providing a great neutral perspective, and for being a *mensch*. Never having to worry about anything at home left a lot more time to focus on research. Thank you also for the pecan burgers; I never would have experienced them otherwise.

I thank my research group, with whom I spent innumerable hours (and who spent as many hours tolerating my presence). Andrew, for your patience with my hijinks and many questions, for helping with my development as a chemist, and for looking out for my best interests while I focused on research. Alina Sklad and Jessica Peddle, for being great learners, hard workers, and interesting people. James Walker, for the constant learning and interest, and the shared meals. Jessica Sigrist (and your *fiancée* Ryan), for your playful rants, your drive, your solid work ethic, and your rational judgment. John Hayes, for the many enlightening discussions and ridiculous adventures, the empathy from shared experiences, and the grandparents, but also for the beard, amazing sweaters, and general tomfoolery. Working with all of you (and your friendship) made research and grad school both exciting and enjoyable.

I thank the researchers, staff, and organizations who have supported our research. Dr. Dimitre Karpuzov is thanked for collection of XPS spectra at the Alberta Centre for Surface Engineering and Science (ACSES), and for the time he spent instructing me on the use of the Kratos instruments. Dr. Robert Gordon and the staff at PNC/XOR-CAT are thanked for their assistance collecting hard X-ray spectra at Sector 20 of the Advanced Photon Source (APS). Mr. Tom Regier and Mr. David Chevrier are thanked for their support with soft X-ray and XPS studies at SGM (11ID-1) at the Canadian Light Source (CLS). Dr. Ning Chen and Dr. Weifeng Chen are thanked for their support with hard X-ray measurements at HXMA (06ID-1) at the CLS. Dr. Lucia Zuin and Mr. Chris Ryan are thanked for their support with soft X-ray and XPS studies at PGM (11ID-2) at the CLS. Mr. Tom Bonli and Mr. Jim Rosen are thanked for their support with the XRD facilities at the University of Saskatchewan. Ms. Tanaya Smith, Ms. Jillayne Neufeld, Ms. Sandra Ribeiro, and Dr. Robert Blyth, from the CLS, are thanked for their support and for providing opportunities to share our research with the public.

Finally, I thank the funding agencies that supported our research. The Natural Sciences and Engineering Council of Canada (NSERC) is thanked for financial support in the form of a Julie Payette research scholarship. The Herzberg family and the Department of Chemistry are thanked for their financial support in the form of a Herzberg Memorial scholarship. ACSES is supported by the Canada Foundation for Innovation, the Alberta Science and Research Authority, the University of Alberta, Syncrude, and Micralyne. PNC/XSD facilities at the Advanced Photon Source, and research at these facilities, are supported by the US Department of Energy - Basic Energy Sciences, a Major Resources Support grant from NSERC, the University of Washington, Simon Fraser University and the Advanced Photon Source. Use of the Advanced Photon Source is also supported by the U. S. Department of Energy, Office of Science, Office of

Basic Energy Sciences, under Contract DE-AC02-06CH11357. The CLS is supported by NSERC, the National Research Council Canada, the Canadian Institutes of Health Research, the Province of Saskatchewan, Western Economic Diversification Canada, and the University of Saskatchewan. The Natural Sciences and Engineering Council of Canada (NSERC) supported this work through a Discovery grant to Dr. Andrew Grosvenor, and the University of Saskatchewan supported this work through a new faculty grant to Dr. Andrew Grosvenor.

All the experimental work (*e.g.*, synthesis, characterization, computer simulations, sample preparation, data collection), interpretation, and writing presented in this thesis has been done by me, except where noted otherwise. Written material was revised and edited by Dr. Andrew Grosvenor, who also provided guidance throughout the course of the work described in this thesis.

Abstract

Due to their chemical selectivity and the large amount of information that can be gained about the charge and coordination number (CN) of an element, X-ray absorption near-edge spectroscopy (XANES) and X-ray photoelectron spectroscopy (XPS) are routinely used to study metal centres in a variety of synthetic (*e.g.*, alloys, ceramics, films) and natural (*e.g.*, plants, soils) matrices. However, many competing effects influence spectral energies, and the ability to separate these effects is difficult. In particular, the effect of CN and the next-nearest neighbour (NNN) on XPS binding energies (BE) of inorganic solids have not been well-studied. In this work, the constituent elements of several industrially-relevant materials have been substituted and the resulting shifts in XPS and XANES spectral energies have been investigated, leading to a better understanding of the different effects that can cause these shifts.

With increasing Zn content in $SrFe_{1-x}Zn_xO_{3-\delta}$ ($0 \leq x \leq 1$), an oxygen-deficient perovskite-type structure, examination of Fe K- and Zn K-edge XANES spectra shows that greater oxygen deficiency (δ) lowers the transition-metal CN. Substitution of Fe by Zn results in shifts in the metal 2p XPS BEs that are much greater than the shifts observed in the corresponding $L_{2,3}$-edge XANES absorption energies. As the number of electron-rich O^{2-} anions surrounding the metal centres decreases, there is less electron density to screen the core-hole generated by XANES or XPS processes. Consequently, the poorly-screened core-hole exerts a stronger influence on the system, whose electrons relax to a greater extent. Further, O is electronegative compared to other atoms in the structure, and its tendency to tightly bind electrons restricts the ability of electrons from the material to relax around a core-hole on a metal centre. As the CN decreases, the

magnitude of final-state relaxation around the core-hole increases, lowering the final-state energy and the observed BE. When the same core-electron is excited, this effect is more pronounced in XPS than in XANES, where the excited electron partially screens the core-hole.

Investigations of $(TiO_2)_x(SiO_2)_{1-x}$ $(0 \leq x \leq 1)$, an amorphous metal-silicate, showed that the use of both hard (Ti K-edge) and soft (Ti $L_{2,3}$-edge) X-rays provides a useful way to monitor changes in the bulk and surface, respectively. The bulk and surface regimes are critical for the applications of the amorphous transition-metal silicates, which are now being used as high-κ dielectric materials for use in semiconductors. Comparison of Ti K- and $L_{2,3}$-edge spectra revealed that Ti atoms at the surface have a higher average CN than in the bulk, likely due to the presence of surface hydroxide and water groups that can coordinate to the Ti centres. The O K-edge, Ti $L_{2,3}$-edge, and Si $L_{2,3}$-edge XANES absorption energies showed little to no change with Ti content, while the O 1s, Ti 2p, and Si 2p XPS BEs were found to decrease significantly with increasing Ti content. As Ti replaces electronegative Si atoms, electrons in the material become less tightly bound and can relax to a greater extent around a core-hole. The larger degree of relaxation screens the core-hole more effectively in the final-state, lowering the final-state energy and all core-line BEs in these materials. Investigations of amorphous quaternary $[(ZrO_2)_x(TiO_2)_y(SiO_2)_{1-x-y}$ $(x + y = 0.20, 0.30)]$ and related ternary $[(ZrO_2)_x(SiO_2)_{1-x}$ $(0 \leq x \leq 1)]$ silicates found similar results. Namely, final-state relaxation increases with the amount of incorporated metal-oxide. The increase in final-state relaxation with total metal content has been confirmed empirically through analysis of the Auger parameter, which also increases with total metal content. These studies provide more examples that help us improve our understanding of the many influences that makes analysis of XPS spectra complicated, and highlight large changes in BE (>1 eV) that can occur without any changes in ground-state energies (*e.g.*, oxidation state).

Contents

1. Introduction 1

1.1. Transition metal oxides and perovskite-type structures 3
1.2. Transition metal silicates 6
1.3. X-ray photoelectron spectroscopy (XPS) 8

1.3.1. Overview 8
1.3.2. Auger emission 12
1.3.3. Sampling depth 13
1.3.4. Determining the electron binding energy (BE) 14
1.3.5. The modified charge potential model 17

1.4. X-ray absorption and near-edge spectroscopies (XAS and XANES) 19
1.5. Synopsis 27

2. Coordination-induced shifts of absorption and binding energies in the $SrFe_{1-x}Zn_xO_{3-\delta}$ system 29

2.1. Introduction 29
2.2. Experimental 31

2.2.1. Synthesis and X-ray diffraction. 31
2.2.2. Fe and Zn K-edge XANES. 32
2.2.3. Fe L_3-, Zn L_3-, and O K-edge XANES. 32
2.2.4. Fe 2p, Zn 2p, and O 1s XPS 33

2.3. Results and discussion 34

2.3.1. Structure and X-ray diffraction. 34
2.3.2. Fe and Zn K-edge XANES. 38
2.3.3. Fe L_3-, Zn L_3-edge, and O K-edge XANES 41
2.3.4. Fe 2p, Zn 2p, and O 1s XPS 46

2.4. Conclusions 49

3. XANES and XPS investigations of $(TiO_2)_x(SiO_2)_{1-x}$: the contribution of final-state relaxation to shifts in absorption and binding energies 51

3.1. Introduction 51
3.2. Experimental 53

3.2.1. Synthesis of $(TiO_2)_x(SiO_2)_{1-x}$ 53
3.2.2. XANES 54
3.2.3. XPS 56
3.3. Results and Discussion 56
3.3.1. Ti K-edge XANES 56
3.3.2. Ti $L_{2,3}$-edge XANES 61
3.3.3. XPS 62
3.3.4. XANES vs. XPS 68
3.4. Conclusions 70
4. XPS investigations of final-state relaxation in amorphous Zr and Zr/Ti silicate powders 72
4.1. Introduction 72
4.2. Experimental 74
4.2.1. Synthesis of $(ZrO_2)_x(SiO_2)_{1-x}$ and $(ZrO_2)_x(TiO_2)_y(SiO_2)_{1-x-y}$ 74
4.2.2. XANES 75
4.2.3. XPS 77
4.2.4. Electronic structure calculations 78
4.3. Results and discussion 81
4.3.1. Transition metal K-edge XANES 81
4.3.2. Zr $3d_{5/2}$, Ti $2p_{3/2}$, Si 2p, and O 1s XPS binding energy (BE) shifts 84
4.3.3. Ti $L_{2,3}$-, Si $L_{2,3}$-, and O K-edge XANES 90
4.3.4. Identifying the cause of XPS BE shifts 99
4.3.5. The Auger parameter 101
4.4. Conclusions 108
5. Conclusions 109
5.1. Summary 109
5.1.1. The effect of coordination number 109
5.1.2. Structural studies of transition metal silicates 111
5.1.3. Next-nearest neighbour (NNN) effects and electronegativity 113
5.1.4. Significance and implications 115
5.2. Directions for future research 116
6. References 121

List of Figures

Figure 1.1. (a) The ABX_3 perovskite-type structure and (b) examples of distortion. 2

Figure 1.2. Diagram of an XPS spectrometer. 9

Figure 1.3. Representative XPS (a) survey and (b) core-line spectra. 10

Figure 1.4. (a) Photoemission and the subsequent (b) fluorescence and (c) Auger decay. 11

Figure 1.5. XPS energy diagram. 16

Figure 1.6. Typical experimental setup for XAS. 20

Figure 1.7. Representative transition metal K-edge (a) XAS and (b) XANES spectra. 23

Figure 1.8. XANES energy diagram.. 28

Figure 2.1. Unit cell constants as a function of Zn content in $SrFe_{1-x}Zn_xO_{3-\delta}$. 35

Figure 2.2. The crystal structures of (a) $SrFeO_{2.75}$ (*Cmmm*) and (b) $SrZnO_2$ (*Pnma*), end-members in the $SrFe_{1-x}Zn_xO_{3-\delta}$ system,..... 36

Figure 2.3. (a) Fe and (b) Zn K-edge spectra from $SrFe_{1-x}Zn_xO_{3-\delta}$ 37

Figure 2.4. (a) Fe L_3-, (b) Zn L_3-, and (c) O K-edge spectra from $SrFe_{1-x}Zn_xO_{3-\delta}$. 40

Figure 2.5. High resolution core-line (a) Fe $2p_{3/2}$, (b) Zn $2p_{3/2}$, and (c) O 1s XPS spectra from $SrFe_{1-x}Zn_xO_{3-\delta}$. 44

Figure 2.6. Shifts in (a) the XANES absorption energies and (b) XPS BEs with increasing Zn content in $SrFe_{1-x}Zn_xO_{3-\delta}$. 45

Figure 3.1. Ti K-edge (a,b) and Ti L_3-edge (c,d) XANES spectra of $(TiO_2)_x(SiO_2)_{1-x}$. 60

Figure 3.2. High resolution core-line (a) O 1s, (b) Si 2p, and (c) Ti $2p_{3/2}$ XPS spectra of annealed $(TiO_2)_x(SiO_2)_{1-x}$. 64

Figure 3.3. Si $2p_{3/2}$, Ti $2p_{3/2}$, and O 1s binding energy shifts with increasing Ti content (x) in $(TiO_2)_x(SiO_2)_{1-x}$. 65

Figure 3.4. (a) O K- and b) Si $L_{2,3}$-edge XANES spectra of annealed $(TiO_2)_x(SiO_2)_{1-x}$ materials. 67

Figure 4.1. Ti (a, b) and Zr (c, d) K-edge spectra from $(ZrO_2)_x(TiO_2)_y(SiO_2)_{1-x-y}$ with a fixed total metal content (x + y) of 20 mol % (a, c) and 30 mol % (b, d). 79

Figure 4.2. (a) Ti K- and (b) Zr K-edge edge spectra of $(ZrO_2)_x(TiO_2)_y(SiO_2)_{1-x-y}$ with increasing *total* metal content..... 80

Figure 4.3. (a) Zr 3d and (b) Ti $2p_{3/2}$ XPS core-line spectra of the quaternary silicates and binary oxides. 85

Figure 4.4. (a) Si 2p and (b) O 1s XPS core-line spectra of the quaternary silicates and binary oxides. 86

Figure 4.5. Binding energy of the photoelectron peak maximum as a function of total metal content (mol % ZrO_2 + TiO_2) in quaternary silicates. 87

Figure 4.6. (a) Ti $L_{2,3}$-edge and (b) Si $L_{2,3}$-edge spectra of the quaternary silicates..... 92

Figure 4.7. Si K-edge spectra of annealed $(TiO_2)_x(SiO_2)_{1-x}$ materials. 94

Figure 4.8. (a) O K-edge spectra of quaternary silicates and (b) the first derivative with respect to energy. (c) The calculated electronic DOS. 97

Figure 4.9. (a) O K-edge spectra of the Zr ternary silicates and (b) the first derivative with respect to energy. 98

Figure 4.10. O KLL Auger spectra from (a) quaternary and (b) Zr ternary silicates. 105

Figure 4.11. (a) O KLL Auger peak maxima and (b) Auger parameters of the quaternary and Zr ternary silicates.. 106

Figure 4.12. Plots of XANES absorption energies and XPS BEs for transitions with identical ground-state energies. 107

List of abbreviations and selected symbols

APS	Advanced Photon Source
BE	Binding energy
CLS	Canadian Light Source
CMOS	Complementary metal-oxide–semiconductor
CN	Coordination number
EDTA	Ethylenediaminetetraacetic acid
E^{EA}	Extra-atomic relaxation energy
Eq.	Equation
eV	Electron volt
EXAFS	Extended X-ray absorption fine-structure
FLY	Fluorescence yield
FTIR	Fourier transform infrared
HXMA	Hard X-ray Micro-Analysis
KE	Kinetic energy
LMTO	Linear muffin-tin orbital
MIEC	Mixed ionic-electron conduction
NMR	Nuclear magnetic resonance
NN	Nearest neighbour
NNN	Next-nearest neighbour
SGM	Spherical Grating Monochromator

SOFC	Solid oxide fuel cell
TEOS	Tetraethyl orthosilicate
TEY	Total electron yield
TM	Transition metal
UHV	Ultra-high vacuum
VLS PGM	Variable Line Spacing Plane Grating Monochromator
XANES	X-ray absorption near-edge spectroscopy
XAS	X-ray absorption spectroscopy
XPS	X-ray photoelectron spectroscopy
XRD	X-ray diffraction
YSZ	Yttira-stabilized zirconia
κ	Dielectric constant
χ	Electronegativity

Chapter 1

1. Introduction

The rational design of materials requires a deep understanding of structure-property relationships, which can be acquired through studies using mature and robust spectroscopic techniques. X-ray spectroscopy is particularly effective for these studies, as it can be used to characterize both the physical structure (*i.e.*, coordination environment) and electronic structure (*i.e.*, energies of core and valence electrons, and/or bonding interactions).[1, 2] X-ray absorption and photoelectron spectroscopies (XAS and XPS) involve the excitation of core electrons, and the energy required for these excitation processes is sensitive to the local chemical environment around an element of interest. In general, the spectral energies are the result of ground state (before excitation) and final state (after excitation) effects, and although these techniques and the underlying theory have developed considerably, there continue to be factors whose effects remain poorly understood and merit further study.

In this work, subtle and controlled changes in model systems, oxygen-deficient perovskite-type structures (Chapter 2) and transition metal silicates (Chapters 3 and 4), are used to understand finer spectral energy changes in X-ray absorption and photoelectron spectra. These model systems have a wide range of compositions where substitution leads to well-defined structural changes. This provides an opportunity to isolate specific changes in structure and composition, which is crucial to determining the underlying cause of spectral energy shifts.

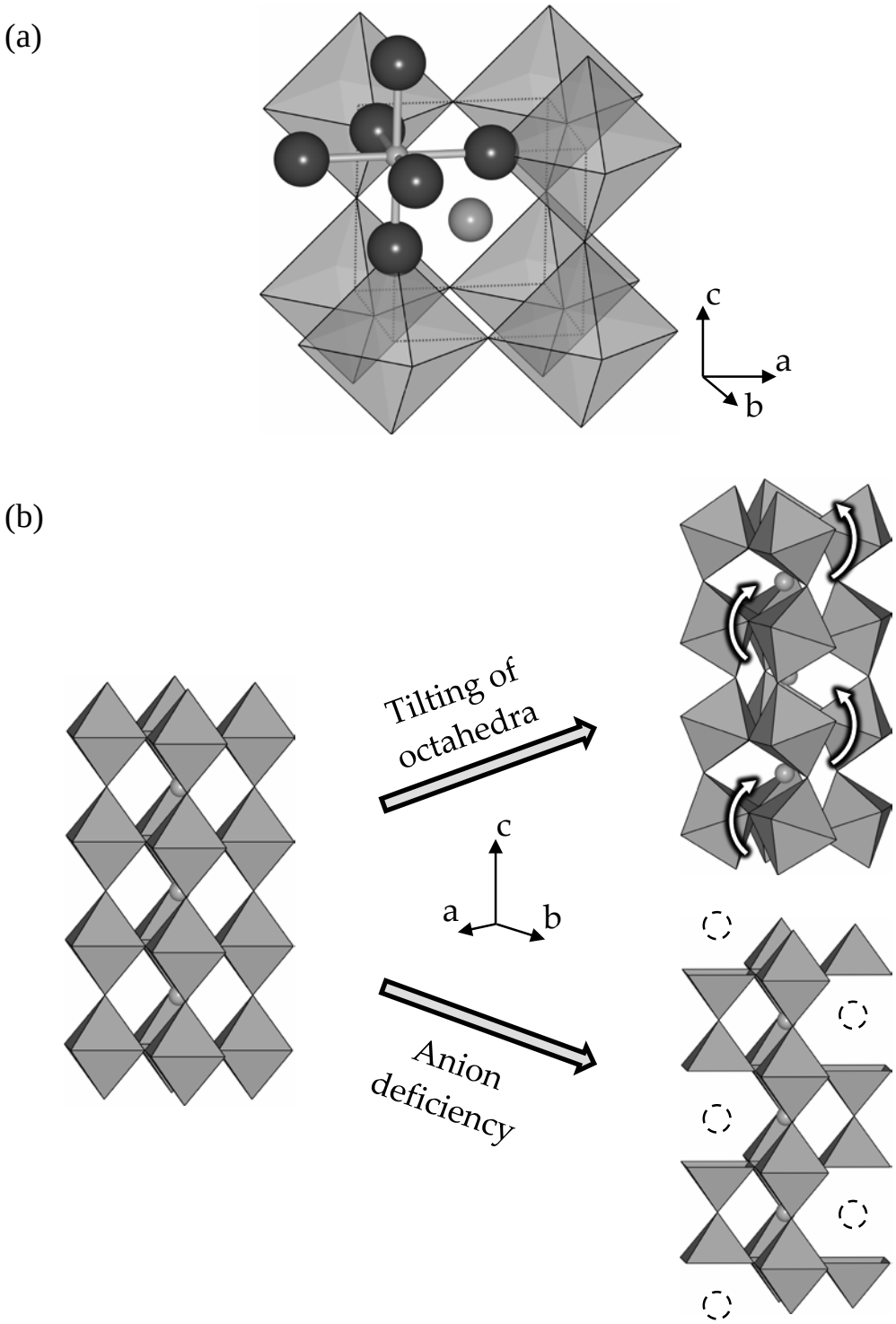

Figure 1.1. (a) The ideal ABX_3 perovskite-type structure consists of a 3-dimensional framework of corner-sharing BX_6 octahedra centered on corners of the cubic unit cell and A cations in interstitial positions. All B-X-B bond angles are 180° to each other and all B-X bond lengths are equidistant. (b) Tilting of the octahedra (top) and anion deficiency (bottom) are possible distortions of perovskite-type structures. Anion vacancies are represented by dashed-line circles.

1.1. Transition metal oxides and perovskite-type structures

Transition metal oxides are a diverse class of materials bestowed with properties that make them desirable for technological applications.[3] Compared to compounds without transition metals, the partially filled d-states of transition metals frequently lead to a more complex electronic structure, which is often accompanied by interesting properties. Accordingly, transition metal oxides have a long history of scientifically interesting features and industrial applications, as well as an abundance of phenomena that have yet to be fully understood or mastered, such as high-temperature superconductivity, half-metallicity, metal-insulator transitions, ion-conduction, magnetic ordering, and the coupling of magnetic and electric properties.[3-13]

Metal oxides have a wide range of structures, but perhaps the most recognized is the perovskite-type structure, which follows the general formula ABX_3. In this notation, A is usually a large electropositive cation, B is often a transition metal cation, and X is predominantly an oxygen anion, though the X site can be partially or fully substituted by other anions such as fluoride or sulphide.[14, 15] As shown in **Figure 1.1a**, the ideal perovskite-type structure is cubic and consists of a 3-dimensional framework of corner-sharing BX_6 octahedra, with A cations located in interstitial positions. All B-X-B bond angles are 180° to each other and all B-X bond lengths are equidistant.[14-16] However, the structure can tolerate substantial distortion, and this flexibility allows the structure to accommodate a wide range of atoms with different size and valence. These modifications often involve tilting of the BX_6 octahedra, displacement of the B cations within the octahedra, and anion (X) deficiency, all of which reduce the symmetry of the structure (**Figure 1.1b**).[9, 14-18] Distorting the structure and/or reducing the symmetry are often desirable, as they introduce complexity and are frequently accompanied by new properties. For

example, anion-deficiency can lead to ion conduction, while tilted BX_6 octahedra and displaced B cations can produce non-centrosymmetric structures required for ferroelectricity, piezoelectricity, and second harmonic generation.[3, 9, 19-23]

Perovskite-type oxides can easily be made by direct methods (also called the ceramic method), where powdered binary oxides are mixed together and heated at high temperatures over extended periods.[15] Sol-gel syntheses have also been successfully employed and have been shown to provide superior control of particle size, which is important for applications involving ion conduction through the material.[24, 25] As a result of the compositional tolerance and ease of synthesis, the perovskite-type structure has become one of the most well-studied structure-types. Further, the structure is easily tuneable through changes in composition or synthetic conditions, so it is often used to investigate the complex relationship between structure, composition, and physical properties.[15, 18] This has allowed the rational design of materials with desirable properties, tailored to particular applications and devices: capacitors, signal transducers, high-temperature superconductors, resistors, ion conductors, and gas sensors, among many others.[15]

One phenomenon being actively investigated through perovskite-type oxides is solid-state ion conduction (also called mixed ion-electron conduction, or MIEC).[3, 26] Although solids are typically considered to be static, sodium ions incorporated in β-Al_2O_3 *at room temperature* show the same ionic conductivity as a 0.1 M NaCl solution.[3] Meanwhile, β-Al_2O_3 retains all the mechanical properties associated with a conventional ceramic, such as hardness, durability, chemical inertness, and retention of structural integrity at high temperatures. In industrial applications, lithium-ion conduction has been central to lithium-ion and lithium-polymer batteries, while oxide anion conduction is critical to solid oxide fuel cells (SOFC) and electrodeless catalysts.[3, 26, 27] Recent investigations of oxygen-deficient perovskite-type phases

have shown high oxygen fluxes, making them viable replacements for yttria-stabilized zirconia (YSZ), which has been the standard for many years.[9, 26-30]

Oxygen-deficient perovskite-type structures are non-stoichiometric perovskite-type oxides of the form $ABO_{3-\delta}$, where δ is the degree of oxygen deficiency. As before, A is a large electropositive cation, whereas B tends to be a smaller cation (and is often a transition metal). In the structure, the oxygen deficiency is derived by removing O atoms from the structure. Synthetically, the oxygen deficiency varies with temperature, partial pressure of oxygen (pO_2), and substitution of the A or B sites.[9] If the oxygen vacancies are randomly distributed, a disordered structure results. However, vacancy ordering can occur, and is favoured as δ increases.[9, 31, 32] In many cases, the perovskite-type structure can tolerate a substantial oxygen deficiency, often up to ~15 mol %, before it undergoes a phase transformation to a brownmillerite-type structure where the oxygen vacancies are ordered.[9, 32] The brownmillerite-type structure, of the form $A_2B_2O_5$ ($ABO_{2.5}$), can be derived by removing 1/6 of the O atoms (16.7% deficiency) from the ABO_3 perovskite-type structure, creating alternating layers of BO_4 tetrahedra and BO_6 octahedra.[9, 32]

Although many ceramics (processed inorganic solids) were first found as minerals in nature, rationally designed synthetic ceramics are now commonplace. As mentioned in the opening, this logical design of materials with application-tailored properties is possible due to knowledge of structure-property relationships. In this work, the subtle and controlled changes in perovskite-type structures are used to understand some of the finer spectral energy changes in X-ray absorption spectroscopy (XAS) and X-ray photoelectric spectroscopy (XPS).

1.2. Transition metal silicates

Silicates are a broad class of materials that contain Si bound to anions. The most commonly featured anion is oxygen, where an extended structure is composed of SiO_4 subunits.[33] These tetrahedral subunits can order to give isolated tetrahedra, pairs, rings, chains, sheets, or 3-dimensional networks.[33] Due to the many possible motifs of these tetrahedral SiO_4 building blocks, silicates are usually classified by the ordering of these subunits within the crystal structure. The most well-known member, silica (SiO_2), is colloquially referred to as "glass," though most glasses contain a number of other additives.

Although SiO_2 is more well-known for its chemical and physical durability, it has played a vital role in the semiconductor industry, where it is grown on Si substrates by oxidation of Si to create an electrically insulating and polarizable layer (*i.e.*, a dielectric layer).[34, 35] However, the progressive reduction in the size of transistors is limited by the dielectric constant of SiO_2. (The dielectric constant is a measure of the relative permittivity of a material and its ability to attenuate electromagnetic fields, so a large dielectric constant is desirable to achieve a high capacitance or serve as an electrically insulating layer.[36-38]) As gate dielectric stacks in complementary metal-oxide–semiconductor (CMOS) devices shrink in size, the SiO_2 dielectric layer thickness can only shrink to a fundamental limit, beyond which electron tunnelling leads to a leakage current that deleteriously affects device reliability.[34, 39, 40] To overcome this fundamental limit, materials with a higher dielectric constant are required, while being compatible with current manufacturing processes. The dielectric constant is material-specific, so there has been a flurry of activity in search of a suitable candidate to replace SiO_2, and incorporation of Hf has led to the creation viable devices.[35, 41] Introducing transition metals into silicates often imparts useful properties, and in the case of SiO_2, the substitution of some Si sites

with Ti, Zr, or Hf increases the dielectric constant by up to an order of magnitude.[42-45] Unfortunately, phase segregation is problematic for metal silicates, especially with higher metal content. For example, annealing (*i.e.*, heating at elevated temperatures), a routine technique in semiconductor fabrication and industrial processing, can easily cause the formation of ordered metal-rich domains, leading to heterogeneity when higher metal contents are used.[39, 44, 46, 47] Heterogeneity changes the properties of the material and can deleteriously affect device reliability, particularly with films.[39] For other applications, silicates have traditionally been made by a melt synthesis, where they are rapidly cooled from high temperatures.[33, 48, 49] However, transition-metal (*e.g.*, Ti, Zr, Hf) silicates have high melting points that make this processing unfeasible, and crystallization is favoured at high temperatures.[46, 48, 49] "Soft" methods such as sol-gel routes have overcome these difficulties, and have the added benefit of a range of post-synthetic solution processing techniques, such as spin-coating for thin-film applications or fibre drawing and spinning for use in composites or textiles.[50-52]

Industrial applications, particularly electronics, require homogeneous products with well-defined properties. To investigate the structure and homogeneity of materials, X-ray diffraction (XRD) is traditionally used, but it depends on long-range order.[53] Lack of long-range order in amorphous systems, such as silicate thin-films used in electronics, prevents examination by diffraction-based techniques, so structural information must be obtained by other means. Disordered systems such as these amorphous metal silicates are ideal candidates for study by X-ray spectroscopy, which requires no long-range order because it is sensitive to the first few coordination shells of the element being examined. XPS is one such technique that is routinely used to characterize these materials, and shifts in spectral energies have been observed with increasing metal content.[54, 55] However, the origin of these shifts has been debated and remains

unclear.[54, 55] In this work, the structural tolerance of the SiO_2 glass network and the large substitutional range in the $(TiO_2)_x(SiO_2)_{1-x}$, $(ZrO_2)_x(SiO_2)_{1-x}$, and $(ZrO_2)_x(TiO_2)_y(SiO_2)_{1-x-y}$ systems have been exploited to create an isostructural series with varying metal content. This series has been examined by several spectroscopic techniques to determine the contributing factors of the energy shifts in XPS, toward the goal of better understanding and describing material changes investigated by XPS.

1.3. X-ray photoelectron spectroscopy (XPS)

1.3.1. Overview

X-ray photoelectron spectroscopy (XPS) is a spectroscopic technique that yields elemental and chemical state information of surfaces by exploiting the photoelectric effect: when a material is irradiated with photons of sufficient energy, electrons are ejected (called *photoelectrons*) whose kinetic energies (KE) are determined by the energy of the incident photons ($h\nu$) and the identity and chemical environment of the atoms in the material.[2, 56] As shown in the diagram of a typical XPS instrument (**Figure 1.2**), photoelectrons are emitted into vacuum and pass through an energy analyzer to reach a detector, after which a spectrum of electron intensity as a function of KE is constructed. The KE of a photoelectron is given by eq. (1.1), where hν is the incident photon energy, BE is the binding energy of the electron examined, and ϕ is the work function of the sample, which is a material-specific measure of the energy required to liberate an electron from the surface of a solid.[2, 56]

$$KE = h\nu - BE - \phi \qquad (1.1)$$

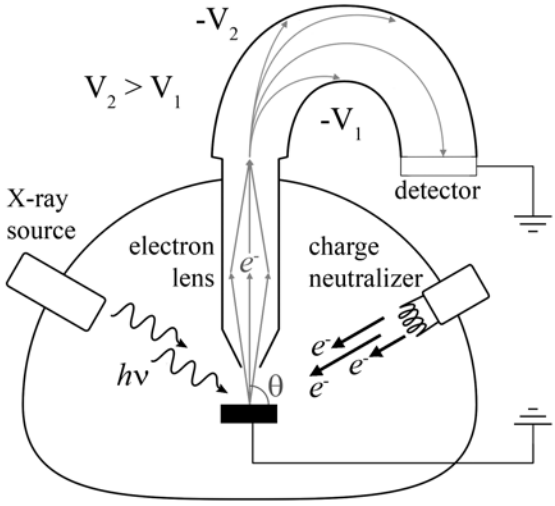

Figure 1.2. An XPS spectrometer generally consists of a chamber under ultra-high vacuum ($<10^{-9}$ Torr), a monochromatic X-ray source, a charge neutralizer, an electron lens, an energy analyzer, and a detector that is electrically coupled to the sample stage. θ is the take-off angle, which can be adjusted by changing the orientation of the sample with respect to the electron lens. In a hemispherical analyzer, only electrons with a specific range of energies will reach the detector. V_1 and V_2 are applied negative potentials, where $|V_2| > |V_1|$, forcing electrons around an arc toward the detector. Electrons with too high or low KE will collide against the outer or inner wall of the analyzer, respectively.

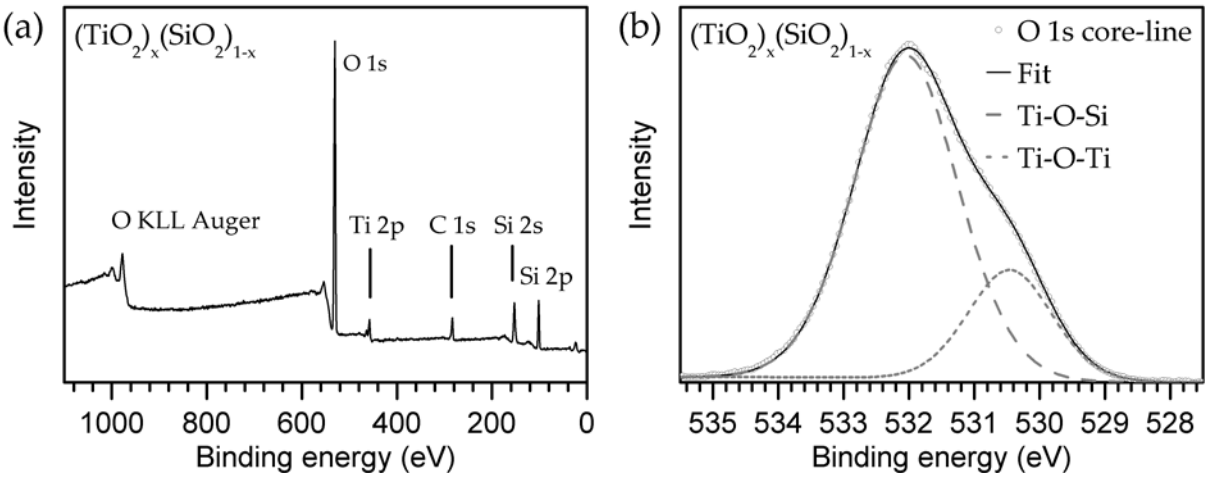

Figure 1.3. (a) A representative XPS survey spectrum of $(TiO_2)_x(SiO_2)_{1-x}$, with peaks labelled to indicate the transition responsible for the emission. The peak intensities can be used to determine elemental composition. The stepped background is caused by inelastic scattering of electrons travelling through the material before reaching the surface. (b) A representative XPS O 1s core-line spectrum from the same sample. Synthetic peaks (long-dashed lines) have been fitted to show the different O chemical environments. When O is surrounded by more electropositive Ti atoms (compared to Si), the O 1s BE is lower (short-dashed line). Measured data points are shown as circles, and the solid line is the spectrum generated from the synthetic peaks.

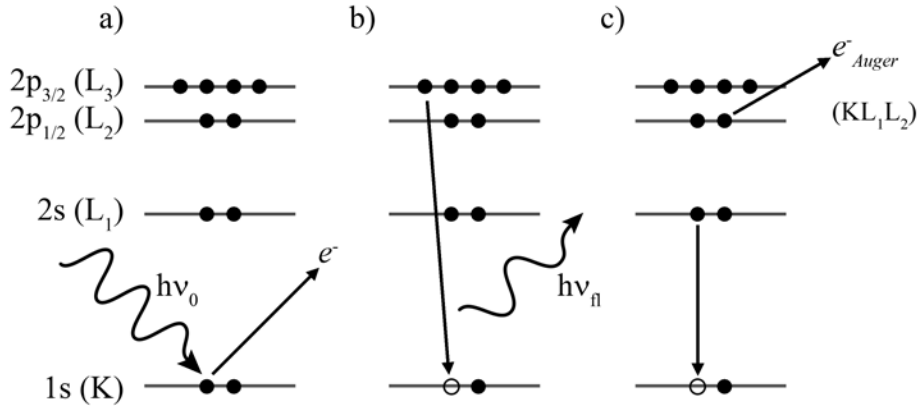

Figure 1.4. If an atom absorbs an incident photon with sufficient energy, bound electrons in core shells can be ejected from the absorbing atom. (a) Absorption of the incident photon produces a photoelectron and a core hole, which can decay by emission of (b) a photon (fluorescence) or (c) an electron (Auger emission).

Depending on the information needed, different regions of interest in an XPS spectrum are examined. To quantify elemental composition, "survey" spectra are collected with a wide energy window and a coarse step size (*e.g.*, a 1000 eV window sampled every 1 eV; **Figure 1.3a**), while core-line scans with a narrow energy window and a finer step size (*e.g.*, a 10 eV window sampled every 0.05 eV; **Figure 1.3b**) are used to determine more subtle chemical state information, such as the oxidation state of the absorbing atom and the identity of coordinating ligands. Although the electron analyzer detects the KE of photoelectrons, conversion from KE to BE can be achieved by trivial rearrangement of eq. (1.1). Whereas the KE of an emitted photoelectron depends on the energy of the incident photon, the BE of an electron is characteristic of its atomic energy level and parent element, and is an intrinsic property of a material.[56] For these reasons, XPS spectra are often plotted on a BE scale.

1.3.2. Auger emission

Analysis of the photoelectron peak BEs can reveal the electronic structure of a material. However, there are additional processes accompany the ejection of a photoelectron, and these can be used to gain more information about a system of interest. When a photoelectron is ejected from a core shell, the atom is ionized and a core-hole is produced. The core-hole that is produced is unstable, and rapidly decays by either fluorescence or Auger processes, shown schematically in **Figure 1.4**.[57] In both processes, an electron from a higher-energy state fills the core-hole, and the difference in energy after this decay process (the stabilization energy) is released from the system. The decay products that carry this energy distinguish the two processes. In fluorescence, a photon is emitted with a frequency that depends on the stabilization energy, and the atom is left with a hole further from the core. In an Auger process, an electron is emitted whose KE depends on the stabilization energy, after which the atom is left with two holes further from the core (a

doubly-ionized state).[56, 58] The emitted Auger electron can be subsequently analyzed and detected in an XPS spectrometer by the same means as the primary photoelectron.[2, 56]

$$KE_{Auger} = E_{\mathrm{C}} - E_{\mathrm{V}} - E_{\mathrm{V}'} - \phi \qquad (1.2)$$

Auger energies can be described approximately by the difference in the energies of the orbitals involved in the decay process, eq. (1.2), although it is recognized that more complicated factors such as many-body effects and relaxation influence the Auger energies.[58-60] (The sample work function, ϕ, accounts for the amount of energy required to remove the electron from the material, and its contribution can be removed by methods described in Section 1.3.4.) Whereas the KE of a primary photoelectron is proportional to the incident photon energy, the KE of an Auger electron is independent of the excitation energy, so Auger peaks are always treated on a KE scale. As can be seen in **Figure 1.4c**, three energy levels are involved in a given Auger process, so Auger peaks are identified with three orbital definitions (sometimes two of these levels, V and V', are identical). In the notation used here, C is the orbital of the core-hole being filled, V is the initial orbital of the relaxing electron, and V' is the orbital from where the Auger electron is emitted.

1.3.3. Sampling depth

All of the information that can be obtained through the analysis of photoelectrons or Auger electrons is restricted to atoms near the surface of the sample (nm scale), which may not be in the same chemical environment as in the bulk (μm scale).[56, 61] Differences in the bulk and surface chemical environment could be due to surface reconstruction, surface adsorbates or oxides, or incomplete coordination spheres at the surface. The incident photons that excite the sample are often high energy (*e.g.*, Al Kα radiation, 1486.7 eV), and are able to penetrate into the bulk of the material.[56] However, electrons with the same or lesser energy interact more strongly

with matter, so they are more likely to be inelastically scattered and/or absorbed by the material (*i.e.*, the electron-electron scattering cross-section is much larger than the photon-electron scattering cross-section).[62-64] For this reason, XPS is inherently surface sensitive, with a sampling depth less than 10 nm.[56] (The sampling depth is commonly defined as the depth up to which 95% of the detected electrons originate.[56])

1.3.4. Determining the electron binding energy (BE)

The binding energy (BE) of an element within a material is a valuable probe of its chemical environment. By comparison to reference materials, and especially within a series of similar compounds, the shift in the BE can be a powerful tool to examine changes in the electronic structure.[56] This, in turn, can be used to understand how the system changes when a stress is applied, such as a change in structure or in composition. Rearrangement of eq. (1.1) yields the expression for the electron BE, shown in eq. (1.3).

$$BE = h\nu - KE - \phi \qquad (1.3)$$

All energies of solids are defined relative to the Fermi level of a material, which is taken to be zero (*i.e.*, $E_{Fermi} = 0$). (The Fermi level for electrical conductors (*i.e.*, metals) is defined as the highest occupied energy state at absolute zero, and is often defined as the mid-point of the band gap for semiconductors and insulators.)[56, 62, 65] In this context, the BE of an electron is the amount of energy necessary to promote the electron from its ground-state energy (*i.e.*, from a core orbital) to the Fermi level. However, the electron at the Fermi level still experiences an attractive potential from the solid and requires additional energy to be liberated from the surface. This energy barrier is the work function of a material, ϕ, which is the amount of energy required to bring an electron from the Fermi level to a point where the electron is no longer bound to the

solid (*i.e.*, it is at the vacuum energy level, E_{vac}), usually >100 Å.[62, 65] An energy diagram is provided to help visualize the energy levels previously described (**Figure 1.5**).

As shown in eq. (1.3), the measured BE depends on ϕ, the sample work function, which is specific to a material and generally unknown. However, if the sample is electrically conductive, it can be electrically connected (*i.e.*, grounded) to the spectrometer, which aligns their Fermi levels and removes the dependence on the *sample* work function.[2, 56] Instead, the measured BEs depend on the *spectrometer* work function, $\phi_{\text{spectrometer}}$, as shown in eq. (1.4). This term is relatively static, and can be found through the use of conductive standards with well-known BEs (*e.g.* Au metal).[2, 66-69] A bias is then added to the detector to remove the contribution of the spectrometer work function, and the expression for the BE of an electron simplifies to eq. (1.5).

$$BE = h\nu - KE - \phi_{\text{spectrometer}} \quad (1.4)$$

$$BE = h\nu - KE \quad (1.5)$$

Although this adequately describes the situation for electrical conductors, insulators make analysis more difficult. If the sample is an insulator, the surface of the sample will not be electrically grounded to the spectrometer and will not recover all of the electrons lost through emission. As a result, the surface of the material becomes electron-deficient and positively charged; electrons become more attracted to the surface and more difficult to remove.[56] For semiconductors and weak insulators, uniform charging can often be overcome with a technique known as charge neutralization, where many low-energy electrons are directed toward the material.[2, 55, 56] These electrons are able to replenish the electrons being lost from the material, which is often effective at reducing the effect of charging. One of the many ways electrons can

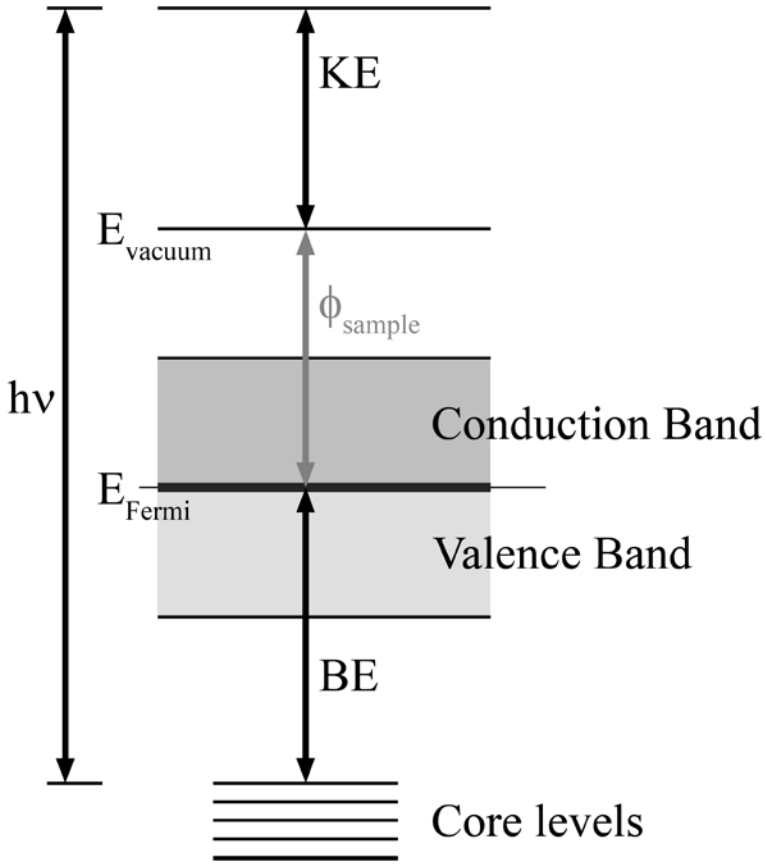

Figure 1.5. An energy diagram showing the relationship between the excitation energy (*hν*), binding energy (BE) of core electrons, the sample work function (ϕ_{sample}), and the KE of the emitted photoelectron.

be generated is through thermionic emission from a tungsten filament, after which an electric field is used to direct the electrons toward the sample being analyzed.[70]

Once spectra are collected, energy referencing or calibration can be done using internal or external standards with known core-line energies. Since the potential generated by uniform charging affects all BEs equally, all spectra for a sample can be shifted by the appropriate amount if the BE shift of the internal standard is known. Fortunately, most samples are contaminated with adsorbed hydrocarbons that, although present in only small concentrations, are detectable by XPS.[56, 71] This carbon contamination (called adventitious carbon) is unavoidable, even under ultra-high vacuum (UHV), and frequently arises from desorption of adsorbates from the instrument chamber walls. A common practice for conductive or insulating samples is to calibrate a set of core-line spectra from a sample by setting the C 1s photoelectron peaks from adventitious carbon to the accepted value of 284.8 ±0.2 eV.[55, 56, 71]

1.3.5. The modified charge potential model

One of the great strengths of XPS is that it can obtain information about chemical states. The binding energy (BE) of an XPS core-line is influenced by the chemical environment, and this superficial analogy to proton-based nuclear magnetic resonance (^{1}H NMR) spectroscopy led to a BE shift in XPS also being called a *chemical shift*.[72] As the electron density around a given atom being probed increases, the effective nuclear charge decreases due to screening by the electrons. As a result, the electrons around the atom experience less attraction and are easier to remove (*i.e.*, have a lower BE). XPS BEs are sensitive to the chemical environment because they are related to the interactions between the atom of interest and its first coordination shell, that is, its nearest neighbour atoms. Longer-range interactions with more distant atoms can also influence these energies, though these effects are often much less pronounced.[56, 73] The observed

binding energy of a photoelectron from atom *i*, E_i, which results from both ground- and final-state energies, can be described by the modified charge potential model.[2, 56, 74] Although final-state effects were initially ignored because their contribution was believed to be minor, it is now recognized that final-state effects can be major contributors to an observed shift in BE.[56, 74, 75] Relative to the element in a reference compound (*e.g.*, the elemental form), E_i^0, a shift in BE of atom *i*, ΔE_i, is described by eq. (1.6).[56]

$$\Delta E_i = E_i - E_i^0 = (k\Delta q_i + \Delta \sum_{\mathrm{i}\neq\mathrm{j}} \frac{q_j}{r_{ij}}) - (\Delta E_i^{\mathrm{IA}} + \Delta E_i^{\mathrm{EA}}) \qquad (1.6)$$

A shift in binding energy results from both ground- and final-state effects, which are shown in this order and separated by parentheses in eq. (1.6). Shifts in the ground-state energies are caused by changes in the charge of the atom (*i*) being excited (q_i in $k\Delta q_i$, where *k* is a parameter that describes the Coulombic interaction between core and valence electrons) and the chemical environment ($\Delta \sum_{\mathrm{i}\neq\mathrm{j}} \frac{q_j}{r_{ij}}$, where r_{ij} is the distance to atom *j*, which has a charge of q_j).[2, 56, 74-76] These are intra- and extra-atomic effects, respectively. In the final state, after a photoelectron has been ejected from atom *i* and an unscreened core-hole has been produced, the system will rearrange its remaining electrons to minimize its energy. In the presence of the newly-created attractive potential, the electrons in the system *relax* towards the core-hole. Extra-atomic relaxation (ΔE_i^{EA}) of electrons from surrounding atoms is sensitive to changes in the chemical environment, whereas intra-atomic relaxation (ΔE_i^{IA}) of electrons localized on the atom of interest is not, so ΔE_i^{IA} is often negligible.[56]

$$\alpha' = \mathrm{KE} + \mathrm{BE} \qquad (1.7)$$

Separation of these initial- and final-state effects requires complimentary techniques, and can be quite involved when many variables are changing in a material. One way to separate the

contributions from initial- and final-state effects is to look at the Auger parameter. If a core-line photoelectron peak and an Auger peak are accessible for the same element, the photoelectron BE and the Auger KE can be combined, as shown in eq. (1.7), to obtain the Auger parameter, α'. The Auger parameter can be used to obtain information about the chemical state and chemical environment of an element within a material, but it also provides one of the few experimental measures of changes in extra-atomic final-state relaxation, ΔE_i^{EA}, for which it is used in Chapter 4.[77] Another technique that can help resolve contributions to BE shifts is X-ray absorption near-edge spectroscopy (XANES), which will be discussed in the next section. XANES absorption energies shift in a similar fashion to XPS BEs, though, as the excited electron is not removed completely from the system, contributions from final-state effects tend to be muted.[54, 78-81]

1.4. X-ray absorption and near-edge spectroscopies (XAS and XANES)

XAS is another powerful technique that is routinely used to study chemical states in a variety of synthetic (*e.g.*, alloys, ceramics, films) and natural (*e.g.*, plants, soils) matrices.[82, 83] This is largely due to the elemental selectivity and the information that can be gained about the charge and coordination number (CN) of an element.[84] The CN of metal centres in structures often has a large influence on properties, so spectroscopic probes that can examine the CN are a valuable tool. For example, in oxygen-deficient perovskite-type structures (such as the $SrFe_{1-x}Zn_xO_{3-\delta}$ system investigated in Chapter 2), the ion conduction is strongly dependent on the oxygen-deficiency (δ), which can be probed by looking at the CN of the metal centres bound to oxygen.[9] Further, the use of penetrating, high energy X-rays—also called "hard" X-rays—often allows *in situ* measurements to be performed, such as monitoring the oxidation state of a working catalyst.[85, 86]

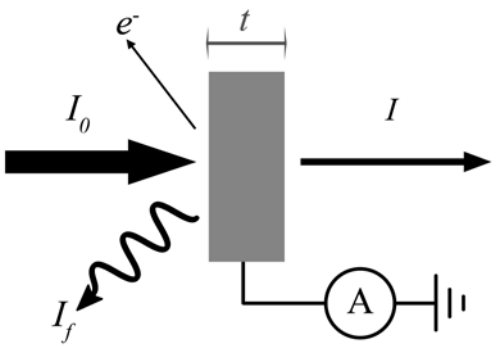

Figure 1.6. A typical experimental setup for XAS where a sample of thickness *t* is irradiated with an incident X-ray beam with intensity I_0. Promotion of a core electron creates an unstable core hole, which quickly decays by emission of photons (I_f) and electrons (e^-). These decay products, or the intensity of the transmitted beam (I), can be monitored to determine the change in the absorption coefficient as a function of energy. The flux of emitted electrons can be monitored by measuring the drain current (A) required to replace ejected electrons.

In an XAS experiment, monochromatic X-rays are used to excite an electron from a core orbital into unoccupied [conduction] states, and the need for a bright and tuneable source has led to the use of synchrotron radiation for these experiments.[87, 88] The excitation energy is scanned through an energy range that is characteristic for a particular transition—called an absorption edge by virtue of its appearance—and a response that is proportional to the absorption coefficient is measured. There are several ways to detect this response, though the most common detection techniques are transmission, fluorescence yield (FLY), and total electron yield (TEY).[88, 89] **Figure 1.6** shows a typical experiment with three observables detected by the previously-mentioned techniques in their respective order: transmitted photons (I), emitted photons (I_f), and emitted electrons (e^-). In a transmission experiment, the intensity of the X-ray beam (which is proportional to the number of photons) is measured before and after the sample. The change in the intensity of the beam is related to the absorption coefficient, μ, via a modified Beer-Lambert law, shown in eq. (1.8), where I_0 and I are the intensities of the incident and transmitted beams, respectively, and t is the sample thickness. The intensity of the X-ray beam can be measured with an ionization chamber, a gas-filled compartment with an electric field applied across two parallel plates.[87, 90] When X-rays pass through the chamber, some interact with the gas to generate ions and electrons. These charges are collected at the plates to generate a current that is proportional to the amount of amount of incident X-ray photons.[87] If ionization chambers are placed before and after the sample, I and I_0 can be easily measured. The relationship of interest is the change of the absorption coefficient with excitation energy, $\mu(E)$, and rearrangement of eq. (1.8) to isolate μ is shown in eq. (1.9). It is important to note that t is often unknown, but in most experiments the sample thickness does not change between measurements, so determining $\mu t(E)$ provides equivalent results.

$$I = I_0 e^{-\mu t} \quad (1.8)$$

$$\mu = -\frac{1}{t}\ln\left(\frac{I}{I_0}\right) \quad (1.9)$$

Transmission experiments are not always possible, especially at lower excitation energies where photons interact more strongly with matter. The absorption energies of 1st row transition metal $L_{2,3}$-edges (2p orbitals) are in this low-energy regime—the soft X-ray region—so the absorption coefficient must be probed by other means.[88, 89, 91] When a core electron is promoted into conduction states during the experiment, the decay of the excited state is often accompanied by emission of photons *(i.e.*, fluorescence) and electrons (*e.g.*, direct emission of Auger or photoelectrons, or indirect emission of secondary electrons).[57, 88] If the generation of these decay products is directly proportional to the change in the absorption coefficient, they can be detected in an experiment to yield a spectrum that is equivalent to a transmission measurement. This is the case with fluorescence yield (FLY), which detects the photon flux emitted from the sample, and total electron yield (TEY), which monitors a drain current required to replace electrons lost by the sample from emission.[88]

It is important to note that the different phenomena lead to different sampling depths. For instance, a transmission experiment is inherently bulk sensitive, as the entire thickness of the substrate is sampled. Likewise, FLY detects photons emitted by fluorescence, which are sufficiently penetrating to escape from the bulk material. This is not the case for TEY, whose signal is dependent on the number of electrons that escape from the material. As the interaction cross-section with matter is much larger for electrons than photons, electrons rapidly lose energy from scattering and/or absorption, and are thus only able to escape from material if they are generated near the surface.[56, 62-64, 89, 92] As a result, TEY measurements are surface sensitive (with sampling depths generally <10nm), and may not be representative of the bulk material.[57, 88, 93-95]

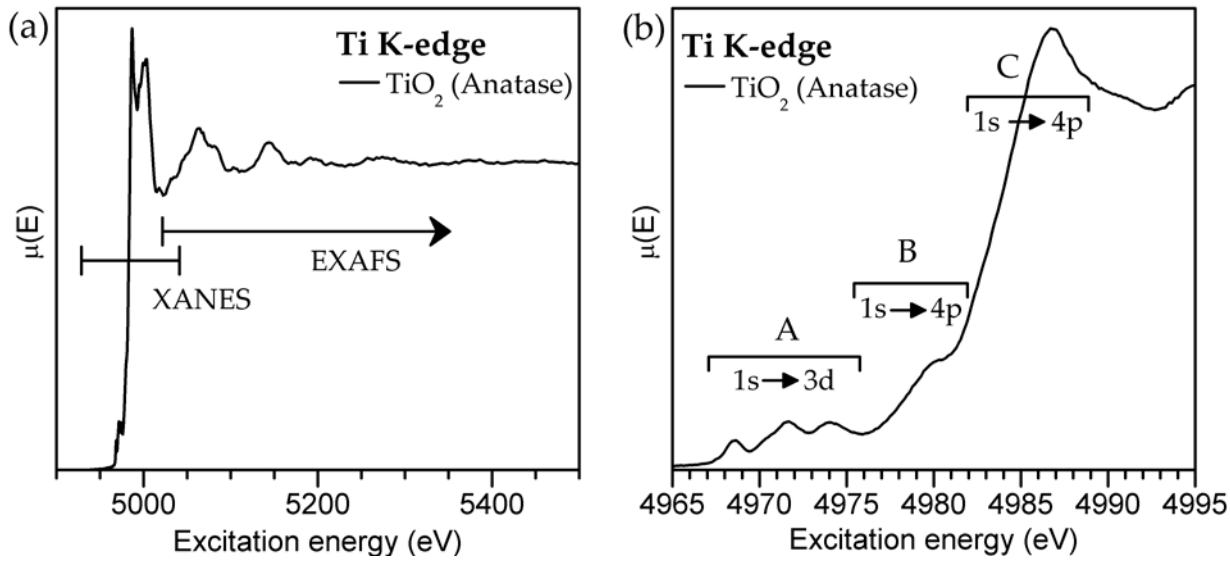

Figure 1.7. (a) A representative transition metal K-edge XAS spectrum, showing the XANES and EXAFS regions. (b) A representative XANES spectrum from a transition metal K-edge. The pre-edge intensity (A), main-edge energy (B), and main-edge intensity (C) have been shown to change with the coordination number and oxidation state of the metal centre being examined.

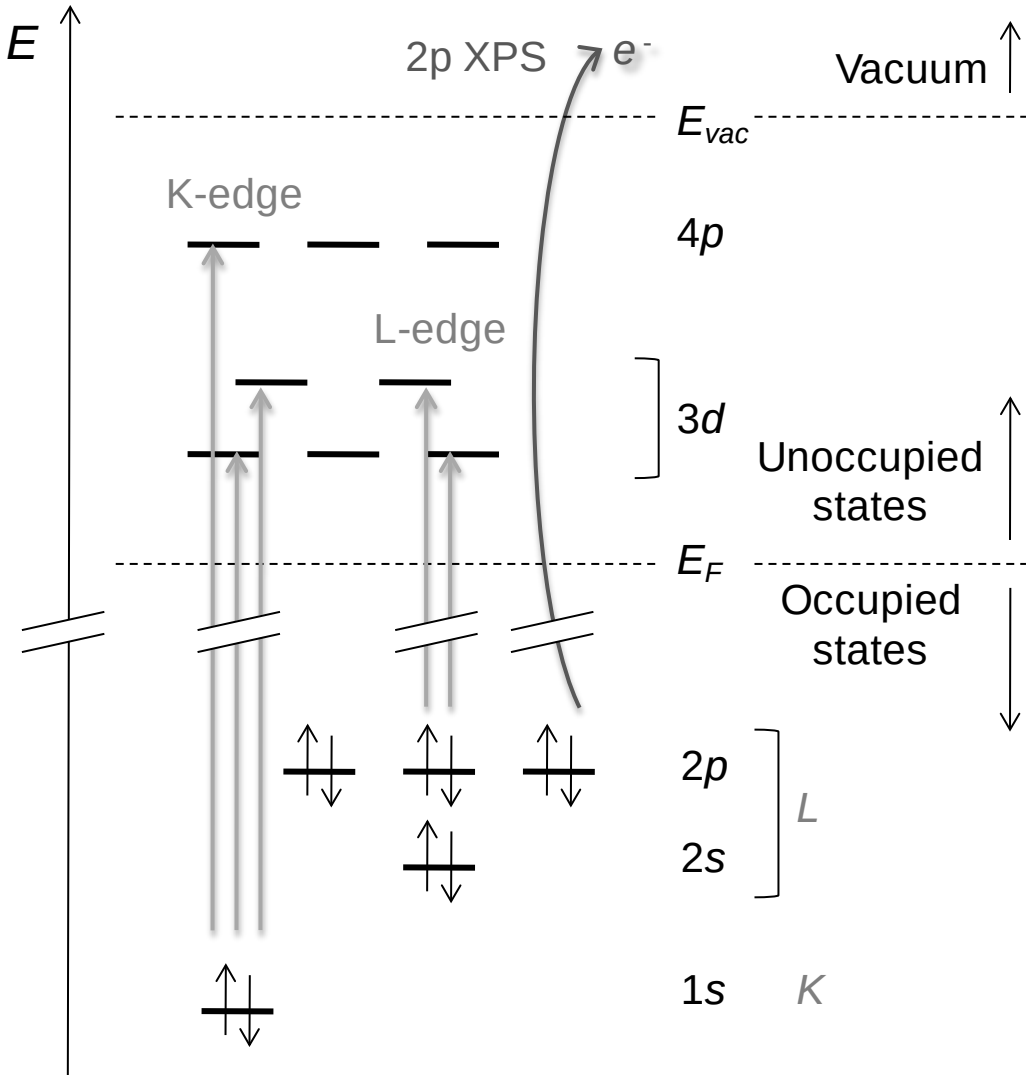

Figure 1.8. An representative energy diagram for representative K- and $L_{2,3}$-edge transitions (from 1s and 2p orbitals, respectively) in XANES. In XANES, the excited electron is still bound to the material in the final state, where it can partially screen the core-hole produced by excitation. The transition for a 2p XPS core-line is shown for comparison, where the excited photoelectron is removed from the material, leading to greater final-state relaxation than in an analogous $L_{2,3}$-edge XANES final state.

Further care must be taken with strongly absorbing or concentrated samples, as the detected signal may not be proportional to the absorption coefficient of the material. In particular, saturation and/or self-absorption effects can deleteriously alter the spectral lineshape by dampening changes in the measured absorption.[89, 94, 96-99] This leads to spectral features with misrepresented intensities, and is most noticeable with strong features, which appear muted. It is well-known that saturation is problematic in fluorescence experiments for samples with a high concentration of absorbing atoms, but it can also be troublesome in soft X-ray TEY measurements when the absorption coefficient increases dramatically at an absorption edge (*e.g.*, first-row transition-metal L_3-edges) and incident photons are less penetrating.[89, 90, 94, 96, 98, 100] (At higher energies, X-rays travel much further through a medium than electrons.) Because several detection methods can be used simultaneously and probe the same property (μ), the spectra can be compared to see whether saturation effects alter the lineshape.

If appropriate sample preparation and detection methods are chosen, the measured absorption spectrum should be a probe of the variation in the absorption coefficient with excitation energy, $\mu(E)$. As the excitation energy is scanned and reaches the threshold required for an allowed electronic transition, μ increases drastically, giving rise to the characteristic absorption "edge" (**Figure 1.7a**).[101] At low energies above the edge (<30 eV), the X-ray absorption near-edge structure (XANES) results primarily from electronic transitions to bound or quasi-bound states localized on the absorbing atom (**Figure 1.8**).[57, 90] At higher energies above the edge (≥30 eV), the electron is promoted to continuum states, where it behaves as a free photoelectron travelling through the material.[57, 90] In this energy-region, the promoted photoelectron has a higher kinetic energy (than in the XANES region), and backscattering of the photoelectron by atoms in the coordination shells surrounding the absorbing atom leads to

interference that creates structured oscillations in the absorption spectrum. These oscillations are known as the extended X-ray absorption fine structure (EXAFS), and are sensitive to the number and identity of scattering atoms.[57, 90] A representative Ti K-edge spectrum is presented in **Figure 1.7a**, where both the XANES and EXAFS regions have been labelled.

The EXAFS region can be modeled to elucidate the local structure of a material; however, there is considerable information that is immediately accessible in XANES. It has been shown that several features in XANES provide important information about the coordination environment and the oxidation state of a given element (**Figure 1.7b**). At lower energy, transition metals with empty d-states have a pre-edge region that is due to 1s → (*n*–1)d [quadrupolar] transitions.[57, 102-106] Formally, these transitions are forbidden (selection rules state that $\Delta l = \pm 1$ due to the conservation of angular momentum), though there remains a low probability of observing them. The probability of these transitions can be increased by addition of dipolar character through mixing with orbitals of p-character from coordinating atoms or possibly from the absorbing atom itself.[57] Despite its weak intensity in most cases, the pre-edge region naturally provides a probe of the d-orbitals of a transition metal, so it provides important chemical knowledge.[57, 104, 105, 107-110] The absorption energy of the pre-edge is sensitive to the oxidation state and coordination number of the metal, and the intensity (A) varies with the coordination number.[104, 105, 107-110] At higher energy, the pre-edge is followed by the main edge, a strong feature that results from 1s → *n*p [dipolar] transitions.[57, 102] Like the pre-edge, the absorption energy (B) and the intensity (C) of the main-edge also change with the oxidation state and the coordination number of the absorbing metal atoms.[102, 105, 107, 108, 111, 112] A representative K-edge XANES spectrum of a transition-metal oxide (TiO_2) is shown in **Figure 1.7b**, where the pre-edge intensity (A), main edge energy (B) and main edge intensity (C) have been labelled.

1.5. Synopsis

Like XPS, shifts in the XANES absorption energies can be explained using the modified charge potential model. However, as electrons in the final state of the XANES absorption process remain associated with the material in conduction states (**Figure 1.8**), relaxation effects (final-state effects) in XANES are generally muted compared to XPS for an analogous transition.[54, 78, 79] This difference is exploited throughout this body of work to determine whether ground-state or final-state effects are the primary cause of XPS binding energy (BE) shifts within two series of materials. Many competing effects influence spectral energies, and the ability to separate these effects is difficult.

Through the deliberate and careful choice of systems to isolate factors influencing XPS BEs, the combination of XPS and XANES is used to examine and resolve some of the competing effects that cause BEs to shift with changes in the first and second coordination shells. Chapter 2 describes the study of $SrFe_{1-x}Zn_xO_{3-\delta}$, an oxygen-deficient perovskite-type isostructural series from $x = 0 \rightarrow 0.3$. In the structure of the end-member of the series ($SrFeO_{2.75}$, *Cmmm* space group), Fe exists as a 50/50 mixture of Fe^{3+} and Fe^{4+}, as expected by simple electron counting rules.[32, 113] Substitution of Zn^{2+} into the system forces a loss of oxygen to balance the charge, and the subsequent decrease in the transition metal coordination number (CN) has been found to cause substantial shifts in BE.

In the $SrFe_{1-x}Zn_xO_{3-\delta}$ system, the *next*-nearest neighbour (NNN) atoms have similar electronegativities ($\chi_{Zn} = 1.66$, $\chi_{Fe} = 1.64$), preventing any effect from changes in the average electronegativity of the NNN site. Chapter 3 and 4 continue by specifically looking at these NNN effects. Toward this end, electronegative Si atoms were gradually substituted by electropositive group IV transition metal ions ($\chi_{Si} = 1.74$, $\chi_{Ti} = 1.32$, $\chi_{Zr} = 1.22$) in a set of isostructural silicates:

$(TiO_2)_x(SiO_2)_{1-x}$ $(0 \leq x \leq 0.33)$, $(ZrO_2)_x(SiO_2)_{1-x}$ $(0 \leq x \leq 0.50)$, and $(ZrO_2)_x(TiO_2)_y(SiO_2)_{1-x-y}$ $(x + y = 0.2, 0.3)$.[114] In these systems, the CN of all atoms remains roughly constant, though large shifts in BE are observed due to differences in the electronegativity of the NNN site.

Chapter 2

2. Coordination-induced shifts of absorption and binding energies in the $SrFe_{1-x}Zn_xO_{3-\delta}$ system*

2.1. Introduction

The perovskite structure is incredibly versatile, and the properties of perovskite-type materials can be changed by altering the composition.[15, 18] Non-stoichiometric, oxygen-deficient perovskite oxides of the formula $ABO_{3-\delta}$ (A = alkali; B = transition metal) have received considerable attention due to their mixed ionic-electronic conduction (MIEC), having oxygen fluxes up to two orders of magnitude greater than conventional materials.[9, 28] This makes the materials potentially useful for, among other things, solid oxide fuel cells, catalysts, and oxygen-permeable membranes. Owing to their lack of chemical durability, alternatives to Co-based MIEC materials are being investigated, with systems similar to $SrFe_{1-x}Zn_xO_{3-\delta}$ having been proposed as new high oxygen-flux ceramics.[115]

The previously-mentioned applications have led to many studies on the physical and electronic properties of the $ABO_{3-\delta}$ system, with focus on industrial applications as a ceramic membrane. To better understand these materials, and how they are affected by substitution, spectroscopic studies using X-ray absorption near-edge spectroscopy (XANES) and X-ray photoelectron spectroscopy (XPS) can be employed. Both XANES absorption energies and XPS binding energies (BEs) are sensitive to the chemical environment because they are related to the

* A version of this chapter has been published. Reprinted with permission from M. W. Gaultois and A. P. Grosvenor, *Journal of Physical Chemistry C*, 2010, **114**, 19822-19829. Copyright 2010 American Chemical Society.

interactions between the atom of interest and its first coordination shell, that is, its nearest neighbour atoms. Longer-range interactions with more distant atoms can also influence these energies, though these effects are often much less pronounced.[56, 73] The observed binding energy (BE) of a photoelectron from atom *i*, E_i, which results from both ground- and final-state energies, can be described by the modified charge potential model.[56, 75] Relative to the binding energy of a reference compound, E_i^0, a shift in BE of atom *i*, ΔE_i, is described by eq. (2.1).[56, 75]

$$\Delta E_i = E_i - E_i^0 = (k\Delta q_i + \Delta \sum_{i \neq j} \frac{q_j}{r_{ij}}) - (\Delta E_i^{\mathrm{IA}} + \Delta E_i^{\mathrm{EA}}) \qquad (2.1)$$

A shift in binding energy results from both ground- and final-state effects, separated in eq. (2.1) by parentheses. Shifts in the ground-state energies are caused by changes in the charge of the atom being excited (q_i in $k\Delta q_i$, where *k* is a parameter due to interactions between core and valence electrons) and the chemical environment ($\Delta \sum_{i \neq j} \frac{q_j}{r_{ij}}$, where r_{ij} is the distance to atom *j*, which has a charge of q_j), which are intra- and extra-atomic effects, respectively.[56, 75] In the final state, after a photoelectron has been ejected from atom *i* and an unscreened core-hole has been produced, the system will rearrange its remaining electrons to minimize its energy. Extra-atomic relaxation of electrons from surrounding atoms, represented by ΔE_i^{EA}, are sensitive to changes in the chemical environment, whereas intra-atomic relaxation of electrons localized on the atom of interest are not, and ΔE_i^{IA} is often negligible.[56] XANES absorption energies shift in a similar fashion to XPS BEs, though, as the excited electron is not removed completely from the system, final-state effects tend to be less significant.[54, 78, 79, 116] As explained above, many factors influence binding and absorption energies, and isolating the main contributors can be difficult.

In this chapter, it is shown that as x increases in the $SrFe_{1-x}Zn_xO_{3-\delta}$ system ($0 \leq x \leq 1$), the oxygen deficiency (δ) increases and the transition-metal (TM) coordination number (CN)

decreases. The changing TM CN induces energy shifts in the TM K-edge XANES spectra and the TM 2p XPS spectra that are not observed in the corresponding TM $L_{2,3}$-edge XANES spectra. Such shifts are a result of final-state effects, whereas only ground-state effects are found to change the O K-edge XANES absorption energies and the O 1s XPS BEs. Here, the factors which influence the absorption and binding energies in $SrFe_{1-x}Zn_xO_{3-\delta}$ are discussed, providing a greater understanding of the effects that can cause these energies to shift.

2.2. Experimental

2.2.1. Synthesis and X-ray diffraction.

The $SrFe_{1-x}Zn_xO_{3-\delta}$ system ($0 \leq x \leq 0.3$) was synthesized by the ceramic method. $SrCO_3$ (Alfa Aesar, 99%), ZnO (Alfa Aesar, 99.9%), and Fe_2O_3 (Alfa Aesar, 99.945%) powders were mixed in stoichiometric amounts and heated in alumina crucibles at 1100°C for >12 h to decompose the carbonate and produce SrO. The resulting product was then ground and pressed into a pellet, and heated at 1200°C over 2–3 days with intermediate grinding and pelleting. All materials were quenched in air except $SrFeO_{2.75}$ ($SrFe_{1-x}Zn_xO_{3-\delta}$, x = 0, space group *Cmmm*), which was cooled to 600°C at 1.25°C/min and annealed at this temperature for >12 h to stabilize the oxygen stoichiometry.[113] At Zn concentrations of $0.3 < x < 1.0$, the materials were multiphase. The materials produced in pure-phase were $SrFe_{1-x}Zn_xO_{3-\delta}$ (x = 0.0, 0.1, 0.2, 0.3), and $SrZnO_2$ ($SrFe_{1-x}Zn_xO_{3-\delta}$, x = 1.0, δ = 1.0, space group *Pnma*), which was synthesized using a temperature of 1100°C. In this system, the range of solid solution was expanded, as only $Ba_{0.5}Sr_{0.5}Fe_{0.8}Zn_{0.2}O_{3-\delta}$ was previously known.[115, 117] Powder X-ray diffraction (XRD) patterns were collected at room temperature using a Rigaku Rotaflex RU-200 rotating anode X-ray diffractometer using Cu Kα radiation. Lattice constants of $SrFe_{1-x}Zn_xO_{3-\delta}$ ($0 \leq x \leq 0.3$) were determined by the program Unit Cell, using an orthorhombic crystal system (*Cmmm*), and were

found to increase with greater Zn content (see **Figure 2.1**).[118] Structural figures (**Figure 2.2**) were generated using VESTA.[119]

2.2.2. Fe and Zn K-edge XANES.

Fe and Zn K-edge XANES spectra were collected at the Canadian Light Source (CLS), using the Hard X-ray Micro-Analysis (HXMA) beamline, 06ID-1, with radiation generated from a 63-pole wiggler insertion device. The flux is ~6 x 10^{11} photons/sec, and the resolution is better than 1 eV at photon energies below 10 keV. For analysis, thin layers of finely ground powder sandwiched between Kapton tape were positioned 45° to the X-ray beam and fluorescence spectra were measured with a Canberra 32-element Ge detector. Spectra were collected from greater than 150 eV below the absorption edge to greater than 500 eV above the absorption edge to ensure proper normalization. Through the absorption edge, the X-ray energy was increased by 0.15 eV per step for Fe and 0.25 eV per step for Zn. A standard thin foil of the elemental metal was positioned behind the sample and analyzed concurrently in transmission mode using N_2-filled ionization chambers, and the absorption edge energy, as determined by the peak maximum of the first derivative, was calibrated to the accepted value of 7112 eV for Fe and 8979 eV for Zn.[87]

2.2.3. Fe L_3-, Zn L_3-, and O K-edge XANES.

Fe L_3- and O K-edge XANES spectra were collected at the CLS using the spherical grating monochromator (SGM) undulator beamline, 11ID-1.[120] The flux is ~10^{11} photons/sec at 1900 eV and increases to ~4 x 10^{12} photons/sec at 250 eV. The resolution is better than 0.3 eV at photon energies below 1500 eV, and the instrumental precision is better than ±0.1 eV. Powdered samples were mounted on carbon tape and measured *in vacuo*. Total electron yield (TEY) and X-ray fluorescence yield (FLY) spectra were collected simultaneously. TEY spectra are presented

for the Fe and Zn L_3-edges, while FLY spectra are presented for the O K-edge, as the TEY is more surface sensitive and influenced by surface adsorbates. Spectra were collected from ~30 eV below the absorption edge to 50–120 eV above the edge to get a suitable background for normalization. All spectra were collected with a 0.1 eV step size through the absorption edge. The spectra were not observed to significantly change even after extended collection times confirming that the surface composition of these materials is relatively stable. The Fe L_3-edge spectra were calibrated against Fe metal powder with the maximum in the first derivative of the L_3-edge set to 706.8 eV.[15] Zn L_3-edge spectra were calibrated to ZnO powder with the maximum in the first derivative of the L_3-edge set to 1026.3 eV.[121] The O K-edge spectra were calibrated to Fe_2O_3 powder with the maximum of the first derivative set to 528.6 eV.[122] All XANES spectra were analyzed using the Athena software program.[123]

2.2.4. Fe 2p, Zn 2p, and O 1s XPS.

XPS measurements were performed using a Kratos AXIS Ultra spectrometer fitted with a monochromatic Al Kα (1486.7 eV) X-ray source. The resolution of this instrument has been determined to be 0.4 eV and the measured binding energies have a precision of better than ±0.1 eV.[124] The area analyzed was ~700 x 400 μm. Finely ground powders were pressed into In foil and mounted on an electrically grounded sample holder. After being loaded into the spectrometer, the samples were cleaned by Ar^+ ion sputtering (4 keV accelerating voltage, 10 mA current) to reduce the concentration of surface contaminants. High-resolution spectra of the Fe 2p, Zn 2p, O 1s, and C 1s core lines were collected with a pass energy of 20 eV, a step size of 0.05 eV, and a sweep time of 180 s. To counter differential charging, the charge neutralizer was used during collection of spectra from $SrZnO_2$. Charge neutralization was not required for examination of the other samples. During data analysis, the samples were calibrated

using the C 1s line arising from adventitious C with a fixed value of 284.8 eV. A Shirley-type function was applied to remove the background arising from energy loss and spectra were fitted using synthetic peaks having a mixed Gaussian (70%) and Lorentzian (30%) line profile.[125]

2.3. Results and discussion

2.3.1. Structure and X-ray diffraction.

Although most studies have refined both Co- and Zn-containing oxygen-deficient perovskites in a cubic space-group, it has been previously argued that the system cannot maintain the cubic symmetry at high oxygen deficiency.[115, 126, 127] Similar complications arose with assignment of the proper space group for $SrFeO_{3-\delta}$.[32] Despite a good fit by a cubic space group, an orthorhombic space group (*Cmmm*) was found to be more appropriate for $SrFeO_{2.75}$ by Rietveld refinement of neutron diffraction data, which is more sensitive than XRD to light elements, such as oxygen.[32]

In the structure of the end-member of the $SrFe_{1-x}Zn_xO_{3-\delta}$ series ($SrFeO_{2.75}$, *Cmmm* space group, **Figure 2.2a**), Fe exists in the centre of corner-sharing FeO_5 square pyramids and FeO_6 octahedra, and Sr^{2+} is in the interstitial sites. By charge balance, Fe exists as a 50/50 mixture of Fe^{3+} and Fe^{4+}.[11,24] As described in Section 2.3.2 (*vide infra*), substitution of Zn^{2+} into the system forces a loss of oxygen to balance the charge, leading to a greater oxygen deficiency (δ) and, therefore, a lowering of the coordination number (CN) of the transition metal (TM). Expansion of the unit cell accompanies the increase in x and δ (see **Figure 2.1**). In this system, the increase in the size of the unit cell is likely a result of size-effects ($r_{Zn2+} = 0.740$ Å > $r_{Fe3+\ (high\text{-}spin)} = 0.645$ Å).[128] In the orthorhombic structure of the other end-member of the series ($SrZnO_2$, *Pnma* space group, **Figure 2.2b**), Zn^{2+} is present in layers of corner-sharing ZnO_4 tetrahedra in zig-zag chains along the b-axis, while Sr^{2+} cations occupy interstitial sites.[129, 130]

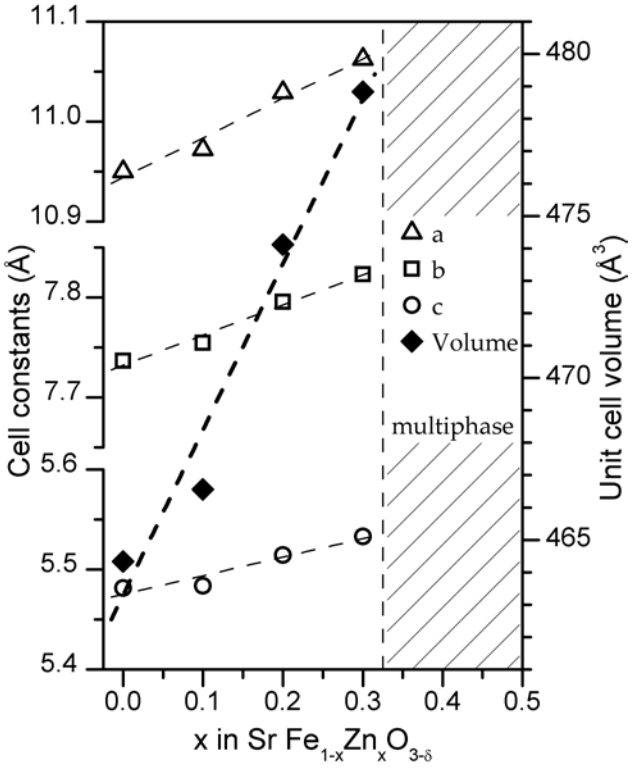

Figure 2.1. An increase in x in the $SrFe_{1-x}Zn_xO_{3-\delta}$ system is accompanied by an increase in oxygen deficiency (δ) and expansion of the unit cell. At a Zn content of x >0.3, there are multiple phases present when examined by powder XRD, and partial melting of these phases occurs at 1200°C. The error in the values is smaller than the size of the symbols.

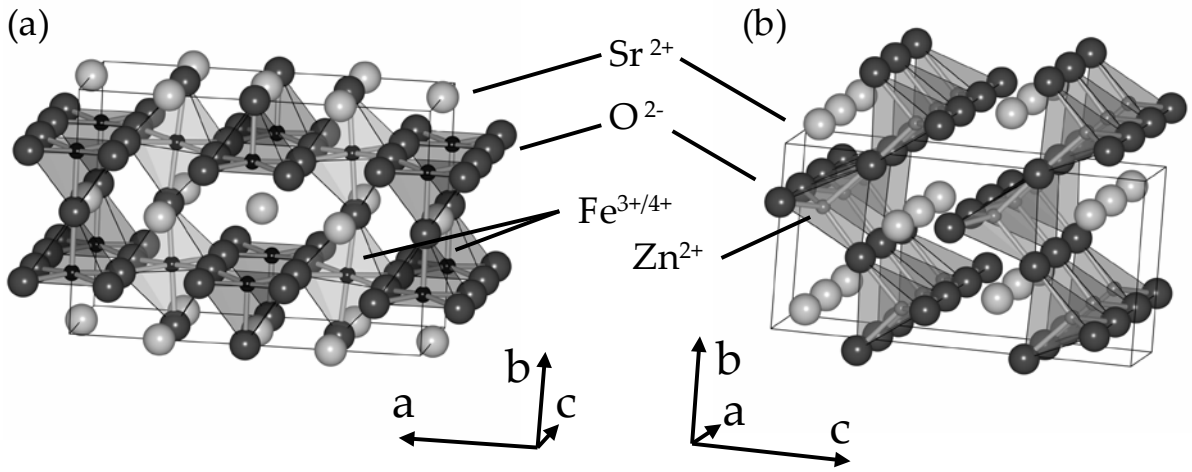

Figure 2.2. (a) In the $SrFe_{1-x}Zn_xO_{3-\delta}$ system, when x = 0 ($SrFeO_{2.75}$, *Cmmm*), TM sites exist in the centre of corner-sharing FeO_5 square pyramids and FeO_6 octahedra. As x increases, Zn^{2+} replaces $Fe^{3+/4+}$, and the oxygen deficiency (δ) increases to balance the charge, causing the average TM CN to decrease. The material exists exclusively in the *Cmmm* structure when $0 \leq x \leq 0.3$. (b) In the $SrZnO_2$ end-member (*Pnma*), corner-sharing ZnO_4 tetrahedra are in layered zig-zag chains.

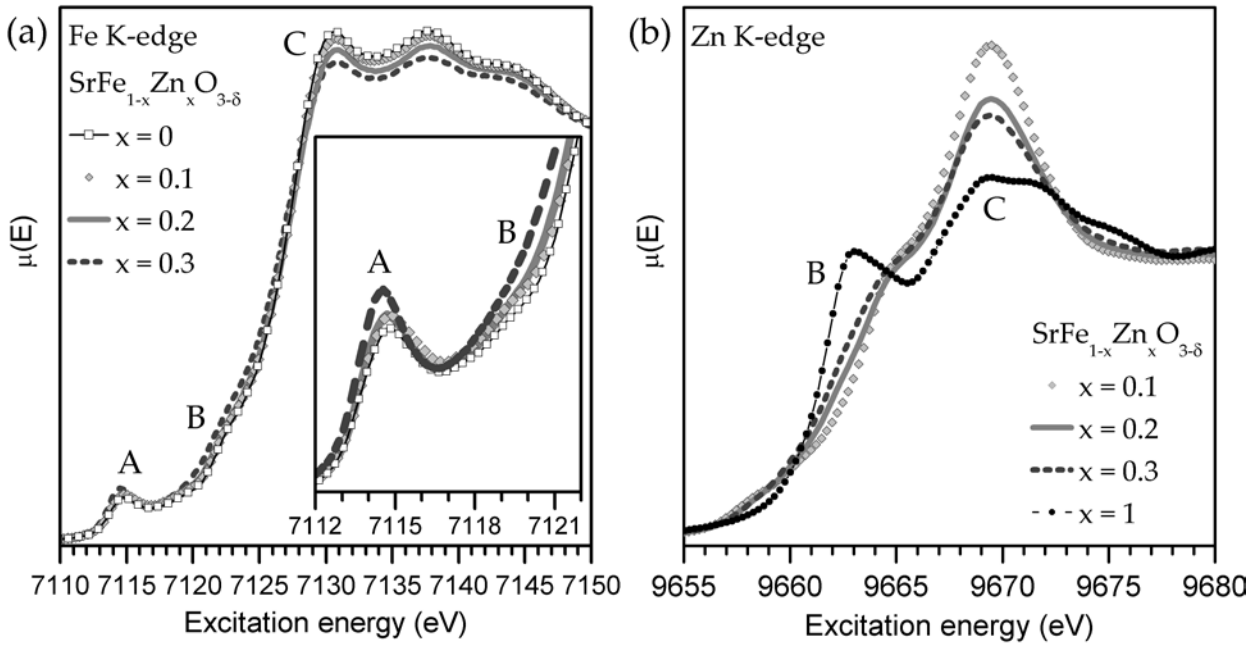

Figure 2.3. (a) Fe and (b) Zn K-edge spectra from $SrFe_{1-x}Zn_xO_{3-\delta}$. The peaks labelled as A, B, and C can be described by the excitations explained in Section 2.3.2. Changes in peak intensity and edge energy are consistent with a decreasing metal CN with increasing Zn content. The inset in (a) shows, more closely, the decrease in the pre-edge (region A) peak intensity and decrease in the absorption energy of region B observed with increasing Zn content.

2.3.2. Fe and Zn K-edge XANES.

Before investigating how the XPS binding energies are affected by substitution, it is important first to understand how the Fe and Zn CNs change with composition. To study changes in CN, Fe and Zn K-edge XANES spectra were collected. These spectra result, primarily, from the dipolar excitation of 1s electrons to *n*p states; however, weaker quadrupolar excitations, 1s → (*n*–1)d, can also occur and are observed at slightly lower energies.[111, 131-134] Multiple investigations have shown that the lineshape and absorption energy of the dipolar and quadrupolar excitations observed in the spectra yield direct information on how the transition-metal CN changes with substitution.[102, 105, 108, 135-137]

2.3.2.1. Fe K-edge XANES.

The Fe K-edge XANES spectra from the $SrFe_{1-x}Zn_xO_{3-\delta}$ series are presented in **Figure 2.3a** and show three main features, labelled as A, B, and C, which all change with CN. The lowest energy feature (A), referred to as the pre-edge peak, is primarily a result of the excitation of 1s electrons to 3d states.[110, 135, 136] Since this is a quadrupolar transition, it is much less intense than the higher energy dipolar excitations (features B and C).[136, 138, 139] As the CN decreases, inversion symmetry is lost and the 3d orbitals are overlapped by 4p states, adding a dipolar contribution to the excitation, which increases the intensity of the pre-edge peak.[136, 138, 140]

The main absorption edge of the spectra (labelled as features B and C in **Figure 2.3a**), located above the pre-edge, results from the excitation of 1s electrons to 4p states, and is significantly more intense than the pre-edge peak.[102, 103, 105, 132, 133] It has been observed that as the CN decreases, an increase in final-state relaxation occurs, resulting from the presence of fewer electrons in the first coordination-shell that are available to screen the core-hole, causing feature B to shift down in energy.[111, 141, 142] Also, the intensity of the main-edge peak (C) has

been observed to decrease as the CN of the metal centre is reduced. This peak results from transitions to empty Fe 4p states that are hybridized with O 2p states.[111, 143] Because the intensity of a transition is proportional to the likelihood of an absorption event and number of empty states that can be populated, a decrease in the number of empty states causes a decrease in peak intensity; similar effects have been observed in other systems.[111, 144, 145] (Note that multiple-scattering resonances (MSR), a special case of the extended X-ray absorption fine-structure (EXAFS), may also contribute to changes in the peak intensity.[106, 141, 146])

In **Figure 2.3a**, it is observed that as the Zn content (x) increases from 0→0.3 in $SrFe_{1-x}Zn_xO_{3-\delta}$, the intensity of the pre-edge (A) increases while the main-edge absorption energy (B) and intensity (C) both decrease. (The absorption energy, B, decreases by 0.3 eV with increasing Zn content.) These observations all indicate that the Fe CN is reduced with increasing Zn^{2+} content (x) and, therefore, greater oxygen deficiency (δ).

2.3.2.2. Zn K-edge XANES.

In contrast to the Fe K-edge, there is no clearly defined pre-edge in the Zn K-edge XANES (**Figure 2.3b**), since the 3d states are filled ($3d^{10}$). However, the dipolar regions of the spectra, labelled identically to those transitions in the Fe K-edge spectra, do change. The edge absorption energy of feature B decreases by >0.6 eV and the intensity of feature C decreases considerably as x increases from 0.1→1 (**Figure 2.3b**). Both observations are consistent with a decrease in Zn CN with increasing x and δ.

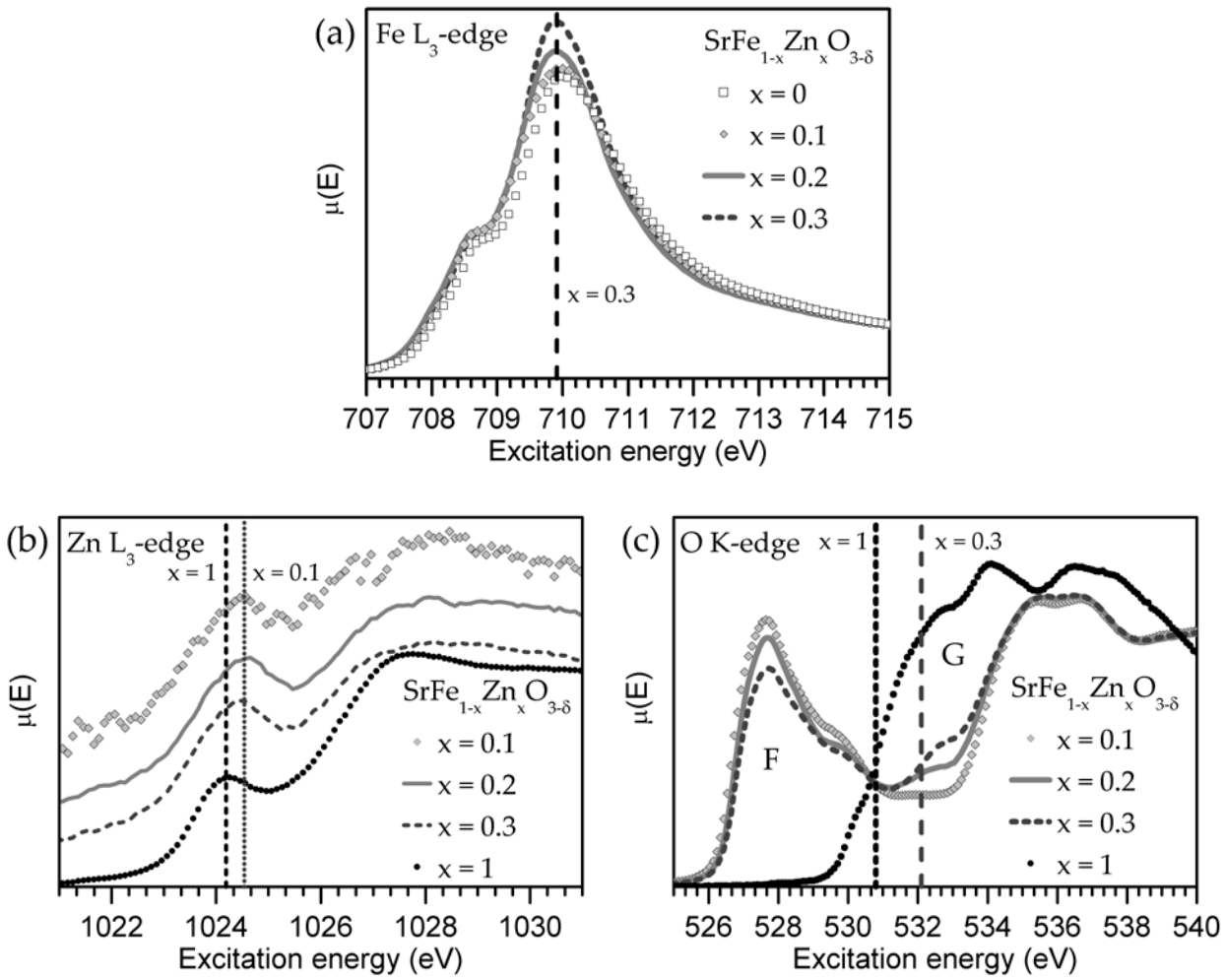

Figure 2.4. (a) Fe L_3-edge spectra of $SrFe_{1-x}Zn_xO_{3-\delta}$ show a negligible change in absorption energy with increasing x, while the increase in intensity suggests an increase in the average charge of Fe. (b) Zn L_3-edge spectra from $SrFe_{1-x}Zn_xO_{3-\delta}$ show a minimal shift in energy, when compared with the large shift in Zn $2p_{3/2}$ BE (Figure 2.5). (c) O K-edge spectra, described in detail in Section 2.3.3. Region F corresponds to transitions from O 1s → 2p states interacting with Fe 3d orbitals, while region G results from O 1s → Fe 4p/4s |Zn 4p/4s| Sr 5s/5p/5d excitations.

2.3.3. Fe L_3-, Zn L_3-edge, and O K-edge XANES.

2.3.3.1. Fe L_3- and Zn L_3-edge XANES.

To further study this system, and to investigate how absorption energies change depending on the orbital excited, the Fe and Zn L_3-edge XANES spectra were collected and are presented in **Figure 2.4**. The transition-metal $L_{2,3}$-edge spectra are dominated by dipole transitions from 2p levels to conduction states (empty (*n*–1)d or *n*s states).[147] When d-states are involved, transitions are influenced by crystal field splitting, providing a useful method to probe coordination.[147] Numerous studies have shown the efficacy of TM $L_{2,3}$-edge XANES for determining oxidation state and site symmetry, as the lineshape and absorption energies are sensitive to charge and coordination.[122, 148-151] Although shifts in energy are useful to track changes in oxidation state, previous studies have shown that the Fe^{3+} and Fe^{4+} energies are very similar (within 0.1 eV).[117] In the $SrFe_{1-x}Zn_xO_{3-\delta}$ system, the Fe L_3-edge (**Figure 2.4a**) absorption energy of the peak maximum decreases by 0.1 eV as x increases from 0→0.3, which is similar to the precision of the experiment (±0.1 eV). The broadness of the spectral peaks is a result of the presence of Fe in multiple coordination environments, which may contribute to the slight shift in absorption energy owing to variations in the crystal-field splitting. An alternative possibility for this slight shift in energy is discussed below (Section 2.3.4). Although no significant shift in absorption energy was observed, the peak intensity in **Figure 2.4a** increases with greater x. This suggests a larger number of unoccupied 3d conduction states into which 2p electrons can be excited (*i.e.*, the Fe oxidation state increases with x, in agreement with Mössbauer studies of an analogous material, $Ba_{0.5}Sr_{0.5}Fe_{0.8}Zn_{0.2}O_{3-\delta}$). [117] The observation above implies that the degree of O deficiency (δ) with increasing x is not as large as might be expected.

Whereas the Fe $L_{2,3}$-edge spectra are dominated by the excitation of Fe 2p states to partially unoccupied Fe 3d states interacting with O 2p states, the Zn 3d-states are filled ($3d^{10}$). Consequently, Zn $L_{2,3}$-edge spectra (**Figure 2.4b**) primarily involve the promotion of electrons from Zn 2p orbitals to empty conduction states involving interacting Zn 4s and O 2p states as well as continuum states. As x increases from 0.1→1.0, the energy of the peak maximum decreases by 0.3 eV, a much smaller decrease than was observed in the Zn K-edge spectra (>0.6 eV, **Figure 2.4a**). (A possible reason for this shift is presented in Section 2.3.4.)

2.3.3.2. O K-edge XANES.

To investigate further how the $SrFe_{1-x}Zn_xO_{3-\delta}$ system is influenced by metal-site substitution, O K-edge spectra were collected and are presented in **Figure 2.4c**. The O K-edge is particularly rich in detail, as O interacts with every atom in the $SrFe_{1-x}Zn_xO_{3-\delta}$ structure. Assignment of the many transitions is outside the scope of this work, though changes in peak intensities with composition, examination of constituent binary oxides, and previous studies on TM oxides make general classification possible.[122, 152, 153] The O K-edge spectra (**Figure 2.4c**) have been divided into regions F and G, corresponding to transitions to O 2p states interacting with empty Fe, Zn, and Sr states.

As the Zn content (x) increases, the O K-edge absorption peak in region F, corresponding to transitions from O 1s to 2p states interacting with Fe 3d orbitals (O 1s → O 2p – Fe 3d), decreases in intensity. The decrease in the intensity of region F is accompanied by an increase in intensity of the lowest energy side of region G, which is a result of Zn 4p/4s-O 2p states (this region also contains transitions to O 2p states interacting with Fe 4p/4s and Sr 4d/5s/5p states).[122, 153, 154] The absorption energy of region F, determined by the peak maximum, does not change as x increases from 0→0.3, a result of the fact that the Fe 3d orbitals are hard screeners, which

are relatively insensitive to changes in screening when compared to the soft-screening, higher-energy, Fe 4p and 4s orbitals involved in region G.[105, 140, 155] This is consistent with the lack of shift observed in the Fe K pre-edge peak energy (**Figure 2.3a**), which also involves Fe 3d states.

Although no shift in the energy of region F was observed, the absorption energy of region G decreases by ~0.9 eV as x increases from 0.1→1.0. Whereas the average TM CN decreases as O is removed from the system, examination of the crystal structures of $SrFe_{1-x}Zn_xO_{3-\delta}$ and $SrZnO_2$ (**Figure 2.2**) suggests that the O CN does not change with varying x and δ. Therefore, the energy shift is likely a result of the replacement of $Fe^{3+/4+}$ by Zn^{2+} cations in the O first coordination shell. Depending on the model of electronegativity (χ), there is little, if any, difference in electronegativity between Zn and Fe ($\Delta\chi = \chi_{Fe} - \chi_{Zn}$: $\Delta\chi_{(Pauling)} = 0.18$, $\Delta\chi_{(Allred\text{-}Rochow)} = -0.02$, $\Delta\chi_{(Sanderson)} = -0.03$), which implies that a change in O-Fe/Zn bond covalency with x is an unlikely explanation for such a significant shift (~0.9 eV).[114, 156, 157] By applying the charge potential model from eq. (2.1), which can also be used to describe shifts in absorption energy, it is more likely that the replacement of $Fe^{3+/4+}$ by Zn^{2+} in the O first coordination shell leads to greater screening of the O nuclear charge (*i.e.*, Zn^{2+} has more valence electrons than $Fe^{3+/4+}$, so $\Delta \sum_{i \neq j} \frac{q_j}{r_{ij}}$ becomes less positive). This change in ground-state screening of O then leads to a lower absorption energy with increasing x.

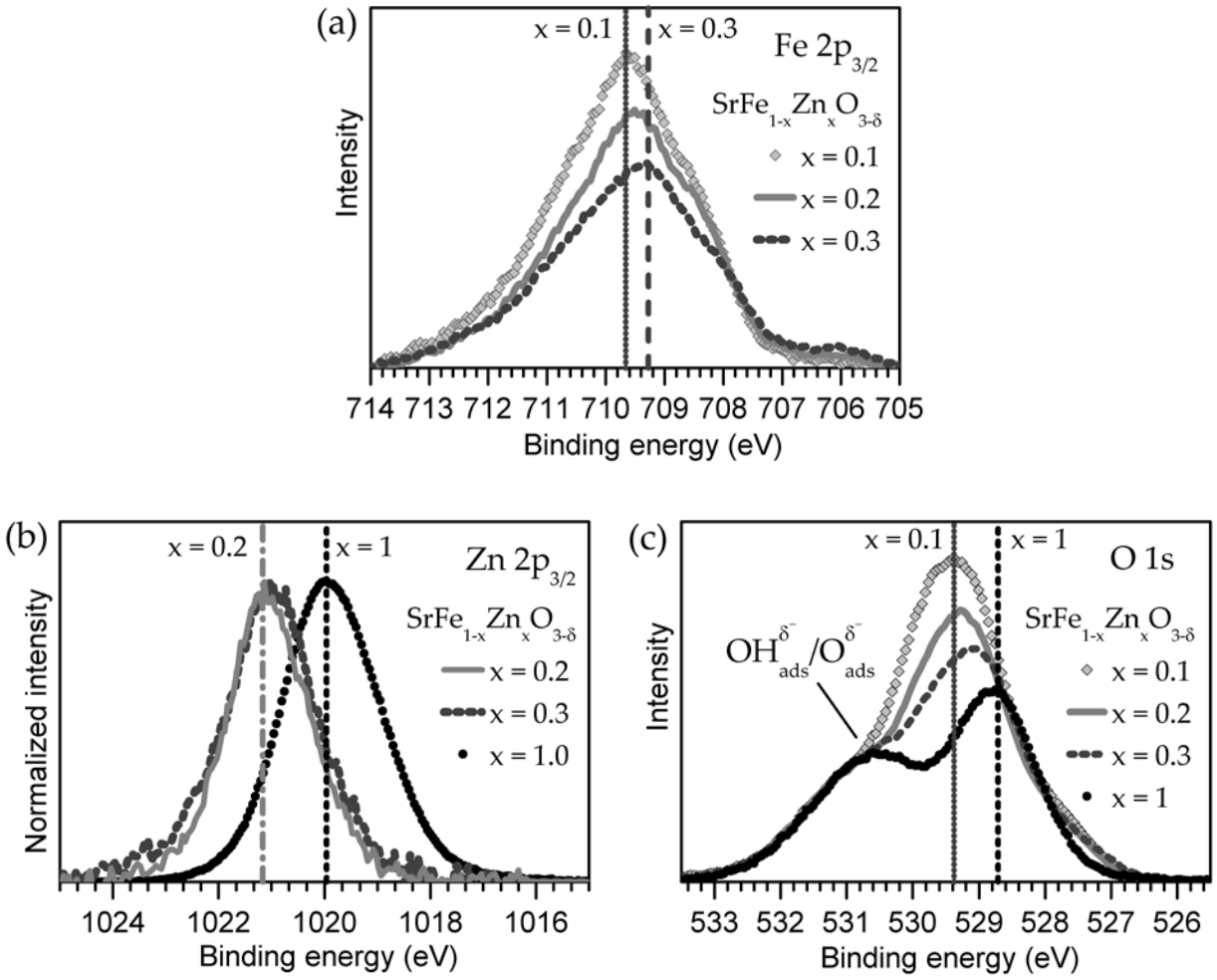

Figure 2.5. High resolution core-line (a) Fe $2p_{3/2}$, (b) Zn $2p_{3/2}$, and (c) O 1s XPS spectra. Fe and Zn BEs decrease with increasing Zn content due to increasing final-state relaxation, while the decrease in O 1s BE is due to ground-state effects. The shifts observed in the Fe and Zn BEs are larger than in the analogous L_3-edge XANES, presented in Figure 2.4. Owing to the large change in intensity observed across the series, normalized Zn $2p_{3/2}$ spectra are presented here.

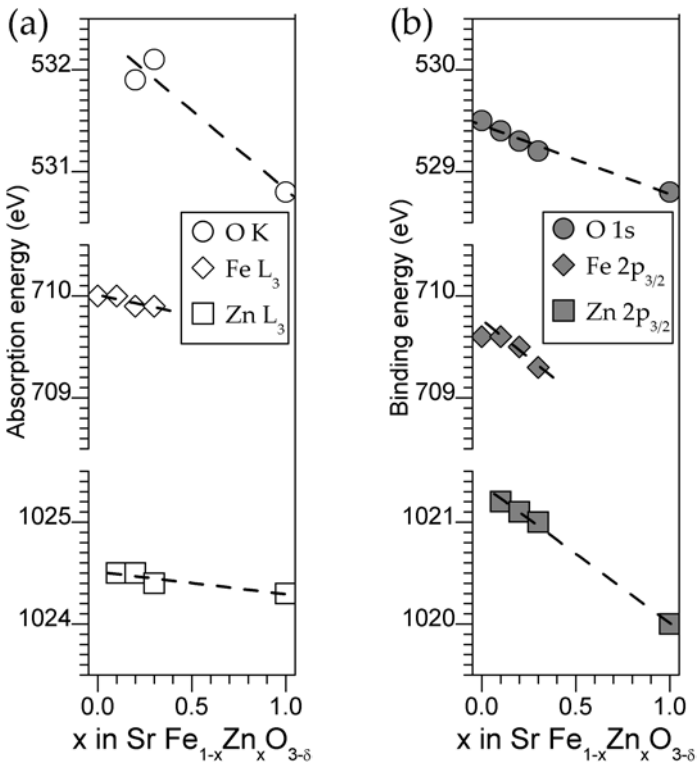

Figure 2.6. Shifts in (a) the XANES absorption energies and (b) XPS BEs with increasing Zn content (x) in $SrFe_{1-x}Zn_xO_{3-\delta}$. The precision of the measurements (±0.1 eV) is equal to the size of the symbols. The O K-edge absorption energy of x = 0.1 phase is not included in (a) because the transition was too weak.

2.3.4. Fe 2p, Zn 2p, and O 1s XPS.

As was presented in the introduction, the XPS excitation fully removes a photoelectron from the system, so final-state relaxation induces considerable shifts in the BE. In the XANES excitation for the same orbital, the excited electron is promoted to unoccupied conduction states and provides some screening of the core-hole, so absorption energy shifts caused by final-state relaxation effects are not as significant. Comparing XPS binding energies to XANES absorption energies allows for a determination of the influence of final-state effects on shifts in BE.

Studying the Fe 2p XPS spectra first (**Figure 2.5a**), as x increases from 0→0.3, the Fe $2p_{3/2}$ BE decreases by 0.3 eV, a more significant shift than was observed in the corresponding Fe L_3-edge absorption energy (**Figure 2.4a**). (A comparison of the shifts in BE and absorption energy is presented in **Figure 2.6**). The Zn 2p XPS spectra are presented in **Figure 2.5b**, and behave in a similar fashion. As x increases from 0.1→1, the Zn $2p_{3/2}$ BE decreases by 1.2 eV (**Figure 2.5b**), yet the Zn L_3-edge absorption energy (**Figure 2.4b**) only decreased by 0.3 eV (see **Figure 2.6**). The magnitude of the BE and absorption energy shifts observed for Zn are much larger than for Fe because of the greater range of x.

The large shifts observed in the Fe $2p_{3/2}$ and Zn $2p_{3/2}$ XPS BEs compared to the much smaller shifts in the corresponding L_3-edge absorption energies implies that the XPS BE shifts result primarily from final-state effects. As mentioned in the introduction, ΔE_i^{EA}, the change in extra-atomic relaxation described in the modified charge potential model, is sensitive to changes in the chemical environment. As x increases in $SrFe_{1-x}Zn_xO_{3-\delta}$, the TM CN decreases and fewer electron-rich O^{2-} anions surround the TM centres, producing a more poorly-screened core-hole. Further, O is electronegative compared to others atoms in the structure (χ_{Zn} = 1.66, χ_{Fe} = 1.64, χ_{Sr} = 0.99, χ_O = 3.50), and its tendency to tightly bind electrons hinders the relaxation of

electrons in the material around a core-hole on a TM centre.[114] Consequently, as x increases (and the CN decreases), the electrons in the system relax to a greater extent to better screen the core-hole produced by the removal of a 2p photoelectron. (Shifts in XPS BE with changing CN have been observed before, albeit rarely.[158, 159]) This reasoning is consistent with the absorption energy shifts observed in the TM K-edge spectra, which are also affected by relaxation (see Section 2.3.2 and below).[133, 135] If these changes in energy were a result of ground-state effects, shifts of similar magnitude would be expected to be observed in the Fe L_3-edge and Zn L_3-edge XANES absorption energies. However, the shifts in absorption energy are considerably smaller when compared to the XPS BE shifts (see **Figure 2.6**), and likely result from a change in ground-state screening of the Fe/Zn nuclear charge with increasing concentration of Zn^{2+} cations in the second coordination shell (*i.e.*, $\Delta \sum_{i \neq j} \frac{q_j}{r_{ij}}$ in eq. (2.1) becomes less positive with increasing x). This will necessarily affect the XPS BEs as well, though it is overshadowed by final-state effects, which dominate.

Deciphering the major contributions to shifts in binding and absorption energies is often problematic, but examination of the same energy level (*e.g.*, Fe 2p and Zn 2p) by both XANES, where final-state relaxation effects are expected to be minor, and XPS, where final-state relaxation effects are more significant, provides a powerful way to differentiate between ground- and final-state effects. To better understand why the magnitude of final-state relaxation changes depending on the orbital excited and the spectroscopic technique used, Slater's rules can be applied to study the changes in screening of the nuclear charge which occur during these excitations.[160] Calculating the relative change in the effective nuclear charge, Z_{eff}, before and after promotion of an electron provides a simple way to estimate the screening provided by the electron. For comparison of Fe 2p photoabsorption and photoelectron spectroscopies, application

of Slater's rules yields a Z_{eff} operating on the outermost valence electron of 3.75 for neutral Fe (Fe: $1s^2 2s^2 2p^6 3s^2 3p^6 3d^6 4s^2$), 3.90 for the XANES photoabsorption final state (Fe*: $1s^2 2s^2 2p^5 3s^2 3p^6 3d^7 4s^2$), and 4.75 for the XPS photoemission final state (Fe^+: $1s^2 2s^2 2p^5 3s^2 3p^6 3d^6 4s^2$). The greater Z_{eff} in the photoemission product implies that greater final-state relaxation will occur.

When comparing the Z_{eff} of the ground-state to the final-state of Fe metal produced by excitation of electrons from different orbitals and by different spectroscopic techniques, Z_{eff} changes by 4% in Fe L_3-edge XANES (2p→3d: $1s^2 2s^2 2p^5 3s^2 3p^6 3d^7 4s^2$), 17% in Fe K-edge XANES (1s→4p: $1s^1 2s^2 2p^6 3s^2 3p^6 3d^6 4s^2 4p^1$, Z_{eff} = 4.40), and 27% in Fe 2p XPS. The above discussion provides a qualitative suggestion of the relative magnitude of relaxation expected from each process and validates the conclusion that the Fe and Zn 2p BEs and the Fe and Zn K-edge absorption energies shift because of final-state relaxation.

Lastly, the O 1s XPS spectra are presented in **Figure 2.5c**. The lowest BE peak is ascribed to O from $SrFe_{1-x}Zn_xO_{3-\delta}$ while the higher BE peak may be attributed to adsorbed $OH^{\delta-}$ or $O^{\delta-}$ present on the surface.[161, 162] However, the possibility that this higher BE peak comes from the $SrFe_{1-x}Zn_xO_{3-\delta}$ system itself cannot be discounted. The intensity of the lowest BE peak decreases with increasing Zn content, confirming the greater O deficiency of this material as x increases in the formula. (This is in agreement with analysis of the Fe K- and Zn K-edge XANES spectra (Section 2.3.2) which show a decrease in transition-metal CN with increasing Zn content.) As observed in **Figure 2.5c** and **Figure 2.6a**, the O 1s BE decreases from 529.4 to 528.7 eV as x increases from 0→1, a decrease of 0.7 eV across the series. This is similar in magnitude to the shift in the O K-edge absorption energy (~0.9 eV, see **Figure 2.6b**), implying

that ground-state effects, like those described in Section 2.3.3.2, play a dominant role in this shift.

2.4. Conclusions

The $SrFe_{1-x}Zn_xO_{3-\delta}$ ($0 \leq x \leq 0.3$) system was synthesized by the ceramic method and the range of solid solution was expanded, as only $Ba_{0.5}Sr_{0.5}Fe_{0.8}Zn_{0.2}O_{3-\delta}$ was previously known.[115, 117] Examination of Fe K- and Zn K-edge XANES spectra show that the transition-metal (TM) coordination number (CN) decreases as x increases in the formula, confirming that the material becomes more oxygen deficient. As the number of electron-rich O^{2-} anions surrounding the TM centres decreases, there is less available electron density to screen the core-hole generated by XANES or XPS processes. A decrease in CN results in a more poorly screened core-hole, resulting in greater final-state relaxation. Further, O is electronegative compared to others atoms in the structure (χ_{Zn} = 1.66, χ_{Fe} = 1.64, χ_{Sr} = 0.99, χ_{O} = 3.50), and its tendency to tightly bind electrons restricts the degree to which electrons from the material can relax around a core-hole on a TM centre.[114] When the TM CN is high, O atoms hinder the ability of electrons in the material to relax around a core-hole on a TM atom. As the CN decreases, electrons are able to relax to a greater extent around the core-hole, lowering the final-state energy and the observed BE. Changes in final-state relaxation are more pronounced in XPS than in XANES, where the excited electron in the final-state can still partially screen the core-hole. Direct comparison of shifts in XANES $L_{2,3}$-edge (2p) absorption energies and XPS 2p BEs reveals that the BE shifts are larger, suggesting that final-state effects are primarily responsible for the shift that accompanies a decrease in CN. This is consistent with estimations of screening through application of Slater's rules, which imply minimal influence from final-state effects in Fe and Zn L_3-edge XANES, with stronger influence in the Fe and Zn 2p XPS spectra.[160] Similar final-state

relaxation effects are also responsible for the decrease in absorption energy observed in the Fe and Zn K-edge XANES, a result of the fact that 1s electrons are strongly screening. Unlike the TM spectra, energy shifts in the O K-edge XANES spectra and analogous O 1s XPS spectra were similar in magnitude, as ground-state effects, owing to increased nearest-neighbour screening of the O nuclear charge with greater Zn content, dominate. Many competing effects influence binding and absorption energies, and the ability to separate these effects is rare. In this study, the influence of coordination number on XPS and XANES spectral energies has been discussed in detail, leading to a better understanding of the different effects which can cause these energies to change.

Chapter 3

3. XANES and XPS investigations of $(TiO_2)_x(SiO_2)_{1-x}$: the contribution of final-state relaxation to shifts in absorption and binding energies*

3.1. Introduction

Amorphous transition-metal silicates (*e.g.*, $(MO_2)_x(SiO_2)_{1-x}$; *M* = Ti, Zr, Hf) are an important class of materials having many interesting properties and applications. All of these compounds exhibit low thermal expansion, are chemically durable, and have a tuneable refractive index, which makes them appropriate for use as anti-reflective films and optical filters.[47, 51, 163-168] The Ti-containing materials have also been examined as catalysts and as catalytic supports, while the Zr- and Hf- containing members have been extensively studied for their possible applications in the electronics industry.[54, 169-177] In particular, $(HfO_2)_x(SiO_2)_{1-x}$ has been proposed as a high-*k* dielectric replacement for SiO_2 to act as a gate dielectric.[40, 44, 54, 176, 177]

These materials can be produced through thin film deposition of the transition-metal or transition-metal oxide on a Si/SiO_2 substrate with the silicate being formed at the interface through annealing or, in powdered form, using sol-gel methods.[44, 47, 54, 163, 168, 178-183] Owing to the lack of long range-order, techniques such as X-ray diffraction yield little information. Because of this, to understand these materials, the use of advanced spectroscopic techniques such as nuclear magnetic resonance spectroscopy, X-ray absorption near-edge spectroscopy (XANES), extended

* A version of this chapter has been published. Reprinted with permission from M. W. Gaultois and A. P. Grosvenor, *Journal of Materials Chemistry*, 2011, **21**, 1829-1836. Copyright 2011 The Royal Society of Chemistry.

X-ray absorption fine-structure (EXAFS), and X-ray photoelectron spectroscopy (XPS) has been necessary. [47, 54, 163, 168, 172-175, 181, 183-191]

Previous spectroscopic investigations (XANES and EXAFS) of the amorphous silicate powders produced by a sol-gel method have shown that the coordination number (CN) of the metal changes with variation in composition.[47, 168, 181, 184, 186, 192] (The Si CN (4) is assumed to be constant.[183]) Sample preparation has been found to greatly affect the metal CN in these materials, as annealing removes organic residues from precursor materials that can coordinate to the metal atoms.[47, 163, 168, 184, 185, 187] Knowing how the metal CN changes with substitution allows for a better understanding of how the properties of these materials can be adjusted through changes in composition. To study thin-films of these amorphous silicates, XPS has been most often used, as the binding energies (BEs) have been found to change considerably with composition.[54, 172, 173, 178-180] Although these materials have a variety of interesting properties and applications that require substantial examination, they are also excellent candidate materials to investigate how variations of the transition-metal CN and degree of ionic bonding influences XANES absorption energies and XPS binding energies. (Si is more electronegative than Ti, Zr, and Hf.[114])

In this chapter, the spectroscopic investigation of sol-gel-produced amorphous Ti silicates, $(TiO_2)_x(SiO_2)_{1-x}$, is reported. By examination of Ti K- and L_3-edge XANES spectra, the variation in Ti CN depending on composition, heat treatment, and if Ti is located within the bulk of the material or at the surface has been investigated. Shifts in XPS BEs have also been studied, and when compared to the corresponding shifts in XANES absorption energies, were confirmed to result from final-state effects. This study, for the first time, provides an understanding of how metal coordination numbers change depending on if the transition-metal is located within the

bulk or surface and also provides important details on how and why the spectral energies shift with composition.

Through substitutional studies of $Sr(Fe_{1-x}Zn_x)O_{3-\delta}$, an oxygen-deficient perovskite-type structure, Chapter 2 showed the effect that changes in CN have on BE shifts. Owing to the similar electronegativities (χ) of Fe and Zn (χ_{Fe} = 1.64, χ_{Zn} = 1.66), XANES absorption and XPS binding energies were unlikely to be affected by a change in the average electronegativity of the next-nearest neighbour (NNN) site.[114] As the NNN effects in solids are poorly understood, it was advantageous to isolate this effect. To maximize the effect for the purpose of studying and understanding the influence of the NNN on XPS BEs, the current chapter continues by looking at $(TiO_2)_x(SiO_2)_{1-x}$, where the difference in the electronegativities of substituted atoms is large (χ_{Si} = 1.74, χ_{Ti} = 1.32).[114]

3.2. Experimental

3.2.1. Synthesis of $(TiO_2)_x(SiO_2)_{1-x}$

The amorphous titanium silicates ($(TiO_2)_x(SiO_2)_{1-x}$; $0 \leq x \leq 0.33$) were synthesized using a sol-gel method.[47, 180] (At high values of x, the material is inhomogeneous.[47, 168, 181]) The less reactive Si-alkoxide was prehydrolyzed by combining tetraethyl orthosilicate (≥99%, Sigma Aldrich), ethanol (anhydrous), and water in a 1:1:1 molar ratio with catalytic amounts of HCl. After stirring this solution under refluxing conditions at 70°C for 2 hours, the reaction was cooled to room temperature and a stoichiometric amount of titanium (IV) tert-butoxide (99.95%, Strem) was added drop-wise with stirring. All reactions were carried out under a N_2 atmosphere. After increasing the water:alkoxide (Ti and Si alkoxide) molar ratio to 1:1, the mixture was sealed and left to sit for >10 days, after which time the material was exposed to the atmosphere for 7 days. Powders were obtained by grinding the resulting materials, placing them under

vacuum for >24 hours, and finally annealing them in air at 550°C for 12 hours to remove residual organic material. The formation of these materials was confirmed by use of Fourier transform infrared spectroscopy.[47, 168] The lack of long-range order present in these materials, even after annealing at temperatures up to 550°C, was confirmed by powder X-ray diffraction using Cu Kα radiation generated from a Rigaku Rotaflex RU-200 rotating anode X-ray diffractometer.

3.2.2. XANES

3.2.2.1. Ti K-edge

Ti K-edge XANES spectra were collected using the Pacific Northwest Consortium/X-ray Science Division Collaborative Access Team (PNC/XSD-CAT, Sector 20) bending magnet beamline (20BM) located at the Advanced Photon Source (APS), Argonne National Laboratory. A silicon (111) double crystal monochromator was used, providing a photon flux of ~10^{11} photons/second and a resolution of 1.4 eV at 10 keV. Finely ground samples were sandwiched between Kapton tape, and positioned 45^{o} to the X-ray beam. Transmission spectra were measured with N_2-filled ionization chambers and fluorescence spectra were collected using a 13-element Ge detector. The X-ray energy was increased by 0.15 eV per step through the absorption edge. Spectra were calibrated by comparison to the spectrum from Ti metal, collected concurrently in transmission mode, which has a well-known edge energy (4966 eV).[87] The Ti K-edge spectrum from anatase (TiO_2; 99.6%, Alfa Aesar) was also collected to provide a standard for comparison of pre-edge peak intensities and absorption energies. The precision of the measurements is estimated to be ±0.1 eV.

3.2.2.2. Ti $L_{2,3}$- and O K-edge

Ti $L_{2,3}$- and O K-edge XANES spectra from $(TiO_2)_x(SiO_2)_{1-x}$ were collected using the Spherical Grating Monochromator beamline (SGM, 11ID-1) located at the Canadian Light Source (CLS).[120] The flux is ~10^{11} photons/second at 1900 eV and increases to ~4×10^{12} photons/second at 250 eV. The resolution is better than 0.3 eV at photon energies below 1500 eV and the precision of the measured absorption energies is better than ±0.1 eV. Spectra from powders of the material pressed on carbon tape were collected in total-electron (TEY; Ti $L_{2,3}$-edge) and fluorescence (FLY; O K-edge) yield mode. Through the absorption edge, the photon energy was increased by 0.1 eV per step. The Ti $L_{2,3}$- and O K-edge spectra were calibrated by collecting spectra from Ti metal and Cr metal, respectively, which have well known Ti L_3-(453.8 eV) and Cr L_3-edge (574.1 eV) absorption energies.[87]

3.2.2.3. Si $L_{2,3}$-edge

The Si $L_{2,3}$-edge XANES spectra from $(TiO_2)_x(SiO_2)_{1-x}$ were collected using the Variable Line Spacing Plane Grating Monochromator (VLS PGM, 11ID-2) at the CLS. The flux is 2×10^{12} photons/second at 80 eV, the resolution is better than 0.01 eV at 100 eV, and the precision of this beamline is better than ±0.1 eV. The FLY spectra from powdered samples pressed on carbon tape were collected by stepping the excitation energy through the absorption edge at 0.05 eV increments. The spectra were calibrated by comparison to a spectrum from a Si wafer having a Si L_3-edge absorption energy of 99.4 eV.[87] All XANES spectra represent the average of multiple scans of each absorption edge, and were analyzed using the Athena software program.[123]

3.2.3. XPS

XPS spectra were collected using a Kratos AXIS 165 spectrometer and a monochromatic Al Kα (1486.7 eV) X-ray source. The resolution of this instrument has been determined to be 0.4 eV and the precision of the measured binding energies, which are significant to two decimal places, is better than ±0.10 eV.[193] Finely ground powders of $(TiO_2)_x(SiO_2)_{1-x}$, TiO_2 (anatase), and SiO_2 (99.99%, Alfa Aesar) were pressed into In foil and mounted on an electrically grounded sample holder. High-resolution spectra of the Ti 2p, Si 2p, O 1s, and C 1s core lines were collected using a pass energy of 20 eV, a step size of 0.05 eV, and a sweep time of 180 s. To counter surface charging, the charge neutralizer was used during collection of all spectra. (Ar^+ ion etching was not used to clean the samples, as testing found that it resulted in the reduction of some of the Ti atoms located at the surface of these silicates.) All spectra were calibrated using the C 1s line arising from adventitious C with a fixed value of 284.8 eV. A Shirley-type function was applied to remove the background arising from energy loss and spectra were fitted using synthetic peaks having a combined Gaussian (70%) and Lorentzian (30%) line profile.[125] The Si $2p_{3/2}$ BE was found by fitting the Si 2p core-line envelope with two peaks (Si $2p_{3/2}$ and Si $2p_{1/2}$) having a 2:1 peak area ratio ($2p_{3/2}$:$2p_{1/2}$).

3.3. Results and Discussion

3.3.1. Ti K-edge XANES

As $(TiO_2)_x(SiO_2)_{1-x}$ is an amorphous silicate, techniques other than X-ray diffraction are required to study the local structure of these materials. To investigate how the Ti coordination number (CN) changed with annealing and Ti content (x), Ti K-edge XANES spectra were collected. These spectra result, primarily, from the dipolar excitation of Ti 1s electrons to unoccupied Ti 4p states.[102, 138] Lower energy and intensity quadrupolar transitions (1s→3d) are

also observed and are referred to as pre-edge peaks.[102, 138] All of the features in these spectra have been found to change with charge, bonding environment, and CN.[105, 111, 112, 136, 145, 155] The highest energy, most intense, dipolar portion of the spectrum (main-edge) decreases in energy and intensity with lowering CN, a result of poorer screening of the core-hole and reduced number of metal-ligand states (Ti 4p – O 2p in the case of this system) available for 1s electrons to be excited to.[111, 112, 144, 145]

Along with the changes to the main-edge portion of the spectrum described above, the energy and intensity of the Ti K-edge pre-edge peak has been observed to change significantly depending on CN.[106, 110, 194] As the CN decreases from 6, inversion symmetry is lost and the Ti 3d states are overlapped partially by 4p states, lending a dipolar component to the excitation and causing the peak intensity to increase.[136, 138] The decrease in energy of the pre-edge with decreasing CN is likely a result of changes in final-state core-hole screening.[195] Simultaneous examination of the pre-edge peak intensity and energy allows for a detailed analysis of how the Ti CN changes in a system.[106, 110, 194] In the silicates studied here and related materials, Ti has a fixed charge of 4+; all of the changes in the Ti K-edge spectra are ascribed to changes in Ti CN, which depend on composition and annealing temperature.[196]

The Ti K-edge XANES spectra from $(TiO_2)_{0.20}(SiO_2)_{0.80}$ annealed at 550°C, as well as not annealed, are presented in **Figure 3.1a** and are compared to the spectrum from TiO_2 (anatase); the pre-edge and main-edge sections of the spectra are labelled as A and B, respectively. The pre-edge peak (A) is more intense in $(TiO_2)_{0.20}(SiO_2)_{0.80}$ (annealed or otherwise) than in TiO_2, implying that the Ti CN is lower in the silicate than in the oxide. This is confirmed by examination of the main-edge peak (B), as the energy and intensity are lower in the silicate than in the oxide.

After annealing the silicate at 550°C, by examination of the Ti K-edge spectra (**Figure 3.1a**), the average Ti CN was found to be lower than for the sample that was not annealed. The fact that the average metal CN is higher before the silicate material is annealed is well known and has been observed by XANES and EXAFS for a number of different silicate systems.[47, 163, 184, 185, 187] The increase in CN is a result of the metal coordinating with ligands from the precursor materials (hydroxide and alkoxide functional groups), leading to metal centres which have tetrahedral, square pyramidal, and octahedral geometries.[47, 188] Examination of the energy and intensity of the peak maximum in the pre-edge of the unannealed material suggests that the Ti atoms are located in a primarily 5-coordinate environment.[106, 110, 194] The presence of some spectral intensity at slightly higher and lower energies (~4972–4975 and ~4967–4969 eV) in the unannealed sample is similar to that observed for TiO_2, implying that some 6-coordinate Ti is also present. (In the pre-edge peak from TiO_2, three distinct structures (labelled as A_1, A_2 and A_3 in **Figure 3.1a**) are observed because of local, quadrupolar, and non-local, dipolar, excitations.[135])

If 4-coordinate Ti was present in any significant amount in the unannealed sample, a lower energy (<4971 eV), intense pre-edge peak would be observed, owing to the greater overlap of Ti 3d and 4p states. The annealed silicate, on the other hand, has a pre-edge peak located at ~4970 eV which is much more intense than the peak at ~4971 eV observed in the unannealed sample. This implies that a significant amount of 4-coordinate Ti *is* found in the annealed material, corresponding to the loss of hydroxide and/or alkoxide ligands from the starting materials. As the principle pre-edge peak is relatively broad (*i.e.*, it encompasses the main-peak from the unannealed sample; see inset of **Figure 3.1a**), it is likely that some 5-coordinate Ti remains after annealing. Further, some peak intensity is observed in the energy region of ~4972–

4975 eV implying that a minor amount of 6-coordinate Ti is also present. The identification of 5-coordinate Ti in these silicates has been suggested by some in the past and denied by others.[47, 181, 187, 188, 192, 197] The presence of 5-coordinate Ti in the system investigated here is likely a result of the different annealing conditions used (550°C for 12 hours) compared to that used by other research groups.[181, 187, 197, 198] (A low annealing temperature was used in this work to limit the formation of TiO_2-clusters, as the primary purpose of this investigation was to study how XANES and XPS spectral energies and lineshapes are affected when Ti is randomly exchanged for Si in the Ti-O-Si bonding environment.)

The consequence of changing the composition on the Ti CN was further studied by Ti K-edge XANES analysis of annealed samples. The spectra are presented in **Figure 3.1b** and, by examination of the decreasing pre-edge peak intensity with x (see inset), it can be clearly observed that the average Ti CN increases with increasing Ti content (x) in the $(TiO_2)_x(SiO_2)_{1-x}$ system. Note that the major decrease in intensity is found in the region where signals from 4- and 5-coordinate Ti would be expected (~4968–4972 eV) whereas the intensity of the region resulting from the presence of some 6-coordinate Ti (>4971 eV) increases slightly. This result is known and implies that at low values of x, Ti is exchanged for Si having a tetrahedral environment.[47, 181, 183] With increasing Ti content, the larger ionic radius ($r_{Ti4+\,(CN\,=\,4)}$ = 0.42 Å, $r_{Si4+\,(CN\,=\,4)}$ = 0.26 Å) opens the structure allowing for more O atoms to interact with the metal centre.[128, 181] The increase of the Ti CN with increasing x has also been ascribed to the formation of TiO_2 clusters within a SiO_2 matrix.[47, 187, 199, 200] The XANES spectra presented here cannot provide evidence of the presence, nor absence, of TiO_2 clusters within these samples. However, as no narrow diffraction peaks were observed in collected powder X-ray diffraction patterns (not shown), it is likely that any ordered TiO_2 domains that may have formed are small.

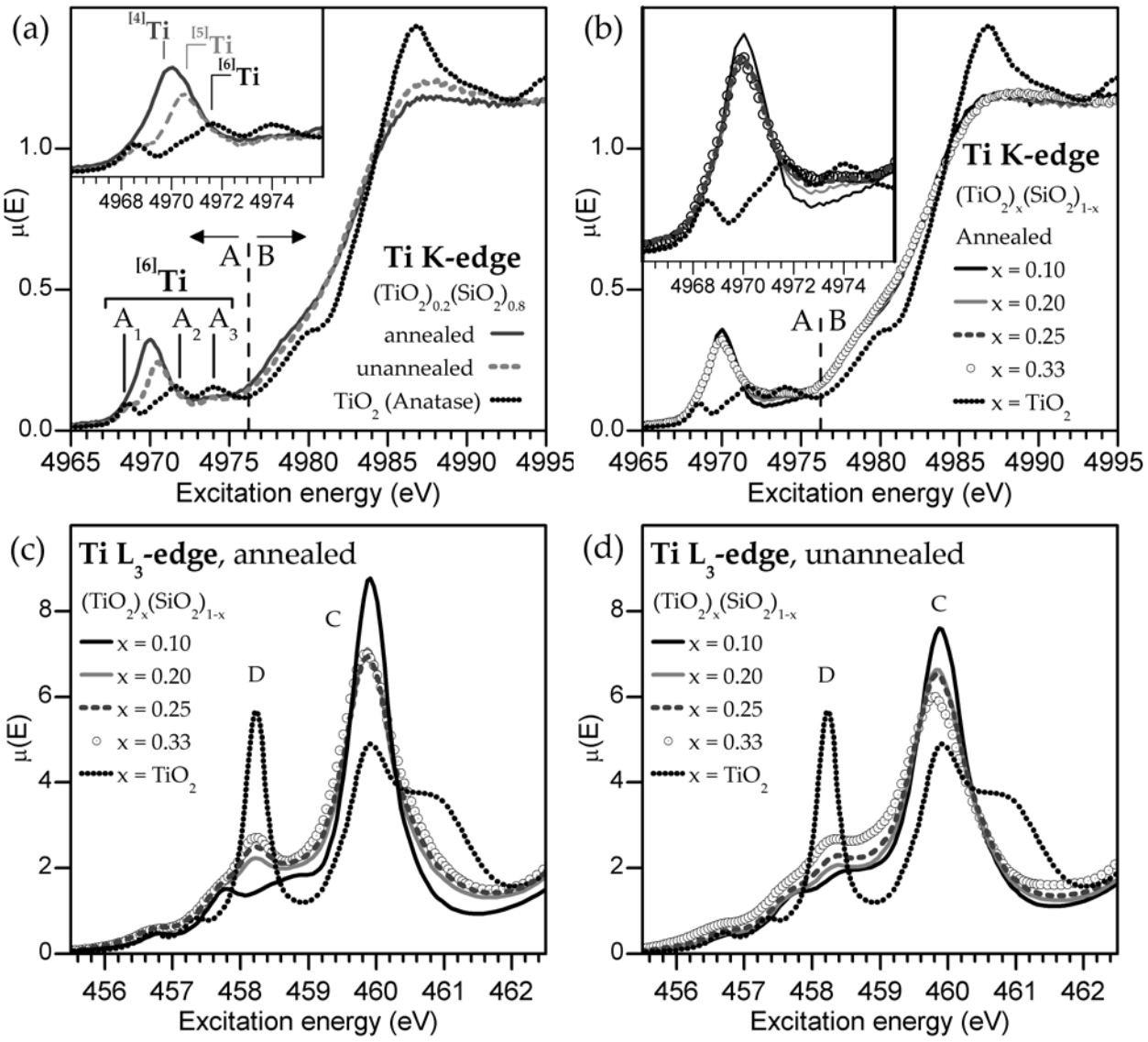

Figure 3.1. Ti K-edge (a,b) and Ti L_3-edge (c,d) XANES spectra of $(TiO_2)_x(SiO_2)_{1-x}$. (a) Ti K-edge absorption spectra showing the changes in lineshape resulting from CN changes observed when comparing annealed and unannealed $(TiO_2)_{0.2}(SiO_2)_{0.8}$ to TiO_2 (anatase). The pre-edge is presented in the inset with typical peak energies for 4-, 5-, and 6-coordinated Ti. The three pre-edge peaks observed in the spectrum from TiO_2 due to both local and non-local transitions are labelled as A_1, A_2, and A_3. (b) Ti K-edge absorption spectra from annealed $(TiO_2)_x(SiO_2)_{1-x}$ silicates showing an increase in the average Ti CN with increasing Ti content (x). (c) Ti L_3-edge absorption spectra of annealed $(TiO_2)_x(SiO_2)_{1-x}$. This surface sensitive analysis shows that the average CN of Ti near the surface increases with x, and is generally higher than that observed for Ti present within the bulk of the material. (d) Ti L_3-edge absorption spectra of unannealed $(TiO_2)_x(SiO_2)_{1-x}$. The average Ti CN increases with increasing x and is always higher than for the unannealed materials having the same Ti concentration.

3.3.2. Ti $L_{2,3}$-edge XANES

Multiple investigations have used Ti K-edge XANES and EXAFS to investigate the change in the Ti CN with composition in the $(TiO_2)_x(SiO_2)_{1-x}$ system.[47, 181, 187, 197] These studies are inherently bulk-sensitive and do not provide any considerable insight to how the CN of Ti atoms located at the surface of the material changes with composition and annealing. One way to study the CN of the Ti atoms located at the surface is to collect Ti $L_{2,3}$-edge XANES spectra in TEY mode. The surface sensitivity of this technique is related to the short inelastic mean free path of electrons as they travel through the material, resulting in depth sensitivities on the nm, rather than μm, scale.[95] This particular spectrum results primarily from the excitation of Ti 2p electrons to unoccupied Ti 3d states.[188] By analysis of various Ti mineral phases and Ti-containing glasses, it has been found that the Ti $L_{2,3}$-edge lineshape changes considerably with CN.[188]

The Ti L_3-edge spectra from $(TiO_2)_x(SiO_2)_{1-x}$ and TiO_2 are presented in **Figure 3.1c**. When x = 0.10, the lineshape is consistent with Ti having a CN of 5, and shows few features resulting from 4- and/or 6-coordinate Ti.[188] With increasing x, the main peak, labelled as C in **Figure 3.1c** (~460.5 eV), decreases in intensity. Concurrently, a new peak located at ~458.4 eV (labelled as D in **Figure 3.1c**) is visible when x >0.10, and increases in intensity with x. By comparison to the spectrum from TiO_2, peak D and C can be attributed to the crystal-field split 3d t_{2g} and e_g* states expected for Ti having a CN of 6.[188] These observations imply that the Ti CN increases from ~5 to between 5 and 6 with greater Ti content. The identification of decreasing Ti CN (from 5 to 4) with greater Ti content, through analysis of Ti $L_{2,3}$-edge XANES spectra, has been suggested in the past, but this interpretation is unlikely considering that Ti prefers to reside in higher-coordinate sites and that a large concentration of species able to

coordinate with Ti atoms are available at the surface.[188] The difference in the average CN depending on if Ti is located in the bulk of the material, as studied by analysis of Ti K-edge spectra, or near the surface of the material, as studied by analysis of Ti $L_{2,3}$-edge spectra, can be related to the availability of surface hydroxide and water groups to bond to the Ti atoms located in the surface region. The Ti L_3-edge XANES spectra from the $(TiO_2)_x(SiO_2)_{1-x}$ samples which were not annealed show a similar trend to that observed for the annealed samples (see **Figure 3.1d**). As peak D is always present in the spectra shown in **Figure 3.1d**, regardless of x, the average Ti CN is always higher in the unannealed samples than in the annealed samples.

3.3.3. XPS

In the previous sections, it was shown that analysis of Ti K- and $L_{2,3}$-edge XANES spectra can be very useful to studying changes in CN with composition. These spectra can also provide information on how the electronic structure is affected by substitution of one element for another; however, such effects can be difficult to study when the CN of the atom of interest is variable. Owing to the considerable differences in electronegativity between Si and Ti, changes in the character of the Ti/Si-O bond are expected with changing composition.[114] To investigate these effects, XPS can be used through examination of shifts in binding energy (BE). The source of BE shifts can be identified using a simple model that describes changes in energy arising from both ground- and final-state effects.[56, 75] This modified version of the charge potential model is defined by eq. (3.1).[56]

$$\Delta E_i = E_i - E_i^0 = (k\Delta q_i + \Delta \sum_{i \neq j} \frac{q_j}{r_{ij}}) - (\Delta E_i^{IA} + \Delta E_i^{EA}).^{64,65} \qquad (3.1)$$

The total binding energy shift, ΔE_i, which is the difference between the measured binding energy of the atom of interest, E_i, and a reference binding energy, E_i^o, consists of a number of

contributions. The $k\Delta q_i$ term describes intra-atomic effects involving the change in charge Δq_i on atom i.[56, 75] (The k term is a constant, and describes the interaction between valence and core electrons.[56, 75]) The $\Delta\sum_{i\neq j}\frac{q_j}{r_{ij}}$ term describes interatomic effects involving changes in the local chemical environment.[56] Both terms introduced above are ground-state effects, describing shifts in BE resulting from changes in the screening of the nuclear charge of the atom being excited, *i*. However, final-state effects, through changes in the magnitude of final-state relaxation, can also influence BEs. These effects are described in eq. (3.1) by the (ΔE_i^{IA} + ΔE_i^{EA}) terms and represent intra-atomic (*IA*) and extra-atomic (*EA*) relaxation, respectively, with ΔE_i^{IA} often being negligible.[56, 75] Shifts owing to final-state relaxation result from changes in the ability of electrons to screen the core-hole produced by removal of a photoelectron. Depending on the system under investigation, BEs can be found to shift because of ground-state or final-state effects, or a combination of both.

3.3.3.1. Ti $2p_{3/2}$, Si 2p, O 1s XPS

To study how the Ti/Si electronegativity affects this system; Ti 2p, Si 2p, and O 1s XPS spectra were collected for the annealed materials and are presented in **Figure 3.2**. The BEs from all three spectra, which are plotted in **Figure 3.3**, were found to decrease with greater Ti concentration. As is described below, this decrease in BE is driven by an increase in final-state relaxation with greater Ti content.

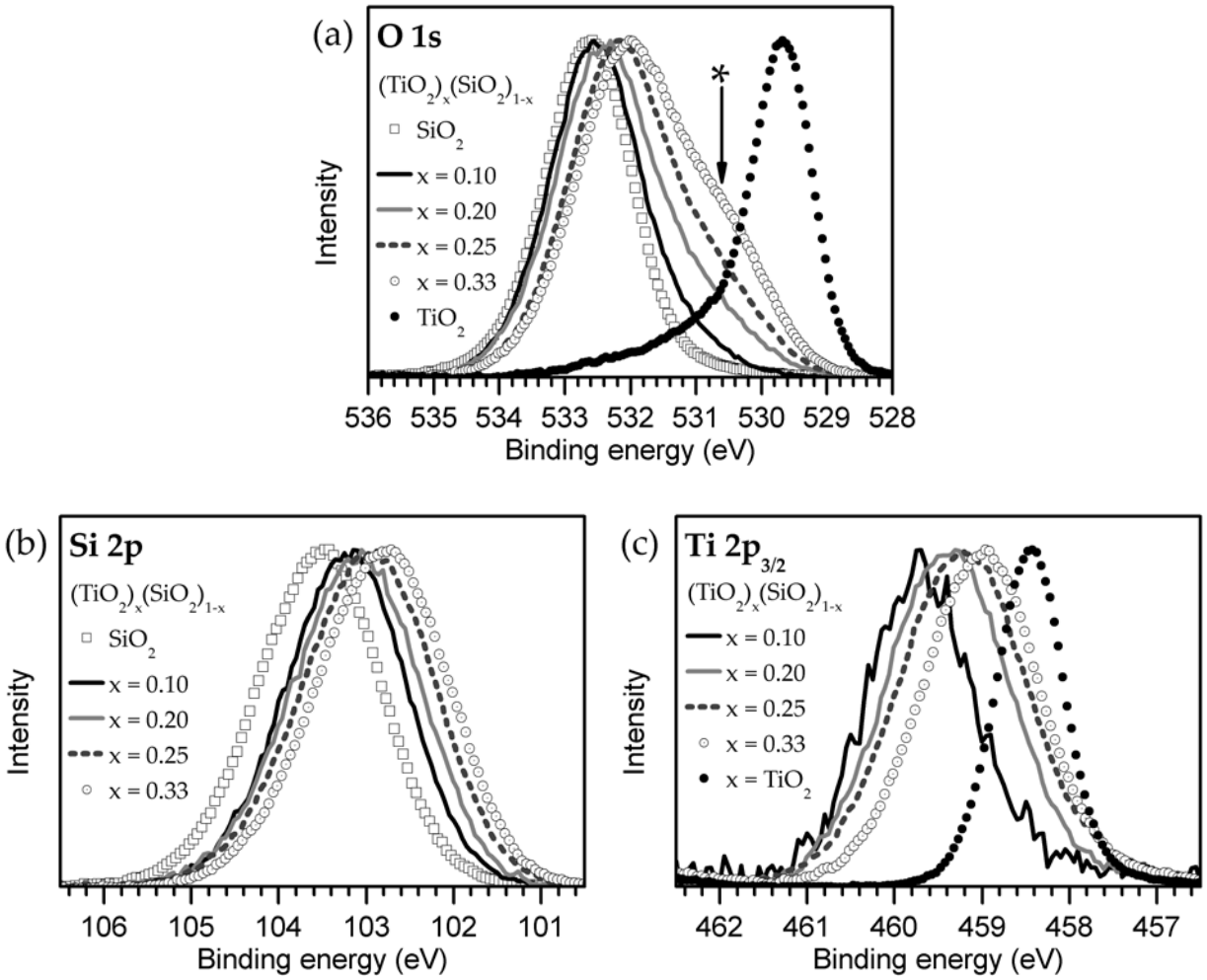

Figure 3.2. High resolution core-line (a) O 1s, (b) Si 2p, and (c) Ti $2p_{3/2}$ XPS spectra of annealed $(TiO_2)_x(SiO_2)_{1-x}$. The asterisk, *, in (a) highlights the low-BE shoulder observed in the O 1s spectra which is caused by Ti-rich domains.

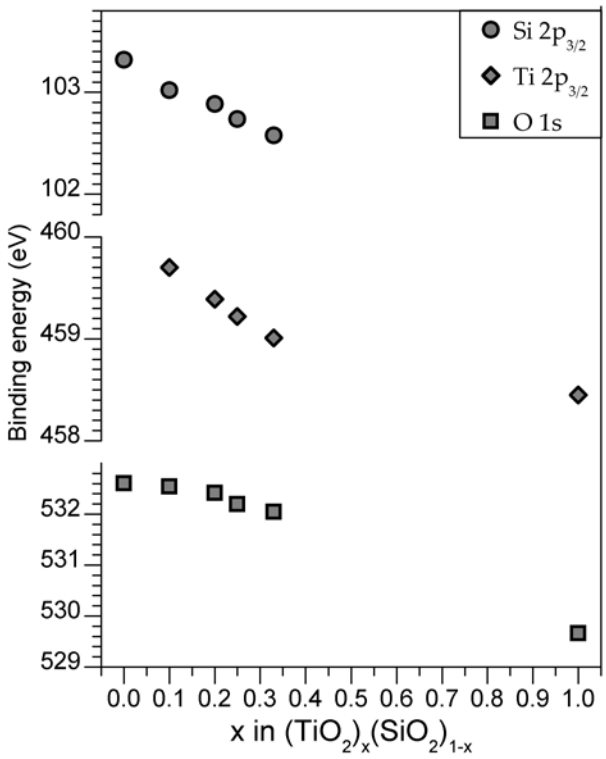

Figure 3.3. Si $2p_{3/2}$, Ti $2p_{3/2}$, and O 1s binding energy shifts with increasing Ti content (x) in $(TiO_2)_x(SiO_2)_{1-x}$. These shifts are caused by the substitution of Si by less electronegative Ti atoms, which increases the magnitude of final-state relaxation. (The Ti $2p_{1/2}$ BE shifts in an identical fashion to the $2p_{3/2}$ BE.)

As x increases from 0→1 in $(TiO_2)_x(SiO_2)_{1-x}$, the O 1s XPS BE (based on analysis of the peak maximum) decreases by 2.94 eV (**Figure 3.2a** and **Figure 3.3**). Note also in **Figure 3.2a**, the presence of a low-BE shoulder that increases in intensity and decreases in BE with increasing x. This low-BE contribution is attributed to the formation of TiO_2-rich clusters in a SiO_2 matrix, whereas the significantly more intense high-BE peak results from homogeneously mixed Ti/Si atoms. (This system is known to exhibit some heterogeneity with increasing Ti content.[47, 168, 181]) Along with shifts in the O 1s BE, the Ti $2p_{3/2}$ BE decreases by 1.25 eV as x increases from 0.1→1 and the Si $2p_{3/2}$ BE decreases by 0.74 eV as x increases from 0→0.33 (**Figure 3.2** and **Figure 3.3**).

Comparison of XPS BE shifts with XANES shifts in absorption energy for transitions in which the same core-electron is excited (*e.g.*, the Ti L_3-edge absorption energy vs. the Ti $2p_{3/2}$ BE) provides a method to isolate final-state effects, as demonstrated in Chapter 2. XPS binding energies are more strongly influenced by final-state effects because the excited electron is completely removed from the system, unlike in the XANES process, where the electron is promoted to an unoccupied conduction state, which can still provide some screening to the core-hole (*i.e.*, the $(\Delta E_i^{IA} + \Delta E_i^{EA})$ term in eq. (3.1) is minimized in the XANES excitation).[54, 78, 79]

The O K-edge XANES spectra are shown in **Figure 3.4a** and are comprised of a low-energy absorption feature (528–533 eV), owing to transitions to O 2p states interacting with Ti 3d states, and a higher-energy absorption feature (>533 eV) resulting from transitions to O 2p states interacting with Ti 4p/4s and Si 3p/3s states.[152, 189] The low-energy feature in **Figure 3.4a** increases in intensity and width with increasing Ti content, especially at high values of x. This broadening is likely due to the presence of multiple Ti coordination environments.

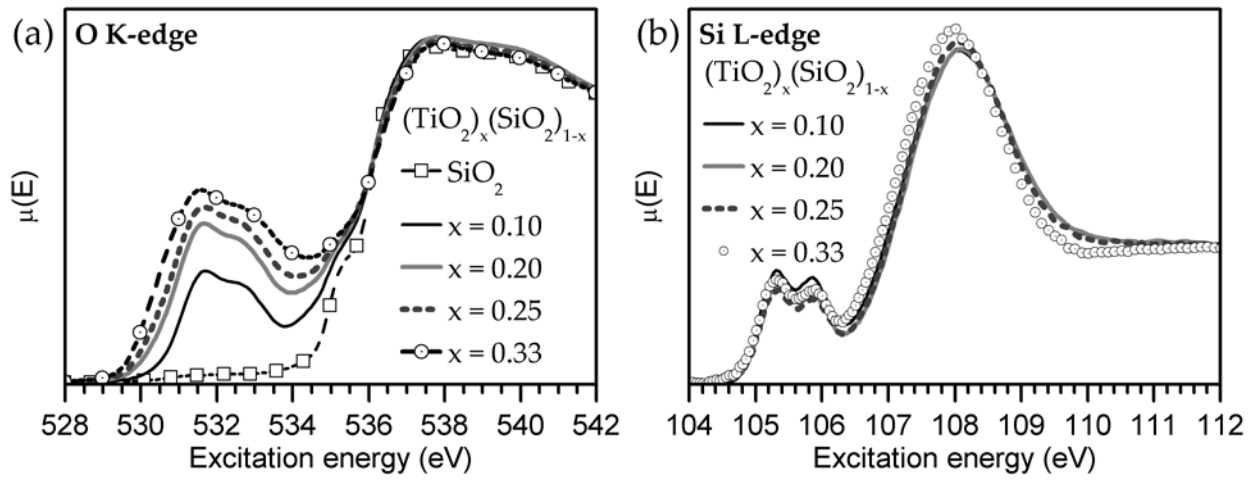

Figure 3.4. (a) O K- and (b) Si $L_{2,3}$-edge XANES spectra for annealed $(TiO_2)_x(SiO_2)_{1-x}$ materials. The O K-edge spectra show no change in absorption energy of the peak maximum of the main edge or the pre-edge, while the Si $L_{2,3}$-edge spectra shift by less than 0.1 eV over the concentration range studied.

Importantly, the energy of the peak maximum of this feature is invariant with Ti content. Additionally, the higher-energy feature shows no change in absorption energy as x increases from 0→0.33, while the O 1s BE decreases by 0.55 eV over the same concentration range ($0 \leq x \leq 0.33$; **Figure 3.3**). Such a comparison provides strong evidence that final-state effects cause the XPS BE shifts observed in the O 1s XPS spectra (**Figure 3.2a**).

To confirm the nature of the Si 2p and Ti 2p XPS BE shifts, they can also be compared to the corresponding XANES spectra (Si $L_{2,3}$-edge (**Figure 3.4b**) and Ti L_3-edge (**Figure 3.1c**). The Si $L_{2,3}$-edge spectra are composed of two regions, a low-energy region corresponding to a Si 2p→3s transition, split into $L_{2,3}$-peaks, and a higher-energy, broader region, corresponding to Si 2p→3d transitions.[201] Overall, the absorption energy of the Si $L_{2,3}$-edge spectra (**Figure 3.4b**) decreases by ≤0.1 eV as x increases from 0→0.33. This shift is significantly smaller than the corresponding decrease in the Si $2p_{3/2}$ XPS BE (*cf.* **Figure 3.3**). The Ti L_3-edge XANES (**Figure 3.1c**) absorption energy was observed to decrease by less than 0.1 eV with greater Ti content ($0.1 \leq x \leq 1.0$), while the Ti $2p_{3/2}$ BE decreased by 1.25 eV (**Figure 3.3**). (The slight decrease in the Ti L_3-edge XANES absorption energy could be due to changes in crystal-field splitting or possibly a change in the ground-state screening of the Ti nuclear charge.)

3.3.4. XANES vs. XPS

Comparison of the energy shifts observed in XANES and XPS (the O K-edge XANES spectra compared to the O 1s XPS spectra, the Si $L_{2,3}$-edge XANES spectra compared to the Si 2p XPS spectra, and the Ti L_3-edge XANES spectra compared to the Ti 2p XPS spectra) strongly supports the notion that the XPS BEs in this system are influenced by final-state effects. As slight shifts in the XANES spectra were observed, ground-state effects do influence the absorption and binding energies, but only in a minor way. Contributions to the shifts in energy

because of ground-state effects result from a change in screening of the nuclear charge of the excited atom owing to the substitution of the atoms located in the first or second coordination sphere (*i.e.*, the $\Delta\sum_{i\neq j}\frac{q_j}{r_{ij}}$ term in eq. (3.1) becomes less positive with greater concentration of less electronegative Ti atoms).

Final-state effects, that is, a change in the magnitude of final-state relaxation, can be influenced by a variety of possible contributors. In the system studied here, the replacement of nearest-neighbour or next-nearest-neighbour Si atoms ($\chi_{Si} = 1.74$) by less electronegative Ti atoms ($\chi_{Ti} = 1.32$) leads to greater final-state relaxation of the excited atom with increasing x.[36] Greater relaxation results in a lower final-state energy, and, therefore, a lower binding energy. Chapter 2 demonstrated that final-state relaxation also increases with decreasing CN, because of a more poorly-screened core-hole. (This final-state effect is mitigated during the XANES excitation as the excited electron populates conduction states, and thus still partially screens the core-hole.) However, the Ti $2p_{3/2}$ BE in the $(TiO_2)_x(SiO_2)_{1-x}$ system decreases with increasing x, despite an increase in the Ti CN, implying that although this effect may dampen the shift in BE, its effect is not significant. The increase in magnitude of the total O 1s BE shift (see **Figure 3.3**) compared to the Ti 2p BE shift ($0.1 \leq x \leq 1.0$) is a result of the Si/Ti atoms substituting in the first—rather than the second—coordination shell of O. The determination that the XPS binding energies from these amorphous silicate powders shift primarily because of final-state effects, with changes in ground-state screening playing a very minor role, is consistent with previous Auger parameter analysis of Ti silicate thin films and powders, and previous XPS studies of Hf- and Zr-silicate thin films.[54, 172-174, 191]

3.4. Conclusions

In this contribution, the $(TiO_2)_x(SiO_2)_{1-x}$ system has been investigated by soft and hard X-ray XANES and XPS and has allowed for a study of the influence of the local coordination environment on the electronic structure. This work has provided a better understanding of how the Ti coordination number (CN) changes in $(TiO_2)_x(SiO_2)_{1-x}$ depending on composition, on annealing temperature, and if the Ti atoms examined are located within the bulk of the material or at the surface. Greater knowledge of why the XPS BEs and XANES absorption energies shift with composition has also been gained.

Examination of Ti K- and L_3-edge XANES spectra revealed that the average Ti CN increases with greater Ti content (x), an effect of the larger Ti ionic radius. Comparison of the Ti K- and Ti L_3-edge XANES spectra showed, for the first time, that the average Ti CN is higher at the surface compared to within the bulk. (Within the bulk of the material, 4-, 5- and 6-coordinate Ti was observed while only 5- and 6-coordinate Ti was present at the surface.)

With increasing Ti content in $(TiO_2)_x(SiO_2)_{1-x}$, the O 1s, Si 2p, and Ti 2p XPS BEs decreased significantly, in agreement with previous studies, while the corresponding XANES spectra (involving the same excited core-electron) showed little to no shifts. As ground state effects will equally affect both, a comparison of the BE and absorption energy shifts allowed for an estimation of the contribution of final-state relaxation to the XPS BEs, which this study has shown is more significant than previously thought for these amorphous silicate powders.[191] The decrease in O 1s, Si 2p, and Ti 2p BEs with increasing Ti content is due to substitution of Si by less electronegative Ti atoms leading to greater final-state relaxation. As the Ti CN was found to increase with greater x, the shift to lower, rather than higher BEs shows that changes in final-state relaxation because of substitution of the next-nearest-neighbour atoms will dominate over

CN affects when the difference in electronegativity of the substituting atoms is sufficiently large ($\Delta\chi_{Si\text{-}Ti} = 0.4$).[114]

The amorphous transition-metal silicates ($(MO_2)_x(SiO_2)_{1-x}$; M = Ti, Zr, Hf), in either thin-film or powdered form, have received a considerable amount of interest owing to their numerous potential applications, especially as high-k dielectric replacements for SiO_2 in semiconductor devices.[40, 44, 54, 176] The increased understanding of how the CN changes depending on composition and location of the metal centres within the material, along with why the XPS BEs and XANES absorption energies shift with composition provided here will aid in optimizing these materials for such applications.

Chapter 4

4. XPS investigations of final-state relaxation in amorphous Zr and Zr/Ti silicate powders

4.1. Introduction

Amorphous transition-metal silicates (*e.g.*, $(MO_2)_x(SiO_2)_{1-x}$; *M* = Ti, Zr, Hf) have been the subject of many investigations because of their tuneable properties and industrial applications. Many of the desirable properties depend on the metal content, which can be adjusted to control the refractive index, thermal expansion coefficient, hardness, chemical durability, and dielectric constant of the materials.[42, 47, 51, 163-168, 202] TiO_2 is often incorporated into SiO_2 to make glasses with a high refractive index and ultra-low thermal expansion, ZrO_2 greatly increases the resistance to alkaline solutions, and $(HfO_2)_x(SiO_2)_{1-x}$ has been proposed as a high-*k* dielectric replacement for SiO_2 gate dielectrics in transistors.[40, 44, 164-166] (Hf-based materials are currently being used in 45 nm computer processors, though the material's identity is not specified.[35, 41]) Quaternary (*M*-*M'*-O-Si; *M, M'* = Ti, Zr, Hf) mixed-metal silicates allow the combination of beneficial properties from each of the ternary metal silicates (*M*-O-Si), creating a wealth of chemical possibilities. Yet, despite the considerable volume of work on the ternary silicates, the quaternary silicates have received considerably less attention.[46, 168, 182, 185, 203, 204]

Traditionally, silicates are made via melt syntheses; however, the high temperatures required to melt transition-metal silicates (often >1300°C) cause phase segregation and

crystallization, leading to heterogeneous products.[46, 49, 182] Consequently, low-temperature soft processing techniques, such as sol-gel synthesis, have led the way to making amorphous, homogeneous glasses with high metal content.[46, 49, 180, 205] Solution-based routes have the added benefit of a range of post-synthetic solution processing techniques, such as spin-coating for thin-film applications or fibre drawing and spinning for use in composites or textiles.[50-52] The lack of long-range order in amorphous materials hinders the use of diffraction-based techniques that are typically used to probe the structure and homogeneity. As a result, amorphous materials are ideal candidates for study by X-ray spectroscopy, which is sensitive to only the first few coordination shells of the element being examined.

In this work, amorphous $(ZrO_2)_x(TiO_2)_y(SiO_2)_{1-x-y}$, a series of quaternary metal silicates, was synthesized by sol-gel methods and investigated by X-ray absorption near-edge spectroscopy (XANES) and X-ray photoelectron spectroscopy (XPS). These mature spectroscopic techniques are routinely used to examine the electronic structure of materials in the solid state, yet many effects remain poorly understood and require further study to understand their role in spectral energy shifts. Improving our understanding of the causes of spectral energy shifts, such as the role played by the next-nearest neighbour (NNN), is critical to the continuing development of these powerful techniques as probes of electronic structure. Towards this goal, this work examines changes in XANES lineshape, changes in XANES absorption and XPS binding energy shifts, and changes in the Auger parameter of these materials to determine the contribution of final-state relaxation. Chapter 3 drew attention to shifts in binding energy (BE) owing to electronegativity differences; however, there were noticeable changes in the Ti coordination number (CN) that could have muted the observed shift in BE. The current chapter expands upon this work by examining the more complex quaternary silicates, where the effect of

metal identity and changes in average CN have been examined. Additionally, Auger spectra have been collected and extraction of the O KLL Auger parameter has been used to confirm that increasing final-state relaxation leads to considerable BE shifts in the metal silicates.

4.2. Experimental

4.2.1. Synthesis of $(ZrO_2)_x(SiO_2)_{1-x}$ and $(ZrO_2)_x(TiO_2)_y(SiO_2)_{1-x-y}$

The amorphous quaternary $[(ZrO_2)_x(TiO_2)_y(SiO_2)_{1-x-y}$ $(x + y = 0.20, 0.30)]$ and ternary $[(ZrO_2)_x(SiO_2)_{1-x}$ $(x = 0.10, 0.20, 0.25, 0.33, 0.50)]$ silicates were synthesized using a sol-gel method.[47, 180] The precision of the stoichiometry in these materials is believed to be better than x,y ±0.02, as supported by the close agreement with XPS BE shifts of ternary silicates having a similar metal content, and the smooth evolution of spectral features in the O K-edge spectra from quaternary and ternary silicates with varying metal content (*vide infra*). All reactions were carried out under a N_2 atmosphere with constant stirring. The reaction solution was diluted with a stoichiometric amount of anhydrous ethanol *before* addition of each metal-organic precursor (20 equivalents of EtOH were added per molar equivalent of Ti- and Zr-alkoxide precursor), and the precursors were reacted in order of increasing reactivity—Si, Ti, then Zr—to promote the formation of homogeneous products.[182, 206] The less reactive Si-alkoxide was prehydrolyzed by combining tetraethyl orthosilicate (≥99%, Sigma Aldrich), ethanol (anhydrous), and water in a 1:2:1 molar ratio with catalytic amounts of HCl.[180] This solution was stirred under reflux at 80°C for 2 hours and then cooled to room temperature. Ethanol was added to dilute the solution, after which titanium (IV) tert-butoxide (99.95%, Strem) was added drop-wise. After stirring for one hour, ethanol was added and zirconium (IV) tert-butoxide (99%, Strem) was added drop-wise with stirring. After continued stirring, water was added drop-wise to increase the water:alkoxide (Ti, Zr, and Si alkoxide) molar ratio to 2:1. The mixture was then sealed under N_2 and stirred

until a gel formed (7-21 days), after which the material was exposed to the atmosphere for >7 days. (Higher Ti content and/or overall metal content reduced the time required to gel.) Powders were obtained by placing the resulting materials (transparent glasses) under vacuum for >24 hours, grinding with a mortar and pestle, and then annealing them in air at 550°C for 12 hours to remove residual organic material. The formation of these materials was confirmed by use of Fourier transform infrared spectroscopy, and the lack of long-range order, even after annealing at temperatures up to 550°C, was confirmed by powder X-ray diffraction using Cu Kα radiation generated from a Rigaku Rotaflex RU-200 rotating anode X-ray diffractometer.[47, 168, 182]

4.2.2. XANES

4.2.2.1. Ti and Zr K-edge

Ti and Zr K-edge XANES spectra were collected using the Pacific Northwest Consortium/X-ray Science Division Collaborative Access Team (PNC/XSD-CAT, Sector 20) bending magnet beamline (20BM) located at the Advanced Photon Source (APS), Argonne National Laboratory. A silicon (111) double crystal monochromator was used, providing a photon flux of ~10^{11} photons/second and a resolution of 0.7 eV at 5000 eV, and 2.5 eV at 18000 eV ($\Delta E/E = 1.4 \times 10^{-4}$). Finely ground samples were sandwiched between Kapton tape, and positioned 45° to the X-ray beam. Transmission spectra were measured with N_2-filled ionization chambers and partial fluorescence spectra were collected using a Canberra 13-element Ge detector. Comparison with transmission spectra showed no self-absorption effects in the fluorescence spectra presented here. The X-ray energy was increased by 0.15 eV per step through the Ti K absorption edge and 0.3 eV per step through the Zr K-edge. Spectra were calibrated by comparison to spectra collected concurrently in transmission mode from Ti and Zr

metal, which have well-known edge absorption energies (4966 eV and 17998 eV, respectively).[87] The Ti K-edge spectrum from anatase (TiO_2; 99.6%, Alfa Aesar) was also collected to provide a standard for comparison of pre-edge peak intensities and absorption energies. The precision of the measurements is estimated to be better than ±0.1 eV, as determined by comparison of spectra from samples and standards collected throughout these studies.

4.2.2.2. Ti $L_{2,3}$-, O K-, and Si K-edge

Ti $L_{2,3}$-, O K-, and Si K-edge XANES spectra from $(ZrO_2)_x(TiO_2)_y(SiO_2)_{1-x-y}$ were collected using the Spherical Grating Monochromator beamline (SGM, 11ID-1) located at the Canadian Light Source (CLS).[120] The flux is ~10^{11} photons/second at 1900 eV and increases to ~4×10^{12} photons/second at 250 eV. The resolution is better than 0.3 eV at photon energies below 1500 eV ($\Delta E/E < 2 \times 10^{-4}$) and the precision of the measured absorption energies is better than ±0.1 eV. Spectra from powders of the material pressed on carbon tape were collected in total-electron (TEY; Ti $L_{2,3}$-edge and Si K-edge) and fluorescence (FLY; O K-edge) yield mode. Through the absorption edge, the photon energy was increased by 0.1 eV per step for Ti $L_{2,3}$-edge and O K-edge measurements, and 0.15 eV per step for Si K-edge measurements. The Ti $L_{2,3}$- and O K-edge spectra were calibrated by collecting spectra from Ti metal and Cr metal, respectively, which have well known Ti L_3- (453.8 eV) and Cr L_3-edge (574.1 eV) absorption energies.[87] Si K-edge spectra were calibrated using fused silica (SiO_2; 99.99%, Alfa Aesar), whose edge absorption energy was taken to be 1847.0 eV.[207]

4.2.2.3. Si $L_{2,3}$-edge

The Si $L_{2,3}$-edge XANES spectra from $(ZrO_2)_x(TiO_2)_y(SiO_2)_{1-x-y}$ were collected using the Variable Line Spacing Plane Grating Monochromator beamline (VLS PGM, 11ID-2) at the CLS.

The flux is 2×10^{12} photons/second at 80 eV, the resolution is better than 0.01 eV at 100 eV ($\Delta E/E = 1 \times 10^{-4}$), and the precision of this beamline is better than ±0.1 eV. The FLY spectra from powdered samples pressed on carbon tape were collected by stepping the excitation energy through the absorption edge at 0.05 eV increments. The spectra were calibrated by comparison to a spectrum from a Si wafer having a Si L_3-edge absorption energy of 99.4 eV.[87] All XANES spectra represent the average of multiple scans of each absorption edge, and were analyzed using the Athena software program.[123]

4.2.3. XPS

XPS spectra were collected using a Kratos AXIS 165 spectrometer and a monochromatic Al Kα (1486.7 eV) X-ray source. The resolution of this instrument has been determined to be 0.4 eV and the precision of the measured binding energies is better than ±0.10 eV.[193] Finely ground powders of $(ZrO_2)_x(TiO_2)_y(SiO_2)_{1-x-y}$, TiO_2 (anatase), SiO_2 (99.99%, Alfa Aesar), and monoclinic ZrO_2 (99.7%, Alfa Aesar) were pressed into In foil and mounted on an electrically grounded sample holder. High-resolution spectra of the Ti 2p, Si 2p, O 1s, and C 1s core lines were collected using a pass energy of 20 eV, a step size of 0.05 eV, and a sweep time of 180 seconds. To counter surface charging, a charge neutralizer was used to direct low-energy electrons toward the samples during collection of all spectra. (Ar^+ ion etching was not used to clean the surface of the samples, as testing on related materials showed preferential reduction of Ti (Section 3.2.3).) All spectra were calibrated using the C 1s core-line arising from adventitious C with a fixed value of 284.8 eV. Charge neutralization and calibration using adventitious C has been previously shown to be effective for analyzing these materials.[55] A Shirley-type function was applied to remove the background arising from energy loss and spectra were fitted using synthetic peaks having a combined Gaussian (70%) and Lorentzian (30%) line profile.[125] The Si

$2p_{3/2}$ BE was found by fitting the Si 2p core-line envelope with two peaks (Si $2p_{3/2}$ and Si $2p_{1/2}$) having a 2:1 peak area ratio ($2p_{3/2}$:$2p_{1/2}$).

4.2.4. Electronic structure calculations

To confirm the interpretation of the complicated O K-edge XANES spectra, full-potential linear muffin-tin orbital (FP-LMTO) calculations were performed using LMTART 7 to determine the total and partial (O 2p, Ti 3d, Zr 4d) density of unoccupied states.[208-211] Owing to difficulties inherent in modeling amorphous systems, calculations were performed for crystalline systems ($ZrSiO_4$ and $TiSiO_4$), though previous studies using this model have accurately reproduced properties (*e.g.*, the dielectric constant) of the amorphous silicates investigated here.[45, 212, 213] Further, as the materials investigated in this study contain a solid solution of Ti and Zr atoms, the true electronic structure likely lies somewhere between the two substitutional end-members modeled here ($ZrSiO_4$ and $TiSiO_4$). Self-consistency was achieved by requiring the convergence of the total energy to be smaller than 10^{-4} eV per unit cell, and the Brillouin zone integration was performed over 1000 *k*-points (10×10×10) using the tetrahedron method.[214, 215] Crystallographic parameters of $ZrSiO_4$ and $TiSiO_4$ used for the calculations were taken from literature.[216, 217] Parameters for $TiSiO_4$ were taken from a theoretical study, as the structure-type of $TiSiO_4$ is not thermodynamically stable under ambient conditions.[217]

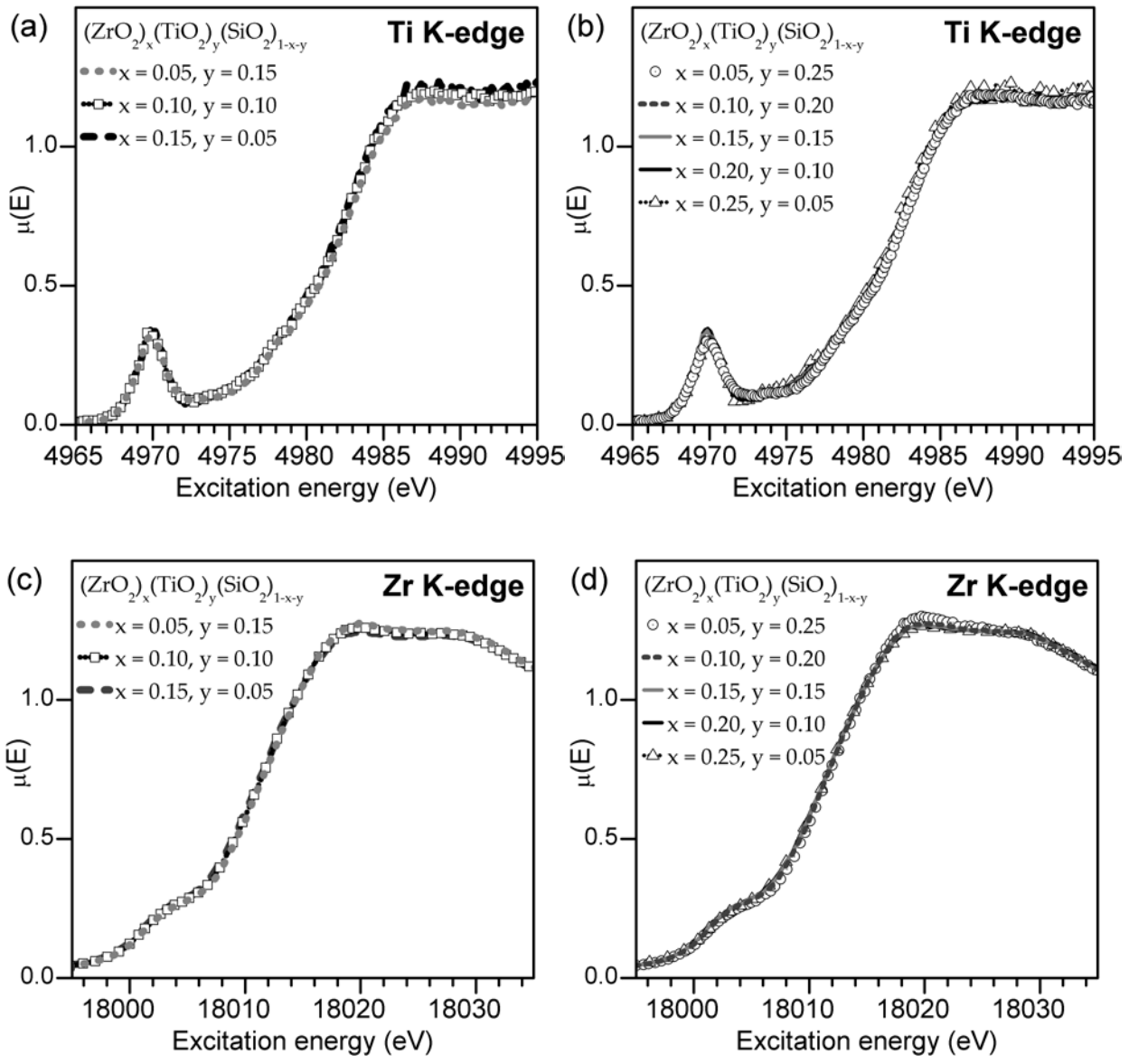

Figure 4.1. Ti (a, b) and Zr (c, d) K-edge XANES spectra from $(ZrO_2)_x(TiO_2)_y(SiO_2)_{1-x-y}$ with a fixed total metal content (x + y) of 20 mol % (a, c) and 30 mol % (b, d). The lack of changes in the lineshape is evidence that there is no significant change in either the Zr or Ti coordination number (CN) with increasing metal content.

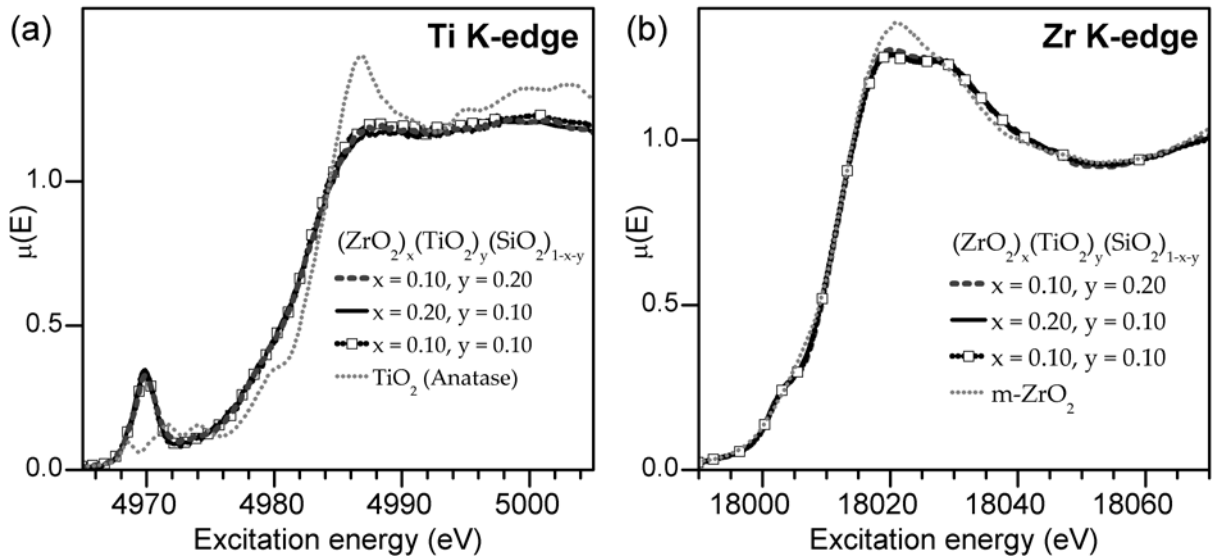

Figure 4.2. a) Ti K-edge XANES spectra of the quaternary silicates show no change with increasing *total* metal content, indicating there is no significant change in the Ti coordination number (CN). A spectrum from TiO_2 (anatase) is presented as an example of the lineshape expected if the Ti CN was 6. b) Zr K-edge XANES spectra from the quaternary silicates also show no change with *total* metal content. The spectra are displayed over a wider energy range to highlight the overall lineshape. A spectrum from monoclinic ZrO_2 is presented as an example of the lineshape expected if the Zr CN was 6.

4.3. Results and discussion

4.3.1. Transition metal K-edge XANES

Transition metal K-edge XANES spectra were collected to examine how the Ti and Zr coordination number (CN) change as a function of the total metal content and Zr:Ti ratio (**Figure 4.1** and **Figure 4.2**). Metal K-edge spectra result from 1s → (*n*–1)d (quadrupolar, pre-edge) and 1s → *n*p (dipolar, main-edge) transitions, which are sensitive to changes in CN.[105, 106, 110-112, 135, 136, 138] The higher energy and more intense, dipolar portion of the spectrum (*i.e.*, the main-edge, above ~4980 eV for Ti and ~18010 eV for Zr) decreases in energy and intensity with lowering CN. This is a result of poorer screening of the core-hole and reduced number of metal-ligand states (*e.g.*, Ti 4p – O 2p or Zr 5p – O 2p) available for 1s electrons to be excited to.[111, 112, 142-145] The main edge absorption energy is also characteristic of the metal oxidation state, which was found to be 4+ for both Zr and Ti in these materials. Significant changes are also observed in the Ti K pre-edge region (4965-4975 eV). As the CN decreases from 6, inversion symmetry is lost and the Ti 3d states are overlapped partially by 4p states, lending a dipolar component to the excitation and causing the pre-edge peak intensity to increase.[135, 136, 138] Although changes in the Zr K pre-edge also occur, they are more difficult to follow because the pre-edge is partially obscured by the main edge. This happens because the unoccupied d- and p-states (4d and 5p, respectively) are closer in energy, and also because the core-hole lifetime broadening increases and instrumental resolution decreases with greater excitation energy.

4.3.1.1. Ti K-edge XANES

Owing to the larges changes in the lineshape of metal K-edge spectra with CN, the coordination environment of Ti in silicates and oxides has been previously investigated using XANES. By comparison of the lineshape to standards with known structures, the average CN of

elements in the amorphous silicates can be estimated.[106, 110] This is readily done by analysis of the intensity and energy of the pre-edge peak, which can be used to determine the Ti CN and the relative concentration of 2-component mixtures where the Ti CN is 4, 5, and/or 6.[106, 109, 192, 194] However, when all three coordination environments coexist, precise determination is not possible using only this method. Examination of the Ti K pre-edge peak intensities and energies from the materials studied here, compared to those from materials reported in other studies, suggest Ti centres in the bulk of $(ZrO_2)_x(TiO_2)_y(SiO_2)_{1-x-y}$ are primarily 5-coordinate, with contributions from 4-coordinate Ti, though minor contributions from 6-coordinate Ti cannot be discounted (**Figure 4.1a**,**b**).[106, 218] More importantly for the scope of this study, the pre-edge intensities and energies are extremely sensitive to *changes* in the Ti CN; however, no changes were observed as a function of metal content (**Figure 4.2**). These results were confirmed by Ti $L_{2,3}$-edge spectra collected from these materials (Section 4.3.3), which exhibit lineshapes consistent with 5-coordinate Ti, and which show no large changes in lineshape or edge absorption energy with metal content.

4.3.1.2. Zr K-edge XANES

The Zr coordination environment in $(ZrO_2)_x(SiO_2)_{1-x}$ and $(ZrO_2)_x(TiO_2)_y(SiO_2)_{1-x-y}$ has previously been studied using extended X-ray absorption fine-structure (EXAFS) modeling and XANES through analogy to known crystalline structures.[168, 186, 219] In agreement with a previous XANES study, the Zr K-edge lineshapes shown here have a more pronounced pre-edge shoulder and a flat, double-peaked main-edge, and show virtually no change when the total metal content ((x + y, mol % ZrO_2 + TiO_2) is constant (**Figure 4.1c**,**d**).[168] The spectra are presented over an expanded energy region to show the overall lineshape, which is most similar to the lineshape of cubic and tetragonal ZrO_2, where Zr is 8-coordinate (**Figure 4.2**).[163, 168] However, the assignment

of CN is tentative because the silicates studied here are amorphous, and structural differences can cause the lineshape to change. Although quantitative assignment is not possible in this case, the Zr CN is certainly >6, which is higher than Ti in these materials. (EXAFS studies do give quantitative results, but the large errors obtained for these materials make assignments equally ambiguous.[163, 168]) Also—as was the case with Ti—no changes were observed in the Zr K-edge spectra with increasing total metal content (**Figure 4.2**), indicating the Zr CN does not change throughout the series.

4.3.1.3. The coordination number of Ti and Zr

In summary, Ti K-edge XANES spectra of the quaternary silicates show no significant changes in lineshape, energy, or intensity with increasing metal content or Zr:Ti ratio (**Figure 4.1a**,**b**). Zr K-edge spectra are equally static as a function of metal content, evidence that there is no significant change in the average CN of Zr (**Figure 4.1c,d**). Because even minute mixing of p- and d-states leads to a large increase in the pre-edge intensity, the lack of drastic changes in either the Zr or Ti K-edge XANES spectra is evidence there are no large changes in either Zr or Ti CN with increasing metal content. This differs from the ternary Zr- and Ti-silicates, where an increase in the average metal CN—albeit a small increase—was seen with increasing metal content (see Chapter 3 and reference 112). It was shown in Chapter 2 that a decrease in the average CN increases the magnitude of final-state relaxation, so the lack of large change in average metal CN in the silicates studied here removes a potential contributor to any shifts in XPS BE. Although exact quantification of the average CN is not possible, Ti appears to be predominantly 5-coordinate, and the Zr CN is >6, likely due to its larger size.

4.3.2. Zr $3d_{5/2}$, Ti $2p_{3/2}$, Si 2p, and O 1s XPS binding energy (BE) shifts

To investigate the changes in electronic structure as the identity and concentration of the metal is changed, high-resolution Zr 3d, Ti 2p, Si 2p, and O 1s core-line XPS spectra were collected. As was demonstrated in previous chapters, the photoelectron BEs can change as a result of shifts in the ground- and/or final-state energies, though the cause of the shift cannot be determined by XPS alone.[56, 220, 221] To describe why BEs shift, a version of the charge potential model is shown in eq. (4.1), where ground- and final-state effects have been grouped together in the first and second set of parentheses, respectively.[56]

$$\Delta E_i = E_i - E_i^0 = (k\Delta q_i + \Delta \sum_{\mathrm{i\neq j}} \frac{\mathrm{q_j}}{\mathrm{r_{ij}}}) - (\Delta E_i^{\mathrm{IA}} + \Delta E_i^{\mathrm{EA}}) \qquad (4.1)$$

The total binding energy shift, ΔE_i, which is the difference between the measured binding energy of the atom of interest, E_i, and a reference binding energy, E_i^{o}, consists of a number of contributions. This shift in BE occurs due to changes *at* and *around* the absorbing atom, given by the first and second terms, respectively, in each set of parentheses in eq. (4.1). In the ground state (also called the initial state), shifts in BE result from changes in the screening of the nuclear charge of the atom being excited, *i*. Here, the $k\Delta q_i$ term describes changes in the charge of the atom being excited (Δq_i), while the $\Delta \sum_{\mathrm{i\neq j}} \frac{\mathrm{q_j}}{\mathrm{r_{ij}}}$ term (often called the Madelung potential) describes changes in the charge of atoms (*j*) located *around* atom *i* at a distance r_{ij}.[56] (*k* is a parameter that describes the Coulombic interaction between core and valence electrons.[75]) In the final state, changes in the magnitude of intra- (IA) and extra-atomic (EA) relaxation result from changes in the ability of electrons to screen the core-hole produced by removing a photoelectron. Here, the $\Delta E_{\mathrm{i}}^{\mathrm{IA}}$ and ΔE_i^{EA} terms represent changes in the final-state relaxation of electrons *at* and *around* atom *i*, respectively, with $\Delta E_{\mathrm{i}}^{\mathrm{IA}}$ often being negligible.[56]

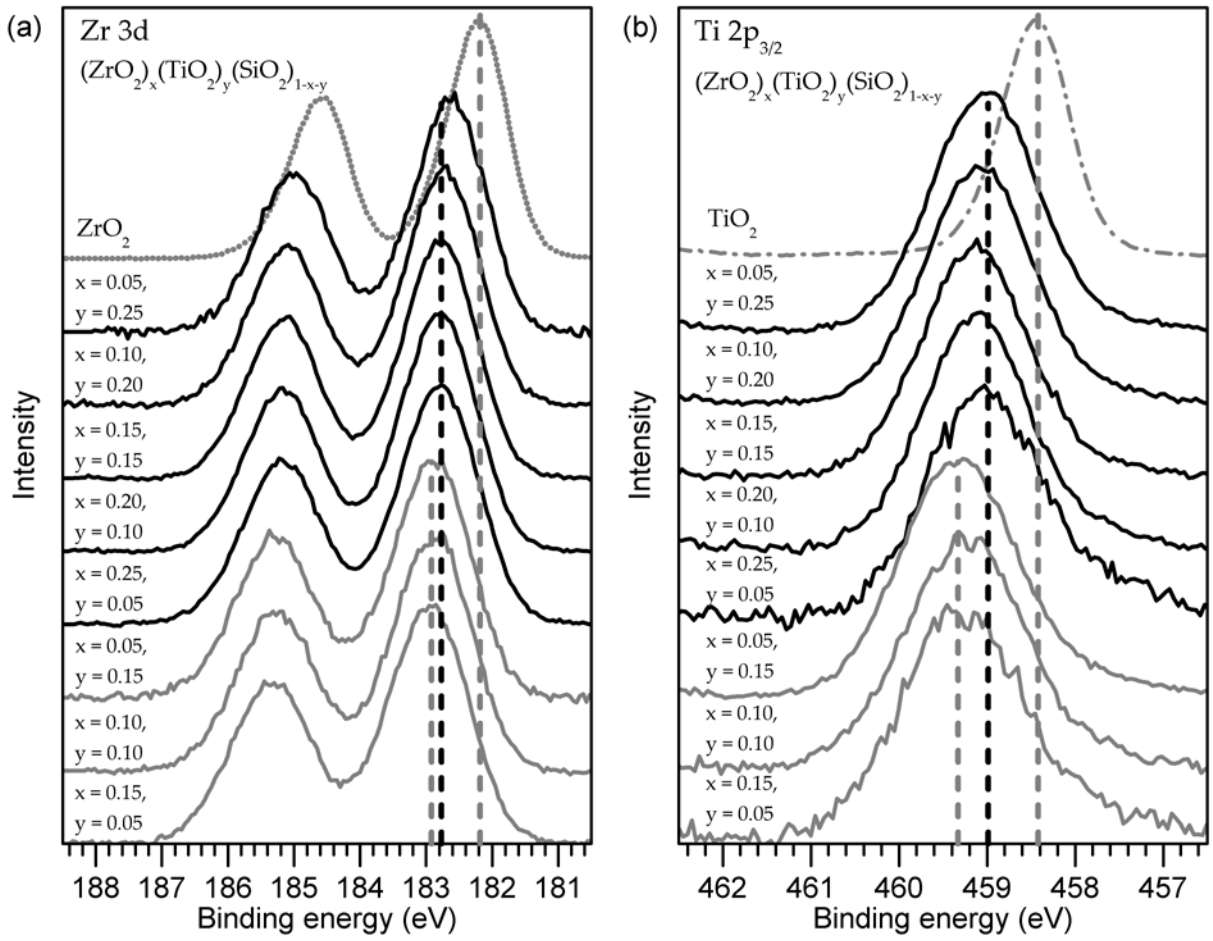

Figure 4.3. (a) Zr 3d and (b) Ti $2p_{3/2}$ XPS core-line spectra of the quaternary silicates and binary oxides. Dashed lines are a guide to indicate the approximate peak maximum for a set of spectra at a given total metal content, [x + y] in $(ZrO_2)_x(TiO_2)_y(SiO_2)_{1-x-y}$. The Zr 3d and Ti 2p binding energies (BE) decrease with increasing total metal content. (Small variations (±0.1 eV) were observed between samples with identical total metal content, though these variations are near the limits of instrumental precision (±0.1 eV) and lack a monotonic trend.)

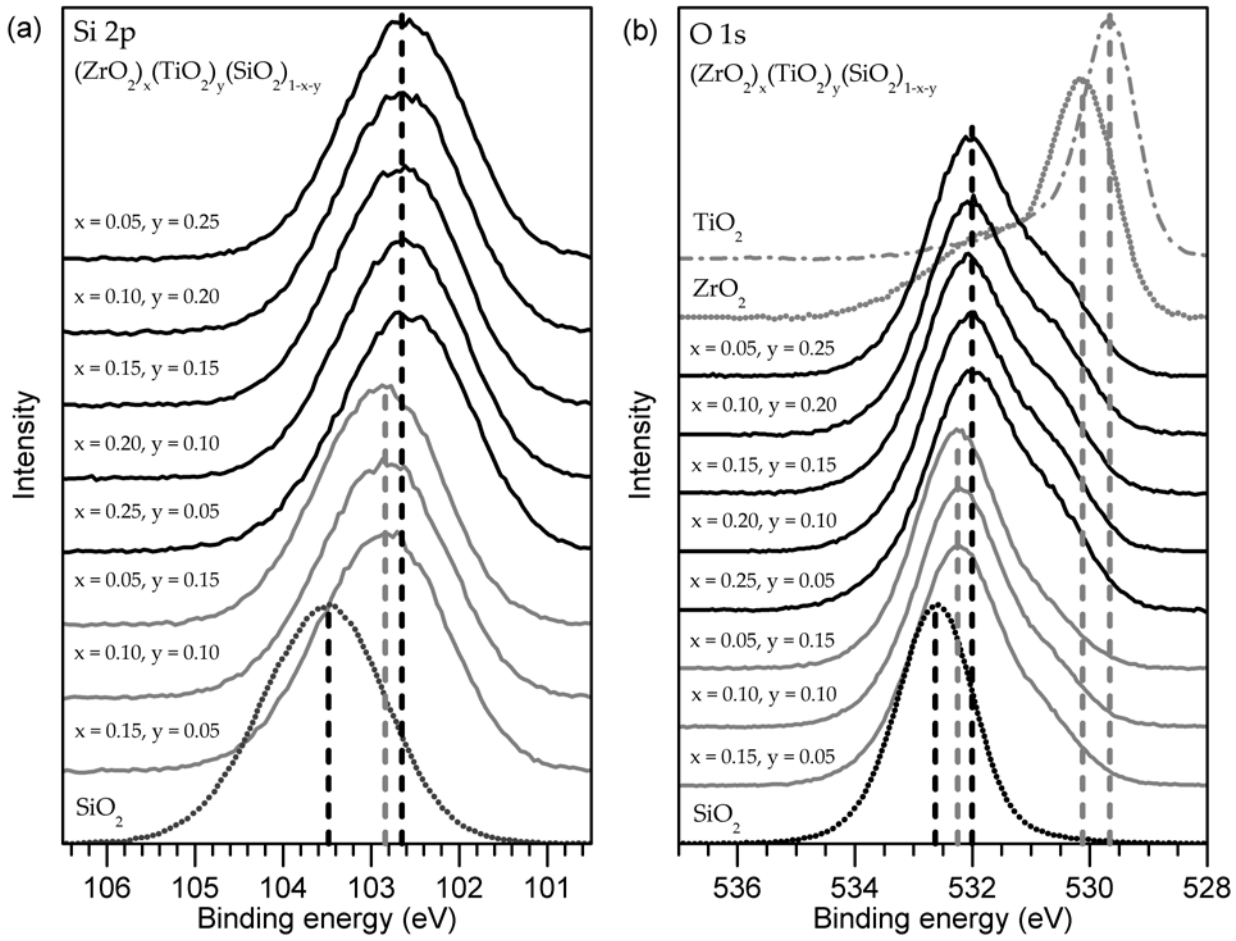

Figure 4.4. (a) Si 2p and (b) O 1s XPS core-line spectra of the quaternary silicates and binary oxides. Dashed lines are a guide to indicate the approximate peak maximum for a set of spectra at a given total metal content, [x + y] in $(ZrO_2)_x(TiO_2)_y(SiO_2)_{1-x-y}$. The Si 2p and O 1s binding energies (BE) decrease with increasing total metal content. The O 1s spectra of the quaternary silicates have a shoulder at low BE that increases in intensity with metal content. This peak is the result of metal-rich domains, which are known to exist in metal silicates at high metal loadings.[47, 181, 186, 191]

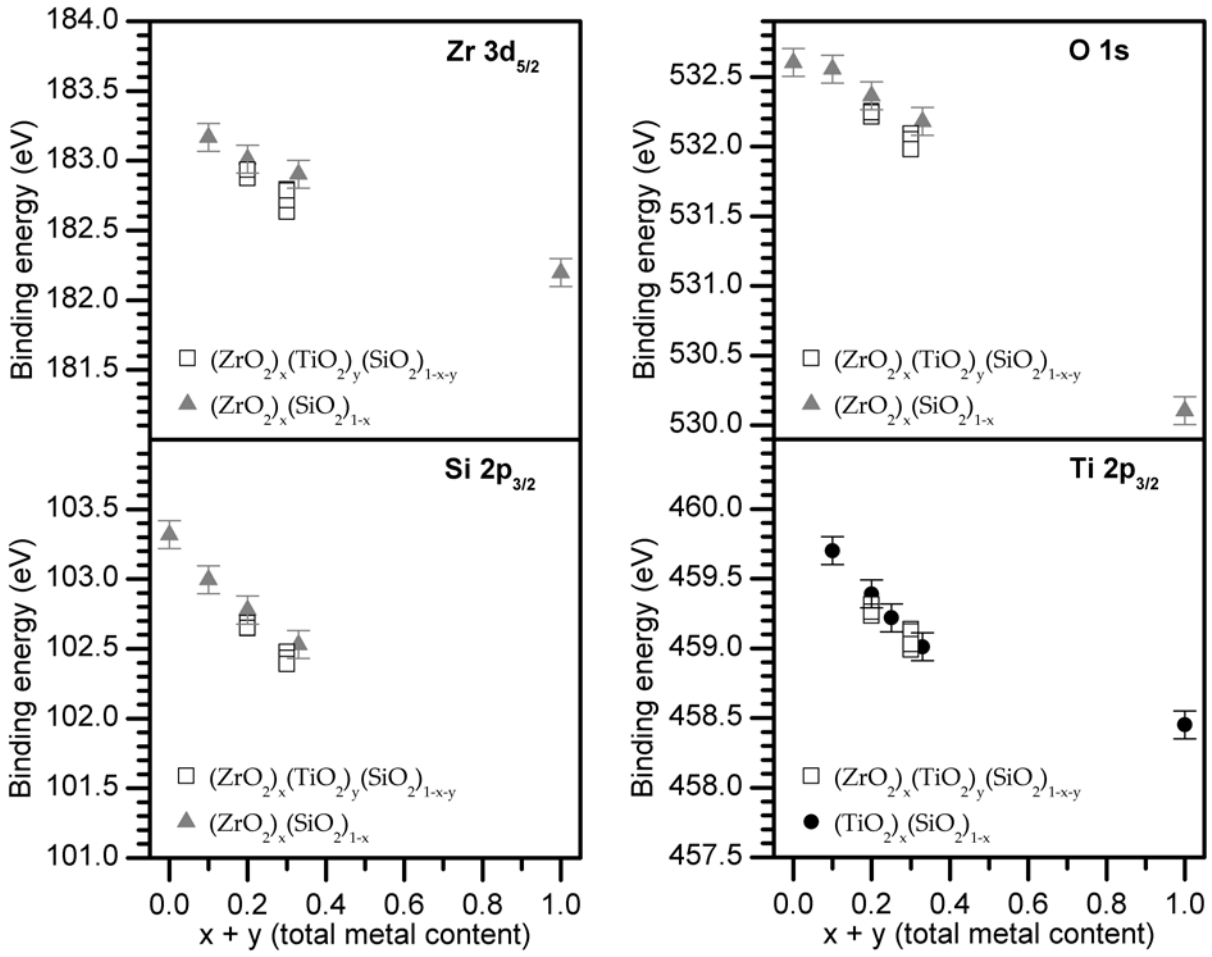

Figure 4.5. The binding energy (BE) of the photoelectron peak maximum decreases with increasing total metal content (mol % ZrO_2 + TiO_2).

To study how increasing the total metal content affects the electronic structure of these materials, XPS core-line spectra from $(ZrO_2)_x(TiO_2)_y(SiO_2)_{1-x-y}$ were collected (**Figure 4.3** and **Figure 4.4**). All core-line photoelectron peaks (Zr $3d_{5/2}$, Ti $2p_{3/2}$, Si 2p, and O 1s) show a significant decrease in BE with increasing total metal content (x + y, mol % ZrO_2 + TiO_2), but show little to no variation in BE when the total metal content is fixed and the Zr:Ti ratio is varied. The O 1s spectra of the quaternary silicates exhibit a shoulder at low BE that increases in intensity with metal content (**Figure 4.4b**). This low-BE contribution is attributed to the formation of metal-rich domains in the SiO_2 matrix, whereas the significantly more intense high-BE peak results from homogeneously mixed transition-metal and Si atoms.[191] This heterogeneity is known to occur in metal silicates at higher metal loadings, as shown in Chapter 3 and elsewhere.[47, 181, 186] Additionally, the O 1s spectrum of the monoclinic ZrO_2 (*m*-ZrO_2) standard shows a high-BE shoulder at energies characteristic of surface adsorbates, which is understandable given that the standard was not pre-treated by Ar^+ sputtering and/or *in vacuo* annealing.[222]

To make analysis feasible for the many samples investigated, the BE of the photoelectron peak maximum is plotted as a function of total metal content (**Figure 4.5**). BEs from ternary silicates are also plotted to show the close agreement with values obtained from the quaternary silicates at similar total metal content (≤0.1 eV difference when the total metal content is identical). (Core-line spectra from $(TiO_2)_x(SiO_2)_{1-x}$ are reported in Chapter 3.) As the total metal content increases, the variation of the quaternary BEs at a fixed total metal content increases, though there is no monotonic trend in BE as the Zr:Ti ratio is changed (see **Figure 4.3** and **Figure 4.4** for the individual spectra), and the small deviations are at the limits of instrumental precision (±0.1 eV). Such small deviations may be due to minor differences in synthetic

conditions or heterogeneity, the latter of which is well known in metal silicates at high metal content, and can be seen in the O 1s spectra of these materials (**Figure 4.4b**).[47, 181, 186] Also, although the BEs generally agree within the precision of the measurements, the decrease in the ternary $(ZrO_2)_x(SiO_2)_{1-x}$ BEs appears to be slightly less than in the quaternary silicates, particularly at higher metal loadings (**Figure 4.5**). These small differences between the ternary and quaternary metal silicates may be caused by changes in the average Zr CN in $(ZrO_2)_x(SiO_2)_{1-x}$, which increases slightly with increasing metal content (*cf.* the quaternary silicates, where Zr K-edge spectra showed that the Zr CN remains unchanged, as shown in **Figure 4.2b**).[112] The small changes in CN seen in the ternary silicates could cause the BEs to be slightly higher than the BEs from the quaternary silicates, for similar reasons to those highlighted in Chapter 2.

As the total metal content (x + y) increases from 0.1→1, the Zr $3d_{5/2}$, Ti $2p_{3/2}$, and O 1s BEs decrease by 1.0, 1.3, and 2.5 eV, respectively. Although a similar compositional range is not accessible for Si, the Si $2p_{3/2}$ BE decreases by 0.9 eV from (x + y) = 0→0.3. It is clear that there are large decreases in BE with increasing total metal content, but the underlying cause of the BE shift is unknown without the aid of other techniques. For example, substitution of Si^{4+} atoms by more electropositive Ti^{4+} or Zr^{4+} atoms ($\chi_{Si} = 1.74$, $\chi_{Ti} = 1.32$, $\chi_{Zr} = 1.22$) may increase final-state relaxation experienced by electrons in the material (increasing ΔE_i^{EA} in eq. (4.1), and decreasing the BE). Alternatively, this substitution could lead to more electron density *at* and/or *around* the absorbing atom in the ground-state (decreasing $k\Delta q_i$ and/or $\Delta\sum_{i\neq j}\frac{q_j}{r_{ij}}$ in eq. (4.1), and decreasing the BE).[56, 114, 220, 223] Additionally, the incorporation of metal centres into the materials will increase the average bond distances ($r_{Si4+\,(CN:4)} = 0.26$, $r_{Ti4+\,(CN:5)} = 0.51$, $r_{Zr4+\,(CN:8)} = 0.84$), which could also affect $\Delta\sum_{i\neq j}\frac{q_j}{r_{ij}}$.[56, 128, 220]

4.3.3. Ti $L_{2,3}$-, Si $L_{2,3}$-, and O K-edge XANES

To determine the origin of the BE shifts in the XPS core-line spectra, soft X-ray XANES spectra (Ti $L_{2,3}$-, Si $L_{2,3}$-, and O K-edge) were collected and compared to the corresponding XPS spectra (Ti 2p, Si 2p, and O 1s). XANES absorption energies shift for similar reasons as XPS BEs, and shifts in absorption energy can be explained by the same charge potential model introduced for XPS in eq. (4.1). The important difference between XANES and XPS lies in the final state produced by each method. In XPS, the final state of the system being probed is electron deficient and has an unscreened core-hole (the core electron having been removed from the material), so relaxation effects due to the core-hole are greater than in XANES (where the core electron is promoted to conduction states and can partially screen the core-hole).[54, 78, 79] Thus, when the ground state is identical and electrons of equal energy (*i.e.*, the same orbital) are probed by both techniques (*e.g.*, Ti $2p_{3/2}$ XPS and Ti L_3-edge XANES), the difference in the final state of analogous XPS and XANES excitations can be exploited to resolve ground- and final-state effects in XPS BE shifts. Additionally, the lineshape of Ti $L_{2,3}$- and Si $L_{2,3}$-edge spectra can be used to determine the coordination environment around these elements.

4.3.3.1. Ti $L_{2,3}$-edge XANES

Ti $L_{2,3}$-edge spectra result from the excitation of Ti 2p electrons to unoccupied Ti 3d states, and are sensitive to both the local CN and the electronic structure (Section 3.3.2).[78, 224] Ti $L_{2,3}$-edge spectra are split into the L_3 and the L_2 components as a result of spin-orbit coupling, and each component is split by bonding interactions (*e.g.*, crystal field splitting).[78, 225] (These peaks are further broadened by multiplet interactions.[226, 227]) In general, although the L_2 component is more poorly resolved than the L_3 (due to broadening from shorter core-hole lifetimes), the spectral features in both edges are consistent.[226, 228] Previous studies have assigned

the multiple peaks of the L_3 or L_2 components to transitions with energies reflective of the splitting in Ti 3d orbital energies.[188] For example, when Ti is in an octahedral environment, a low-energy peak is attributed to transitions involving t_{2g} states, and a high-energy peak is attributed to e_g* states.

Owing to the complex lineshape and numerous spectral features, Ti $L_{2,3}$-edge spectra are characteristic of the Ti CN, and comparison to crystalline standards with known CNs allows the estimation of the Ti CN.[188] The L_3-edge spectra show 2 peaks, and the largest distinguishing factor between spectra from Ti having different CNs is the ratio between high- and low-energy peak intensities, which is large when Ti is 5-coordinate (~3), and small when Ti is either 4- or 6-coordinate (~1).[188] (The L_2-edge shows similar changes.[188]) The $L_{2,3}$-edge spectra collected from the quaternary silicates studied here have lineshapes that are characteristic of 5-coordinate Ti (**Figure 4.6a**), though the presence of other-coordinate species in small amounts cannot be ruled out.[188] Further, the lineshape remains largely unchanged with increasing total metal content, suggesting the Ti CN is constant. These findings are consistent with findings from the Ti K-edge spectra, presented earlier (Section 4.3.1). As a point of contrast to the ternary silicates, the rather undramatic lack of change differs from the $(TiO_2)_x(SiO_2)_{1-x}$ system, where the more surface-sensitive Ti L_3-edge spectra showed a slight increase in the Ti CN with increasing total metal content (Section 3.3.2). Monitoring structural changes is important for characterization, as changes in CN have been shown to influence BEs. However, examining shifts in XANES absorption energies is necessary to determine whether the ground-state energies are changing. The Ti L_3-edge spectra (**Figure 4.6a**) showed no change in the L_3-edge absorption energy (<0.1 eV, determined by the maximum in the first derivative shown in **Figure 4.6a**), indicating that ground-state effects are not responsible for the Ti 2p BE shift observed by XPS.

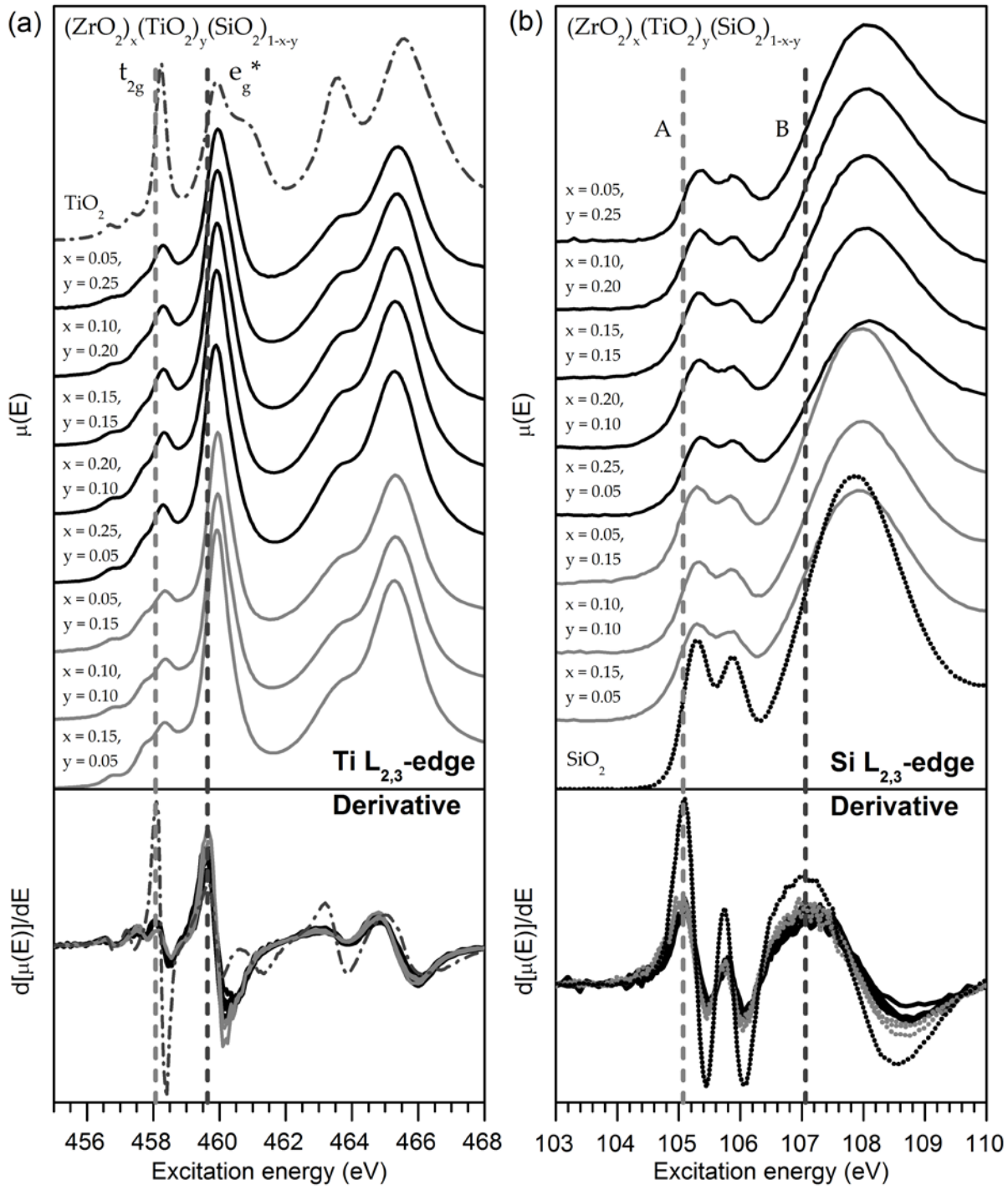

Figure 4.6. (a) Ti $L_{2,3}$-edge and (b) Si $L_{2,3}$-edge XANES spectra of the quaternary silicates. Dashed lines are a guide to indicate the edge absorption energy, which is taken to be the peak maximum in the first derivative. In both sets of spectra, a <0.1 eV shift was observed across the series as the total metal content is changed, indicating there is no change in ground-state energies. Spectra from TiO_2 (anatase) and SiO_2 (fused silica) standards are shown as examples of the lineshape expected if the Ti^{4+} CN was 6 and/or the Si^{4+} CN was 4.

4.3.3.2. Si $L_{2,3}$-edge XANES

Si $L_{2,3}$-edge spectra were also collected to probe the Si CN and changes in the ground-state electronic structure (**Figure 4.6**). The Si $L_{2,3}$-edge spectra have features due primarily to Si 2p→3s transitions at lower energies, followed by a broader region at higher energies involving largely 2p→3d transitions.[141, 142, 201, 229, 230] When Si is in a tetrahedral coordination environment, mixing of the p- and d-states allows transitions to unoccupied states with some p-character, leading to a broad and intense feature (B) that follows the feature at lowest energy (A).[142, 201, 230, 231] (Feature (A) is noticeably split by spin-orbit coupling, leading to two peaks.[141, 142]) The Si $L_{2,3}$-edge lineshape is characteristic of the Si coordination geometry, in part because large changes in coordination lead to significant changes in the spectral lineshape and the intensity ratio of features A and B.[142, 230, 232]

Comparison of the spectra collected at the Si $L_{2,3}$-edge reveals only subtle changes in the lineshape (such as a slight broadening of the peaks with increasing metal content) and less than 0.1 eV change in absorption energy across all samples (**Figure 4.6b**). The lineshape is similar to SiO_2, and confirms that Si has a 4+ charge and remains in a 4-coordinate, tetrahedral geometry in the materials investigated here.[230] This is well supported by previous investigations of $(TiO_2)_x(SiO_2)_{1-x}$ using Si K-edge XANES, which have found that the Si CN is insensitive to changes in metal content of the glasses; Si^{4+} remains in a 4-coordinate tetrahedral site.[183] Si K-edge spectra of $(TiO_2)_x(SiO_2)_{1-x}$ collected here show no change in Si CN with increasing metal content, confirming studies by other groups (**Figure 4.7**).[183] There are no changes in the Si CN, removing the possibility that the decrease in the Si 2p BE is due to CN-induced shifts.

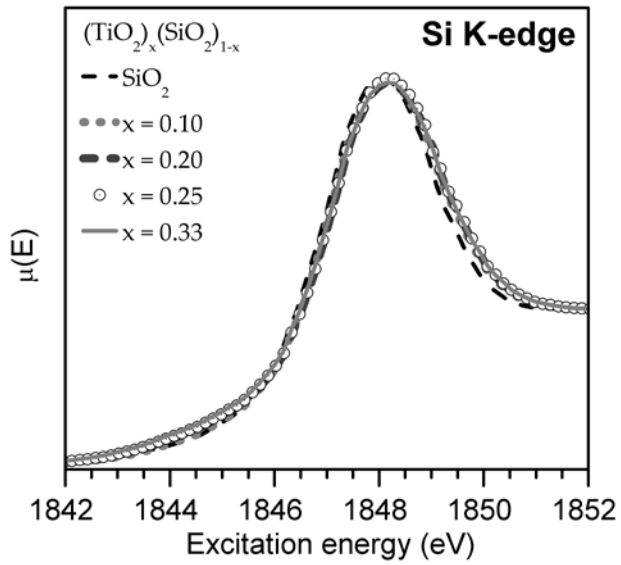

Figure 4.7. Si K-edge XANES spectra of ternary metal silicates show no changes with metal content, confirming there is no change in the Si CN with increasing metal content.

Further, the lack of significant changes in the Si $L_{2,3}$-edge absorption energies (<0.1 eV shift, determined by the maximum in the first derivative shown in **Figure 4.6b**) is testament to the lack of ground-state shifts in the Si 2p BEs with substitution. (Previous studies of related silicates have shown that Si $L_{2,3}$-edge absorption energies shift with substitution of the next-nearest neighbour (NNN) cation due to ground-state effects, but this is not observed in the metal silicates studied here.[230]

4.3.3.3. O K-edge XANES

The O K-edge XANES spectra were also collected to explore changes in the electronic structure of the silicates with changing Ti and Zr content. The peaks in O K-edge spectra result from O 1s→2p transitions, though because the O 2p orbitals interact with other atoms in the structure, the O K-edge spectra are feature-rich and often have contributions from the coordinating atoms. This inherent complexity makes electronic structure calculations a valuable aid for interpretation. Specifically, since XANES transitions are to unoccupied states, examining the unoccupied partial electronic density of states (DOS) can help assign general regions of spectral density to particular interactions. In general, the low-energy region of O K-edge spectra (<535 eV) from the silicates discussed here have features due to O 2p states interacting with M (n–1)d states (Ti 3d, Zr 4d).[152, 233, 234] This is followed by a region at higher energy (>535 eV) with features due to O 2p states interacting with np and ns states (*e.g.*, Ti 4p/4s, Zr 5p/5s, Si 3p/3s).[152, 233, 234] These assignments are supported by *ab initio* DOS calculations of the partial density of unoccupied states for $ZrSiO_4$ and $TiSiO_4$ (**Figure 4.8c**).

As with the Ti $L_{2,3}$- or Si $L_{2,3}$-edge, any shift in the O K-edge absorption energy would signal that there are changes in ground-state energies with substitution. The O K-edge spectra of the quaternary silicates show a lower-energy feature that becomes more prominent with

increasing Ti content (**Figure 4.8a**), owing to the greater number of unoccupied Ti 3d states (**Figure 4.8c**). The Ti 3d states are found at lower energies than the Zr 4d states due to the decreased average distance of 3d electrons to the nucleus (*i.e.*, 3d states are bound more tightly than 4d states). Examination of this feature shows no change in absorption energy (determined by the maximum in the first derivative shown in **Figure 4.8b**) when the metal content is varied. This is consistent with other findings in this work, which suggest that the total metal content (and not the metal identity, *e.g.*, Zr or Ti) plays the largest role in shifts of core-level energies. Similar examination of the higher-energy feature in the O K-edge spectra (~535.0 eV) reveals no shift in absorption energy (**Figure 4.8**), suggesting that the O ground-state energies are insensitive to changes in the identity of the metal. This was also found to be the case during examination of the Ti $L_{2,3}$- and Si $L_{2,3}$-edge spectra (Sections 4.3.3.1 and 4.3.3.2).

To examine the effect of total metal content over a larger range of substitution, the ternary silicates, $(ZrO_2)_x(SiO_2)_{1-x}$, were examined from $x = 0.1 \rightarrow 0.5$, with SiO_2 and ZrO_2 taken as the end-members at $x = 0$ and 1, respectively (**Figure 4.9**). No shift in the O K absorption energy (535.0 eV) was observed up to $x = 0.5$, and only a 0.2 eV increase was observed from $x = 0 \rightarrow 1$ (**Figure 4.9b**). Although there is a decrease (0.5 eV) in the onset energy of the Zr 4d states, the peak maximum of this feature in the O K-edge spectrum (the zero-crossing in the first derivative) remains unchanged, so it is likely due to a broadening of the Zr 4d band with increasing Zr content. The same phenomenon was seen in the O K-edge spectra of the Ti ternary silicates (Chapter 3), though there was no effect on the Ti core levels. Further, this change in the Zr valence states is not related to the changes in the O core levels (as seen by the lack of shift in the main edge at 535.0 eV), and is small compared to the 2.5 eV shift in the O 1s BE.

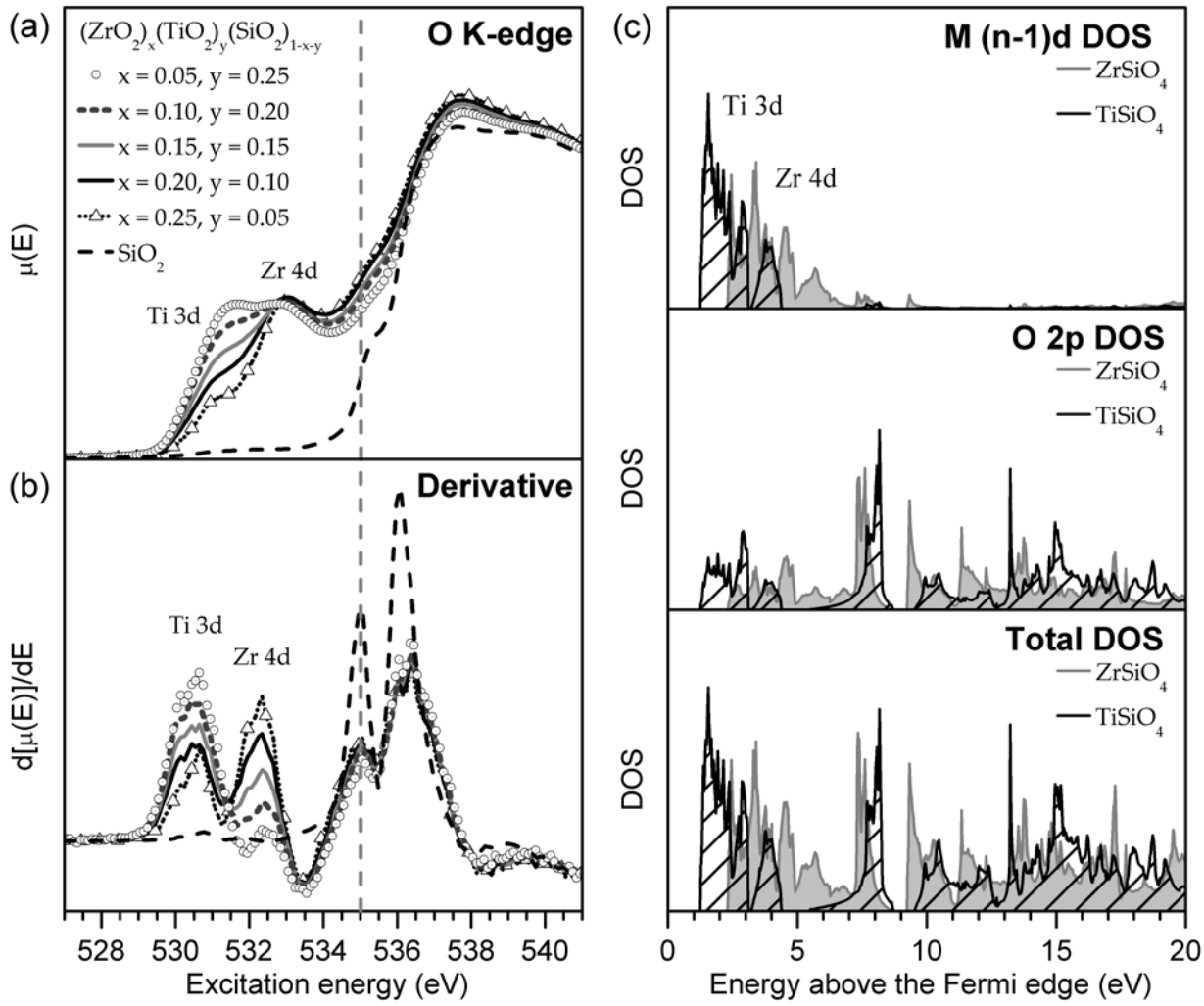

Figure 4.8. (a) O K-edge XANES spectra of the quaternary silicates. No shift was observed in the absorption energy (535.0 eV) when Zr replaces Ti, as monitored by (b) the first derivative of the O K-edge spectra. Dashed lines are a guide to indicate the absorption-edge energy, which is taken to be the peak maximum in the first derivative. (c) The metal (*n*–1)d, O 2p, and total density of states of $ZrSiO_4$ and $TiSiO_4$ were calculated to confirm assignment of the orbital contributions in the O K-edge spectra.

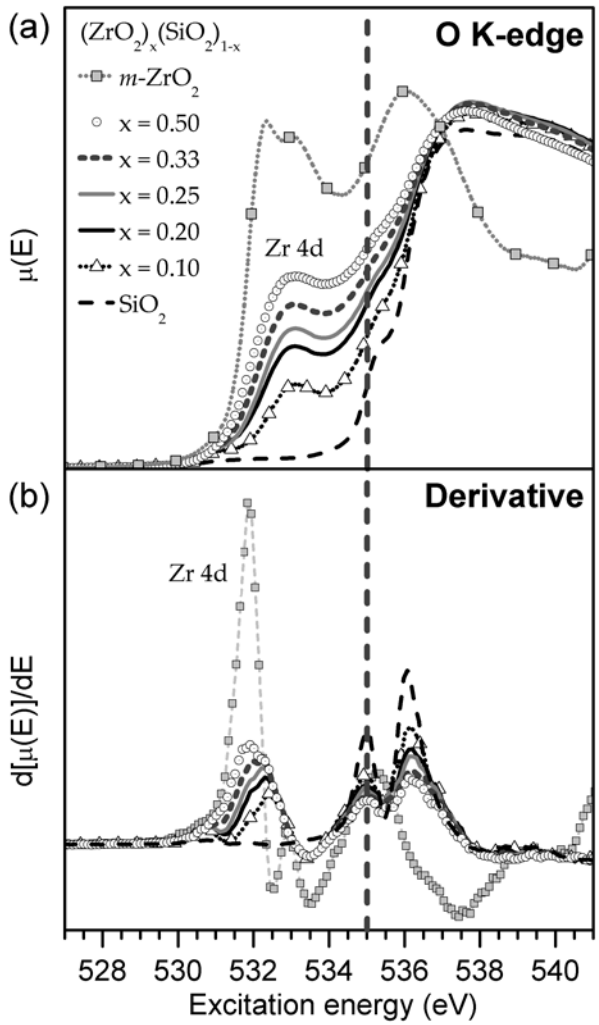

Figure 4.9. (a) O K-edge XANES spectra of the Zr ternary silicates. The absorption edge at 535 eV is preceded by a low-energy feature due to metal d states. (b) Taking the first derivative is helpful to look for shifts in absorption energy. Dashed lines are a guide to indicate the absorption-edge energy, which is taken to be the peak maximum in the first derivative. No shift in the O K absorption energy (535.0 eV) was observed up to (x + y) = 0.5, and a 0.2 eV increase was observed from x = 0→1 (from SiO_2→ZrO_2). Although there is a decrease (0.5 eV) in the onset energy of the Zr 4d states, the peak maximum of this feature in the O K-edge spectrum (the zero-crossing in the first derivative) remains unchanged, so it is likely due to a broadening of the Zr 4d band with increasing Zr content. Further, this change in the Zr valence states is not related to the changes in the O core levels (as seen by the lack of shift in the main edge at 535.0 eV), and is small compared to the 2.5 eV shift in the O 1s BE.

4.3.4. Identifying the cause of XPS BE shifts

Previous XPS studies on representative members of the $(ZrO_2)_x(SiO_2)_{1-x}$ series (*i.e.*, SiO_2, $ZrSiO_4$, ZrO_2) have also found decreases in core-line BEs with increasing metal content, but the shifts were attributed to increased ground-state charge density at the absorbing atom.[55] Core-line BEs and Auger transitions were collected, after which the Auger parameter was used to estimate ΔE_i^{EA} and DFT calculations were used to determine the contribution from $\Delta \sum_{i \neq j} \frac{q_j}{r_{ij}}$.[55] It was found that the calculated increase in the Madelung potential ($\Delta \sum_{i \neq j} \frac{q_j}{r_{ij}}$) was opposed by a measured increase in relaxation of similar magnitude, so it was concluded that the decrease in BEs with increasing metal content was due to increased charge density at the absorbing atom ($k\Delta q_i$).[55] However, XANES absorption energies are also sensitive to changes in charge density in the ground-state, and the spectra presented here show no change in absorption energies with metal content. This suggests that any ground-state contributions, although likely present, oppose each other and do not cause a net change in the ground-state core-level energies.

The XPS core-line spectra, reported in section 4.3.2, showed a large decrease in the photoelectron BEs of all elements in $(ZrO_2)_x(TiO_2)_y(SiO_2)_{1-x-y}$ with increasing total metal content. Meanwhile, soft X-ray XANES spectra (Ti $L_{2,3}$-, Si $L_{2,3}$- and O K-edge), reported in section 4.3.3, showed no changes in absorption energies, implying that ground-state effects are not a major contributor in the XPS BE shifts. This leaves changes in final-state relaxation (ΔE_i^{EA}) as the driving cause of these BE shifts. Previous studies on oxygen-deficient perovskite-type materials have shown that a change in CN can change the magnitude of relaxation (Chapter 2). This is not the case in the metal silicates studied here, as hard X-ray XANES (Zr and Ti K-edge) performed in this work show the metal CN is static as a function of total metal content in the

quaternary silicates (Section 4.3.1), so the decrease in BE cannot be driven by a changing CN of the absorbing atom. Yet, although the average CN of the absorbing atom (either Si, Zr, or Ti) does not change with increasing total metal content, the average CN of the Si/Zr/Ti *site* does increase as Si is replaced by metal atoms. (In the silicates examined here, the average CN of Si is 4, Ti is roughly 5, and Zr appears to be 8.) Given the large difference in the average Ti and Zr CNs, a difference between the ternary silicate BEs would be expected if an increase in the average CN of the nearest neighbour (NN) or next-nearest neighbour (NNN) site was a major contributor to the BE shifts. However, the core-line BE shifts from $(ZrO_2)_x(SiO_2)_{1-x}$ and $(TiO_2)_x(SiO_2)_{1-x}$ agree within the limits of instrumental precision (±0.1 eV) to those from $(ZrO_2)_x(TiO_2)_y(SiO_2)_{1-x-y}$ at similar metal loadings ($x = 0 \rightarrow 0.33$). The close agreement between the shifts in BE from the ternary and quaternary silicates, which have different average metal CNs, suggests that the average metal CN does not play a major role in the BE shifts observed in the quaternary silicates.

Instead, the BE shifts in the silicates are caused by substitution of Si by Ti or Zr atoms, which are much less electronegative ($\chi_{Si} = 1.74$, $\chi_{Ti} = 1.32$, $\chi_{Zr} = 1.22$).[114, 223] As the electronegativities of Ti and Zr are similar, mutual core-line BE shifts experienced by $(ZrO_2)_x(SiO_2)_{1-x}$ and $(TiO_2)_x(SiO_2)_{1-x}$ are remarkably close, as noted above. This close agreement between ternary BE shifts further supports the conclusion that the electronegativity difference ($\Delta\chi$) is the primary contributor. Despite large differences in the metal CN, bonding environment, and response of the glass network (large Zr atoms act primarily as network modifiers—network modifiers do not participate in forming the glass network structure—whereas smaller Ti atoms can act as network formers *and* modifiers), the driving force of the BE shifts is similar ($\Delta\chi$), and this leads to BE shifts of similar magnitudes in both ternary systems.[218, 219] As metal atoms

replace Si and the average electronegativity of the Si/Zr/Ti site decreases, the electron density becomes less tightly bound. Consequently, electron density from the chemical environment surrounding the absorbing atom can relax to a greater extent around the core-hole produced during an XPS experiment, lowering the final-state energy and leading to a decrease in the BE. Revisiting the charge potential model in eq. (4.1), these shifts resulting from final-state effects can be described as a change in the magnitude of the ΔE_i^{EA} term, which describes changes in extra-atomic relaxation.

4.3.5. The Auger parameter

The electronic structure of a material is sensitive to changes in the chemical environment, and can be probed by many spectroscopic techniques. As was discussed in Sections 4.3.2 and 4.3.4, there are numerous factors that influence the BE of a photoelectron peak, making complementary techniques necessary to elucidate the major contributors to a shift in energy. By comparing the shifts in XPS BEs and XANES absorption energies of transitions involving the same core electron, it is argued in this work that the observed decrease in BEs with increasing total metal content is due to greater final-state relaxation. To confirm that final-state effects are responsible for the BE shifts, the O KLL Auger transition was monitored and the Auger parameter, one of the few experimental measures of extra-atomic relaxation, was extracted (**Figure 4.10** and **Figure 4.11**).[77, 235]

4.3.5.1. The physical basis of the Auger parameter

The Auger parameter, α', is obtained by adding the BE of a core-line photoelectron peak and the kinetic energy (KE) of an Auger peak involving the same orbital as the photoelectron peak. Provided that the transitions giving rise to the Auger peak involve only core orbitals, the change in the Auger parameter provides a direct measure of final-state effects in XPS BEs.[56, 76,

[77, 235] These final-state effects are primarily due to changes in extra-atomic relaxation around the core-hole, ΔE_i^{EA} in eq. (4.1).[56, 77, 235] The physical basis for the Auger parameter lies in the nature of the final states created during photoelectron and Auger electron emission. In an Auger process, the atom is left in a doubly-ionized final state, which experiences more relaxation than the final state produced by emission of a photoelectron, where there is only a single core-hole.[235] Understandably, final-state effects play a larger role in Auger KEs than photoelectron BEs; however, shifts in ground-state energies influence XPS BEs and Auger KEs equally. Thus, when the Auger KE and XPS BE involving the same orbital are combined in the Auger parameter, ground-state effects drop out, and shifts in the Auger parameter depend only on final-state effects, as shown in detail below.[235]

After primary photoelectron emission in XPS, the excited atom is left with a core-hole. In the Auger KLL Auger process, this K-shell (1s) core-hole (K^+) subsequently decays with relaxation of an L-shell (2p) electron and ejection of an L-shell electron, leaving two holes in the L shell (L^+L^+). The kinetic energy (KE) of the Auger electron is given approximately by eq. (4.2), where E_i terms represent ground-state energies of core shells, and E_i^{EA} terms represent the relaxation energies of core shells. (Where appropriate, initial-state effects have been placed in square brackets to help distinguish them from final-state effects.)

$$\mathrm{KE}_{\mathrm{Auger}} = [E_i(\mathrm{K}) - E_i(\mathrm{L}) - E_i(\mathrm{L})] - E_i^{\mathrm{EA}}(\mathrm{K}^+) + E_i^{\mathrm{EA}}(\mathrm{L}^+\mathrm{L}^+) \qquad (4.2)$$

Because the KLL Auger KE depends on the difference in energy between the K and L shells, the Auger KE will increase if the K-shell becomes more stabilized (lower energy), while the Auger KE will decrease if the L-shell becomes more stabilized. (This is why E_i(L) terms have the opposite sign as E_i(K) terms.) Accordingly, a shift in the kinetic energy of the KLL

Auger electron is given by eq. (4.3). By analogy, a shift in the KE of a 1s (K-shell) photoelectron examined by XPS is given by eq. (4.4).

$$\Delta\mathrm{KE}_{\mathrm{Auger}} = [\Delta E_i(\mathrm{K}) - 2\Delta E_i(\mathrm{L})] - \Delta E_i^{\mathrm{EA}}(\mathrm{K}^+) + \Delta E_i^{\mathrm{EA}}(\mathrm{L}^+\mathrm{L}^+) \quad (4.3)$$

$$\Delta\mathrm{KE}_{\mathrm{XPS}} = [-\Delta E_i(\mathrm{K})] + \Delta E_i^{\mathrm{EA}}(\mathrm{K}^+) \quad (4.4)$$

Provided that only core shells are involved in Auger emission, the shift in ground-state energy of the different core shells is approximately equal (*i.e.*, $\Delta E_i(\mathrm{K}) = \Delta E_i(\mathrm{L}) = \Delta E_{i,\mathrm{ground}}$) and the shift in the Auger KE simplifies to eq. (4.5).[235] If valence shells are involved, the simple model shown here breaks down because the shift in ground-state energies of core shells is different than valence shells.

$$\Delta\mathrm{KE}_{\mathrm{Auger}} = \left[-\Delta E_{i,\mathrm{ground}}\right] - \Delta E_i^{\mathrm{EA}}(\mathrm{K}^+) + \Delta E_i^{\mathrm{EA}}(\mathrm{L}^+\mathrm{L}^+) \quad (4.5)$$

In the original model of the Auger parameter proposed by Wagner, final-state relaxation (referred to as the "polarization energy") was assumed to be proportional to e^2, where e is the charge of the ion.[235] Consequently, the shift in relaxation energy of the doubly-ionized state Auger final state will be 4 times that of the singly-ionized XPS final state, *i.e.*, $\Delta E_i^{\mathrm{EA}}(\mathrm{L}^+\mathrm{L}^+) = 4\Delta E_i^{\mathrm{EA}}(\mathrm{K}^+)$. This is shown in eq. (4.6), which simplifies to eq. (4.7).

$$\Delta\mathrm{KE}_{\mathrm{Auger}} = \left[-\Delta E_{i,\mathrm{ground}}\right] - \Delta E_i^{\mathrm{EA}}(\mathrm{K}^+) + 4\Delta E_i^{\mathrm{EA}}(\mathrm{K}^+) \quad (4.6)$$

$$\Delta\mathrm{KE}_{\mathrm{Auger}} = \left[-\Delta E_{i,\mathrm{ground}}\right] + 3\Delta E_i^{\mathrm{EA}}(\mathrm{K}^+) \quad (4.7)$$

Taking the difference between the shift in the Auger KE and photoelectron KE (eq. (4.8)) removes any dependence on ground-state effects; the shift in the Auger parameter, $\Delta\alpha$, directly provides the contribution of final-state relaxation in a singly-ionized final state, such as that created in XPS.

$$\Delta\alpha = \Delta\mathrm{KE}_{\mathrm{Auger}} - \Delta\mathrm{KE}_{\mathrm{XPS}} = 2\Delta E_i^{\mathrm{EA}}(\mathrm{K}^+) \quad (4.8)$$

Alternatively, the excitation energy can be added to the Auger parameter, and the result is equivalent to addition of the Auger KE and XPS BE, shown in eq. (4.9) and eq. (4.10).

$$\Delta\mathrm{KE}_{\mathrm{XPS}} = \mathrm{h}\upsilon - \Delta\mathrm{BE}_{\mathrm{XPS}} \quad (4.9)$$

$$\Delta\alpha' = \Delta\alpha + \mathrm{h}\upsilon = \Delta\mathrm{KE}_{\mathrm{Auger}} + \Delta\mathrm{BE}_{\mathrm{XPS}} = 2\Delta E_i^{\mathrm{EA}}(\mathrm{K}^+) \quad (4.10)$$

4.3.5.2. The effect of total metal content on final-state relaxation

The Auger parameter described and used here only provides a reliable estimate of final-state relaxation when the valence shell is not involved in the Auger transition.[77, 235-238] However, though strict quantification of the relaxation requires modified Auger parameters or Auger transitions involving only core orbitals, the use of Auger transitions involving valence orbitals is used here in the simple model to qualitatively confirm that final-state effects are responsible for the observed BE shifts.[77, 238-241] O KLL Auger spectra for the quaternary and ternary silicates are shown in **Figure 4.10**, and the peak maxima were plotted as a function of total metal content (**Figure 4.11a**). These Auger KE values were added to the previously presented O 1s BEs (**Figure 4.5**) to obtain the Auger parameter (**Figure 4.11b**). A plot of the Auger parameter vs. total metal content (irrespective of metal identity) yields a positive linear relationship, confirming that ΔE_i^{EA}, the degree of final-state relaxation, in $(ZrO_2)_x(TiO_2)_y(SiO_2)_{1-x-y}$ and $(ZrO_2)_x(SiO_2)_{1-x}$ increases with total metal content. As the electronegativities of Zr and Ti are similar, the identity of the metal was not found to be important in this case.

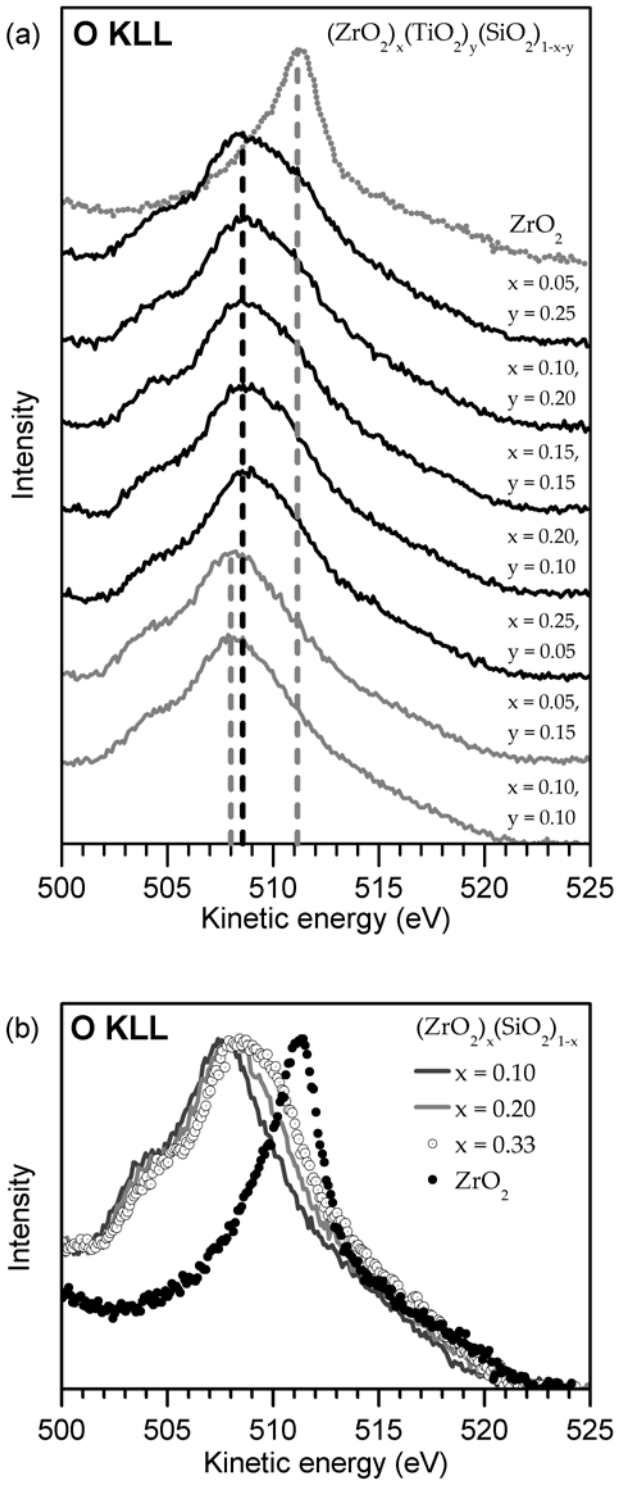

Figure 4.10. O KLL Auger spectra from (a) quaternary and (b) ternary silicates.

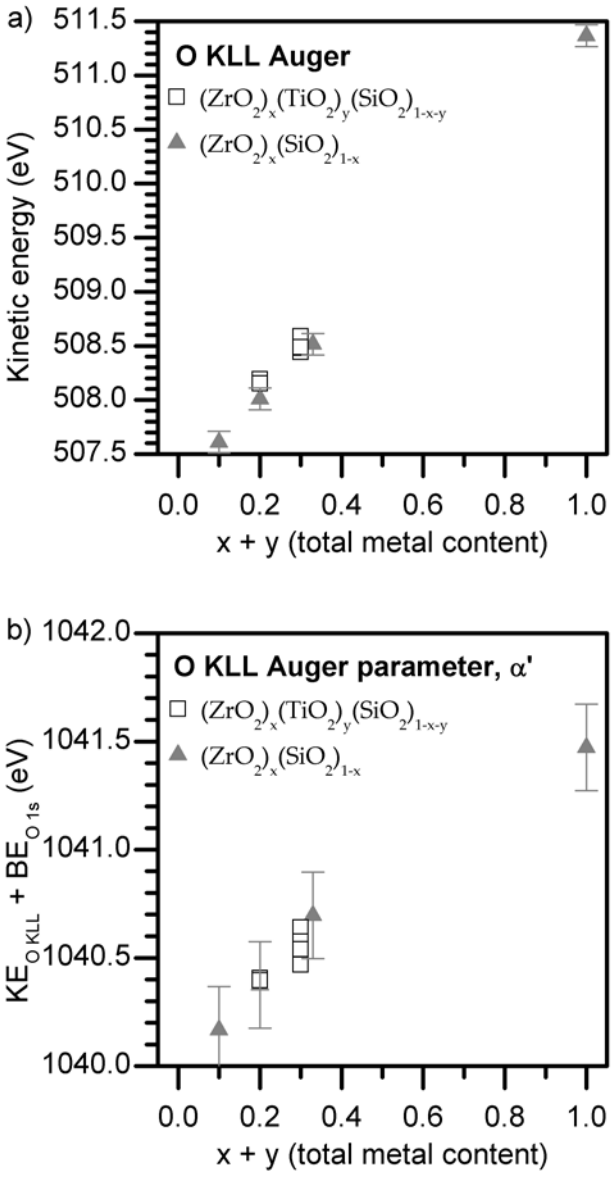

Figure 4.11. (a) O KLL Auger peak maxima and (b) Auger parameters of the quaternary and ternary silicates. The Auger parameter increases with total metal content, confirming that final-state relaxation increases in the same fashion.

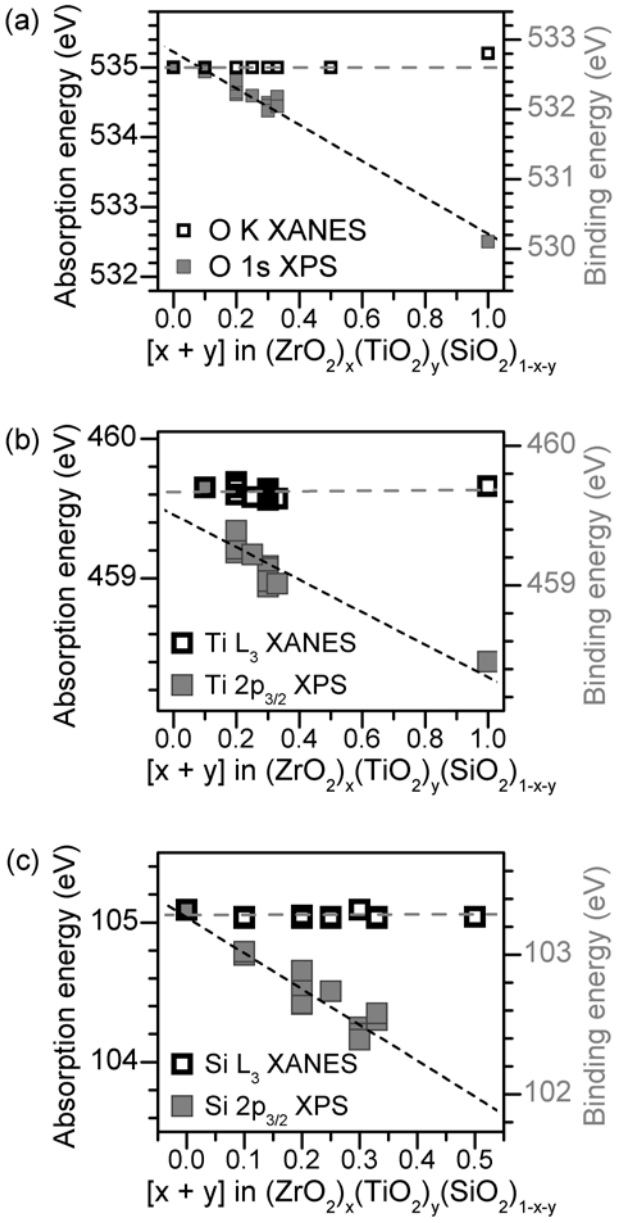

Figure 4.12. Plots of XANES absorption energies and XPS BEs for transitions with identical ground-state energies. The absorption energies remain unchanged, while the BEs decrease, indicating that final-state effects are dominant. The height of the symbols represents the precision of the measured energy (±0.1 eV), and the precision of the stoichiometry is believed to be better than (x,y ±0.02). Spectral energies from ternary silicates [$(TiO_2)_x(SiO_2)_{1-x}$ and $(ZrO_2)_x(SiO_2)_{1-x}$; x = 0.1, 0.25, 0.33, 0.50] are included to show the close agreement with the quaternary silicates.

4.4. Conclusions

The observation of significant shifts in the XPS BEs of the quaternary transition-metal silicates without accompanying shifts in analogous XANES spectral energies demonstrates the dominant influence of increasing final-state relaxation with next-nearest neighbour (NNN) substitution in the silicates (**Figure 4.12**). Zr K-edge, Ti K-edge, Ti $L_{2,3}$-edge, Si $L_{2,3}$-edge, and Si K-edge XANES spectra confirm that the CN and oxidation state of Zr^{4+}, Ti^{4+}, and Si^{4+} do not change with increasing metal content. In the $(ZrO_2)_x(TiO_2)_y(SiO_2)_{1-x-y}$ series, the substitution of Si for group IV metals (Zr and Ti) with lower electronegativity increases the amount of final-state relaxation experienced by atoms in the material upon excitation, decreasing all core-line BEs. Si is more electronegative than Ti or Zr, and restricts the ability of electrons in the material to relax around a core-hole produced in XPS. As the concentration of the incorporated less-electronegative atoms increases, electrons in the material near a core-hole are able to relax to a greater extent, lowering the final-state energy and the observed BE. The increase in final-state relaxation with total metal content has been supported through analysis of the Auger parameter, which also increases with total metal content. This investigation provides another example to improve our understanding of the many influences that makes analysis of XPS spectra complicated, and highlights that large changes in BE can occur without any changes in ground-state energies (*e.g.*, oxidation state).

Chapter 5

5. Conclusions

5.1. Summary

The work presented here highlights the investigation of several systems toward the goal of better understanding the factors that cause X-ray photoelectron spectroscopy (XPS) binding energies (BE) to shift. This spectroscopic technique is routinely used to examine the electronic structure of materials in the solid state, yet many effects remain poorly understood and require further study to understand their role in spectral energy shifts. Improving our understanding of the causes of spectral energy shifts, such as the effect of coordination number (CN) and the next-nearest neighbour (NNN), is critical to the continuing development of this technique as a probe of electronic structure. Through selection of model systems that isolate many of the contributors to spectral energy shifts, the combined use of X-ray absorption near-edge spectroscopy (XANES) and XPS has been shown to be useful for resolving ground- and final-state effects. This thesis describes the first systematic study of the role that CN plays in BE shifts, and includes an important study of final-state NNN effects, which have not been extensively studied in inorganic solids.[54, 73, 193]

5.1.1. The effect of coordination number

The role of CN in XPS BE shifts was investigated in Chapter 2, which featured the $SrFe_{1-x}Zn_xO_{3-\delta}$ ($0 \leq x \leq 1$) system. This is an oxygen-deficient perovskite-type material that is interesting because of its mixed ionic-electronic conduction (MIEC), which positions it for use in

high-temperature reactors catalyzing the partial oxidation of methane to syngas, and as a part of solid oxide fuel cells (SOFC).[9] Co-containing materials decompose under the high-temperature operating conditions for these proposed applications, so the absence of Co in the materials studied here makes $SrFe_{1-x}Zn_xO_{3-\delta}$ an important system to study.[9, 115] With increasing Zn content in $SrFe_{1-x}Zn_xO_{3-\delta}$ ($0 \leq x \leq 1$), examination of Fe K- and Zn K-edge XANES spectra showed that greater oxygen deficiency lowers the transition-metal CN. Substitution of Fe by Zn resulted in shifts in the metal 2p XPS BEs that were much greater than the shifts observed in the corresponding $L_{2,3}$-edge XANES absorption energies. These shifts are due to increasing final-state relaxation with decreasing metal CN. As the number of electron-rich O^{2-} anions surrounding the metal centres decreases, there is less electron density to screen the core-hole generated by XANES or XPS processes. Consequently, the poorly-screened core-hole exerts a stronger influence on the system, resulting in greater relaxation of the electrons. Further, as O is electronegative compared to other atoms in the structure, its tendency to tightly bind electrons restricts the ability of electrons from the material to relax around a core-hole on a metal centre. As the CN decreases, the magnitude of final-state relaxation around the core-hole increases, lowering the final-state energy and the observed BE. As mentioned throughout this thesis, if the same core orbital is probed by XANES and XPS, final-state effects are more pronounced in XPS because the photoelectron is no longer associated with the material in the final-state and is thus unable to screen the core-hole.[78, 116] (By comparison, XANES transitions are to bound states, and the promoted electron is still associated with the material in the final-state and is able to partially screen the core-hole.) This is consistent with estimations of screening through application of Slater's rules, which were applied to explain the minimal influence of final-state effects in Fe and Zn L_3-edge XANES, and stronger influence in the Fe and Zn 2p XPS spectra.[160] Unlike the

metal spectra, energy shifts in the O K-edge XANES spectra and analogous O 1s XPS spectra were similar in magnitude, as ground-state effects were found to dominate. This was attributed to increased nearest-neighbour screening of the O nuclear charge with greater Zn content.

5.1.2. Structural studies of transition metal silicates

The amorphous TM silicates featured in Chapter 3 and 4, $(MO_2)_x(M'O_2)_y(SiO_2)_{1-x-y}$ (M, M' = Ti, Zr, Hf), are a family of materials whose many properties can be chosen in a controlled manner by adjusting the amount of metal oxide added. A variant of $(HfO_2)_x(SiO_2)_{1-x}$ is being used as a high-κ dielectric replacement for SiO_2 in complementary metal-oxide–semiconductor (CMOS) devices, such as microprocessors, making the study of these materials important for the electronics industry.[35, 40, 44] Within this large family, the Ti and Zr ternary systems, $(TiO_2)_x(SiO_2)_{1-x}$ $(0 \leq x \leq 0.33)$ and $(ZrO_2)_x(SiO_2)_{1-x}$ $(0 \leq x \leq 0.50)$, and the Ti/Zr quaternary system, $(MO_2)_x(M'O_2)_y(SiO_2)_{1-x-y}$ $(x + y = 0.2, 0.3)$, were synthesized by sol-gel methods and investigated by XANES and XPS. The lack of long-range order in amorphous materials hinders the use of diffraction-based techniques that are typically used to probe structure and homogeneity, making them ideal candidates for study by X-ray spectroscopy. The increased understanding of the how the CN changes depending on composition and location of the metal centres within the material, along with why the XPS BEs and XANES absorption energies shift with composition provided here, will aid in optimizing these materials for industrial applications. Additionally, despite the considerable volume of work on the ternary silicates (see Chapter 3, Chapter 4, and references therein), the quaternary silicates have received significantly less attention, and the work presented in Chapter 4 is one of the few structural studies of this system.[168]

Chapter 3 investigated how the Ti CN changes in $(TiO_2)_x(SiO_2)_{1-x}$ depending on composition and annealing temperature, and if the Ti atoms examined are located within the bulk of the material or at the surface. It was shown therein that the use of both hard (Ti K-edge) and soft (Ti $L_{2,3}$-edge) X-rays provides a useful way to monitor changes in the bulk and surface, respectively, of these amorphous materials. Examination of Ti K- and $L_{2,3}$-edge XANES spectra revealed that the average Ti CN increases with greater Ti content (x), an effect of the larger ionic radius of Ti. Comparison of the Ti K- and Ti $L_{2,3}$-edge XANES spectra showed, for the first time, that the average Ti CN is higher at the surface compared to within the bulk. (Within the bulk of the material, 4-, 5- and 6-coordinate Ti was observed while only 5- and 6-coordinate Ti was present at the surface.) Comparison of Ti K- and $L_{2,3}$-edge spectra of annealed samples revealed that Ti atoms at the surface have a higher average CN than in the bulk, likely due to the presence of surface hydroxide and water groups that can coordinate to the Ti centres. Also, these materials are known to exhibit heterogeneity at higher metal content, though the presence of metal-rich amorphous domains in the silica network is difficult to detect, even with a combination of advanced spectroscopic techniques.[47, 185, 219] It was found here that O 1s core-line XPS spectra of these materials, presented in Chapters 3 and 4 (**Figure 3.2a** and **Figure 4.4b**), exhibit features corresponding to metal-rich domains that increase with metal content. Owing to the strong O 1s signal, this provides a simple and rapid test to inspect the homogeneity of these materials during XPS analysis. The ability to easily detect heterogeneity may be valuable in other studies because XPS is commonly used for analyzing these materials, particularly in thin film applications.

5.1.3. Next-nearest neighbour (NNN) effects and electronegativity

In addition to the important structural information acquired from the studies described above, final-state effects were investigated by examining changes in spectral energy with composition. The lack of significant changes in oxidation state or changes in electronegativity ($\chi_{Zn} = 1.66$, $\chi_{Fe} = 1.64$) in the $SrFe_{1-x}Zn_xO_{3-\delta}$ system removed influences from ground-state effects or NNN influences on the metal core-line BEs.[114] However, NNN effects have not been extensively studied in inorganic solids and are thus poorly understood. For this reason, the role of the NNN atom was investigated in Chapters 3 and 4 by controlling the stoichiometry, and thus the degree of substitution at the NNN site. With increasing Ti content in $(TiO_2)_x(SiO_2)_{1-x}$, the O 1s, Si 2p, and Ti 2p XPS BEs decreased significantly, in agreement with previous studies. In comparison, the corresponding XANES absorption energies involving the same excited core-electron showed little to no shift.[178, 191] Ground state effects equally affect both XPS and XANES, so a comparison of the XPS BE and XANES absorption energy shifts allowed for an estimation of the contribution of final-state relaxation to the XPS BEs. The decrease in O 1s, Si 2p, and Ti 2p BEs with increasing Ti content is due to substitution of Si by less electronegative Ti atoms, leading to greater final-state relaxation. As the Ti CN was found to increase with greater Ti content, the shift to lower, rather than higher, BEs shows that changes in final-state relaxation due to substitution of the NNN atoms will dominate over CN effects when the difference in electronegativity of the substituting atoms is sufficiently large (*e.g.*, $\Delta\chi_{(Si-Ti)} = 0.4$).[114] While $(TiO_2)_x(SiO_2)_{1-x}$ was found to exhibit these NNN final-state effects when Si replaces Ti ($\Delta\chi$ is large, $\Delta\chi_{(Si-Ti)} = 0.4$), this type of effect was not observed in $SrFe_{1-x}Zn_xO_{3-\delta}$ upon replacement of Fe by Zn ($\Delta\chi$ is small, $\Delta\chi_{(Fe-Zn)} = -0.02$), evidence that the difference in electronegativity plays a crucial role.

Chapter 4 expanded upon the findings in the ternary silicates by increasing the complexity of the system to examine the effects of metal identity and changes in average CN of a crystallographic site (as opposed to an element). Zr K-, Ti K-, and Ti $L_{2,3}$-edge spectra showed less change in the CN of metal centres than in the ternary silicates, allowing the isolation of CN-induced shifts in XPS BEs that were shown to influence final-state relaxation in Chapter 2. As was the case with the ternary silicates, the significant shifts in the XPS BEs of the quaternary transition-metal silicates without accompanying shifts in analogous XANES spectral energies demonstrates the dominant influence of increasing final-state relaxation with NNN substitution in the silicates. In the $(ZrO_2)_x(TiO_2)_y(SiO_2)_{1-x-y}$ series, the substitution of Si for group IV metals (Zr and Ti) with lower electronegativity increases the degree of final-state relaxation in the material upon generation of a core-hole, decreasing all core-line BEs. The increase in final-state relaxation with total metal content has been confirmed empirically through analysis of the Auger parameter, one of the few experimental measures of relaxation, which also increases with total metal content.[77, 235] Despite large shifts in BE due to NNN substitution, no significant effect was observed due to the average CN of the NNN *site* in these materials. (In the silicates examined here, the average CN of Si is 4, Ti is roughly 5, and Zr is >6.) Mutual core-line BE shifts of $(ZrO_2)_x(SiO_2)_{1-x}$ and $(TiO_2)_x(SiO_2)_{1-x}$ agree within the limits of instrumental precision, ±0.1 eV, and show similar trends at the metal loadings investigated (x = 0→0.33). The close agreement between BEs of ternary metal silicates with different average metal CNs suggests that the average CN of the metal site (in these silicates) does not play a major role in the observed BE shifts. This is consistent with what has been previously described in this thesis. That is, since $\Delta\chi$ is large, we expect NNN effects to dominate over CN-induced effects. Also, because $\Delta\chi$ is responsible for the BE shifts and because Zr and Ti have similar electronegativities (χ_{Ti} = 1.32,

χ_{Zr} = 1.22; $\Delta\chi_{(Si\text{-}Ti)}$ = 0.4, $\Delta\chi_{(Si\text{-}Zr)}$ = 0.5), similar shifts in BE result, regardless of metal identity (Zr or Ti).[114, 223]

The nature of the decrease in BEs with increasing metal content in the silicates has been debated, as there are many potential effects that could cause this shift. Some studies have suggested the BE shift is caused by final-state, while more recent studies combining experiment and theory argued that ground-state effects are responsible for the decrease in BE.[54, 55] The findings presented in Chapter 3 and Chapter 4 suggest that the decrease in BEs with increasing metal content is due to increasing final-state relaxation, which is not new.[54] However, most previous studies were conducted on thin films due to the industrial applications (semiconductor devices and optical coatings), where it was mentioned that interfacial charge trapping could have led to the observed decrease in BE.[54] Charge trapping occurs between thin layers with different dielectric constants, but is not an issue with powders, which were chosen for the studies presented in this thesis.[54] Properly assigning the origin of BE shifts is important, as ground-state electronic structure often dictates material properties and stability.

5.1.4. Significance and implications

Taken together, these studies on final-state effects provide important examples to improve our understanding of two of the many influences in XPS BE shifts that often complicate analysis. The significant changes in BE due to increasing final-state relaxation, such as those observed in this thesis, do not necessarily reflect changes in the ground-state energies or electron density, which are often sought by the use of XPS. For example, shifts in XPS core-line BEs are routinely used to assign changes in oxidation state, where an increase in formal charge by +1 (*e.g.*, $Fe^{2+} \rightarrow Fe^{3+}$; $V^{4+} \rightarrow V^{5+}$) leads to an increase in BE of roughly 1-2 eV.[242-244] This is similar in magnitude to the shifts in BE presented throughout this thesis, where large changes in BE due to

increasing final-state relaxation occurred without any changes in oxidation state. Shifts in XPS core-line BEs are also used in catalyst optimization studies, where small (<0.5 eV) shifts in XPS BEs have been used to determine the relative electron density of metal centres.[81, 245, 246] The electron density of metal centres in metal-phosphide hydrodesulphurization (HDS) catalysts affects the adsorption (and desorption) of sulphur on the surface of the catalyst, which has a strong influence on catalytic activity.[245-247] (High affinity for sulphur leads to stronger adsorption, which increases catalytic activity up to a point; in the extreme case at low affinity, no substrate adsorbs to the surface and thus there is no reaction, while at the extreme case of high affinity, no product desorbs from the surface and the catalyst is deactivated.) Catalytic activity is often tuned by partial substitution of the metal. However, Chapter 3 and 4 demonstrated that if the difference in electronegativity ($\Delta\chi$) of the substituted elements is large, substitution can lead to shifts in BE due to increasing final-state relaxation that, by virtue of being final-state effects, do not necessarily reflect changes in the ground-state electron density. These shifts in BE are larger in magnitude (>0.5 eV) than the BE shifts observed in the catalyst optimization studies mentioned earlier, making further studies of NNN effects a valuable endeavour, as it is currently unknown at which point $\Delta\chi$ leads to significant final-state effects.

5.2. Directions for future research

Although the observation of significant BE shifts due to final-state effects is well-substantiated within the systems studied in this thesis, systematic studies on other systems are required to evaluate the transferability and generality of the concepts and models discussed in this thesis. $ABO_{3-\delta}$ perovskite-type materials are a likely avenue for extending the current studies, as the perovskite structure-type is notoriously robust to substitution.[15] By controlled substitution of the A and B sites, it should be possible to create several series and examine the

effect of changing electronegativity and/or CN on XPS BEs, providing more well-controlled systems to study. As there have only been 2 broad systems examined in this thesis, it is important to confirm that the results are general.

A good starting point would be closely related systems to the ones studied in this thesis. In the $Sr(M_{1-x}M'_x)O_{3-\delta}$ (*M, M'* = transition metal) system, $SrFeO_{2.75}$ ($\delta = 0.25$) is convenient because it has a defined stoichiometry and is oxygen deficient. This allows the TM CN to increase or decrease, depending on the substituent. Substitution by Zn^{2+} was chosen for study in Chapter 2 because of its fixed oxidation state and similar electronegativity to Fe. In this case, the TM CN decreases to maintain charge neutrality. However, substitution by Zr^{4+} should increase the TM CN for the same reason. The $SrFe_{1-x}Zr_xO_{3-\delta}$ system was synthesized and XANES measurements have been performed.[112] Performing XPS measurements is the next logical step, where an increase in the TM BEs is expected with increasing Zr^{4+} content due to an increase in the average CN (assuming the average oxidation state of Fe remains unchanged). As the change in δ is smaller ($0.25 \rightarrow 0$ in the Fe/Zr system, *cf.* $0.25 \rightarrow 1$ in the Fe/Zn system), the changes in CN, and therefore BE, are expected to be smaller.

Any fundamental study requires pure, single-phase materials, and both the $SrFe_{1-x}Zn_xO_{3-\delta}$ and $SrFe_{1-x}Zr_xO_{3-\delta}$ system exhibit multiple phases at intermediate values of x ($0.3 < x < 1$) when using high-temperature synthetic methods. This limits the change in CN that can be achieved and studied for some elements (*e.g.*, for Fe in these materials). Low-temperature methods designed to intimately mix the starting materials, such as routes employing ethylenediaminetetraacetic acid (EDTA) and citrate complexation, could potentially allow for synthesis of materials that are not accessible through the direct reaction of binary oxides at high temperature.[24, 248-250] Compared to traditional syntheses, these "soft" complexation methods are less limited by diffusion because of

the proximity and thorough mixing of precursors. As a result, lower processing temperatures can be used, where undesirable phases might not be thermodynamically favoured.

There are also limits to the change in CN that may not be as easily overcome in $SrFe_{1-x}Zn_xO_{3-\delta,}$ making other model systems necessary. In this perovskite-type system, metal CNs can range from 4 to 6, but it would be valuable to examine changes in systems with higher metal CNs. Further, it would be beneficial to study systems where the change in CN could be quantified. A study of the ZrO_2 system is an excellent opportunity for both of these studies. ZrO_2 has several polymorphs where the Zr CN is 7- or 8-coordinate.[251-253] Chapter 4 showed that the similar electronegativities of Zr and Ti do not cause shifts in BE due to NNN effects. Thus, $ZrTiO_4$ (the Zr CN is 6) should serve as a suitable standard for 6-coordinate Zr, as it has the same metal/oxygen mol ratio (*i.e.*, MO_2) as ZrO_2.[254-256] Monitoring the change in BE as the absolute Zr CN decreases quantitatively from 8 to 6 will validate the results found in this work and extend the model to higher-coordinate metal centres.

The study described in Chapter 2 and the studies proposed here all involve coordination environments where a metal centre is surrounded by O atoms. It is believed that the electronegativity of O is an important factor in these CN-induced final-state effects. As O atoms are much more electronegative than the other elements in the systems examined, they are believed to hinder the relaxation of electrons in the material around a core-hole generated on the metal atom. When the metal CN is high, electronegative O atoms restrict the ability of electron to relax, and this is alleviated when the CN decreases. However, on a more general level, is the observed CN-induced (or NNN-induced) change in final-state relaxation merely due to an increase in the average electronegativity of atoms in the material? As the *average* electronegativity (a measure of the ability to attract electrons) of atoms decreases in the materials

studied (as O is removed in $SrZn_xFe_{1-x}O_{3-\delta}$ or as Si is replaced in the metal silicates), electrons in the material are less tightly held to atoms and able to better relax around a core-hole on nearest-neighbour or NNN atoms, causing BEs to decrease. This raises an important question. A*t what point does the difference in electronegativity of substituted elements begin to play a major role in BE shifts?* To answer this, it would be wise to undertake a systematic study of BE shifts across a series of metal silicates with increasing atomic number at constant total metal content ($(M_uO_v)_x(SiO_2)_{1-x}$; *M* = Mg, Ca, Y, Nb, W, V, Mn, Fe, Co, Al, B; x = constant; *u* and *v* depend on the charge of *M*), isolating the effect of the NNN electronegativity (χ). Chapters 3 and 4 showed that the difference in electronegativity between Si and the incorporated metal drives the shift in BE, and the study described here may be able to better quantify this effect. The silica network is robust and able to accommodate a wide range of substituents, and the metal-organic precursors for sol-gel syntheses are commercially available for most transition metals, as well as many other elements.[51, 206] By studying the change in the Si 2p BEs as the identity of the metal is changed in the silica network, a relationship of BE shift vs χ_{NNN} (the electronegativity of the next-nearest neighbour) may emerge.[73, 193]

There are many systems to be studied, but an excellent starting point is the $(M_2O_3)_x(SiO_2)_{1-x}$ system where *M* = Al and B, which could be made by sol-gel reaction of $Si(OEt)_4$, $Al(OBu)_3$, and $B(OBu)_3$. Varying the concentration of both substituents in the quaternary $(M_2O_3)_x(M'_2O_3)_y(SiO_2)_{1-x-y}$ system (*M* = Al; *M'* = B), as was done in Chapter 4, would be a smart choice. First, the structures of aluminosilicate and borosilicate glasses are well studied, facilitating synthesis and structural characterization.[33, 257-268] Second, Al and B are isovalent, simplifying characterization by XPS, where charge plays a large role.[56] Third, the

range of electronegativities in the substituted species is large (χ_{Si} = 1.74, χ_{Al} = 1.47, χ_{B} = 2.01), which will cause large changes in XPS BEs and make any trends more evident.[114]

This thesis has investigated several inorganic solids and has outlined shifts in XPS BEs that result from changes in CN and NNN atoms, representing an important step towards a more complete understanding of why BEs change. Several model systems have been identified for future studies due to the suspected ability to isolate many of the competing factors that influence XPS BEs (*e.g.*, changes in structure, oxidation state, concentration, coordination number, etc.). These further studies will allow for a refinement of the understanding that was developed in this work.

6. References

1. H. Kuzmany, *Solid-state spectroscopy: an introduction*, Springer, Heidelberg, Germany, 2009.

2. J. C. Vickerman and I. S. Gilmore, eds., *Surface analysis: the principal techniques*, Wiley, Chichester, U.K., 2009.

3. D. W. Bruce, D. O'Hare and R. I. Walton, eds., *Functional oxides*, Wiley, Chichester, U.K., 2010.

4. S. Ramanathan, ed., *Thin film metal-oxides: fundamentals and applications in electronics and energy*, Springer, New York, 2010.

5. J. G. Bednorz and K. A. Muller, *Zeitschrift fur Physik B: Condensed Matter*, 1986, **64**, 189-193.

6. Y. Kamihara, H. Hiramatsu, M. Hirano, R. Kawamura, H. Yanagi, T. Kamiya and H. Hosono, *Journal of the American Chemical Society*, 2006, **128**, 10012-10013.

7. M. Imada, A. Fujimori and Y. Tokura, *Reviews of Modern Physics*, 1998, **70**, 1039-1263.

8. J. H. Park, E. Vescovo, H. J. Kim, C. Kwon, R. Ramesh and T. Venkatesan, *Nature*, 1998, **392**, 794-796.

9. H. J. M. Bouwmeester, *Catalysis Today*, 2003, **82**, 141-150.

10. G. A. Prinz, *Science*, 1998, **282**, 1660-1663.

11. S. Jin, T. H. Tiefel, M. McCormack, R. A. Fastnacht, R. Ramesh and L. H. Chen, *Science*, 1994, **264**, 413-415.

12. N. A. Spaldin and M. Fiebig, *Science*, 2005, **309**, 391-392.

13. W. Eerenstein, N. D. Mathur and J. F. Scott, *Nature*, 2006, **442**, 759-765.

14. A. M. Glazer, *Acta Crystallographica Section B: Structural Science*, 1972, **28**, 3384-3392.

15. A. S. Bhalla, R. Y. Guo and R. Roy, *Materials Research Innovations*, 2000, **4**, 3-26.

16. P. M. Woodward, *Acta Crystallographica Section B: Structural Science*, 1997, **53**, 32-43.

17. A. M. Glazer, *Acta Crystallographica Section A*, 1975, **31**, 756-762.

18. P. M. Woodward, *Acta Crystallographica Section B: Structural Science*, 1997, **53**, 44-66.

19. P. S. Halasyamani and K. R. Poeppelmeier, *Chemistry of Materials*, 1998, **10**, 2753-2769.

20. M. Kunz and I. D. Brown, *Journal of Solid State Chemistry*, 1995, **115**, 395-406.

21. I. M. Reaney, *Journal of Electroceramics*, 2007, **19**, 3-10.

22. M. E. Lines and A. M. Glass, *Principles and applications of ferroelectrics and related materials*, Oxford University Press, Oxford, U.K., 2001.

23. M. E. Welk, A. J. Norquist, F. P. Arnold, C. L. Stern and K. R. Poeppelmeier, *Inorganic Chemistry*, 2002, **41**, 5119-5125.

24. A. Feldhoff, J. Martynczuk and H. H. Wang, *Progress in Solid State Chemistry*, 2007, **35**, 339-353.

25. C. D. Chandler, C. Roger and M. J. Hampdensmith, *Chemical Reviews*, 1993, **93**, 1205-1241.

26. P. J. Gellings and H. J. M. Bouwmeester, eds., *The CRC handbook of solid state electrochemistry*, CRC Press, Boca Raton, FL, 1997.

27. G. Y. Adachi, N. Imanaka and S. Tamura, *Chemical Reviews*, 2002, **102**, 2405-2429.

28. Y. Teraoka, H. M. Zhang, S. Furukawa and N. Yamazoe, *Chemistry Letters*, 1985, 1743-1746.

29. S. C. Singhal, *MRS Bulletin*, 2000, **25**, 16-21.

30. N. Q. Minh, *Journal of the American Ceramic Society*, 1993, **76**, 563-588.

31. M. T. Anderson, J. T. Vaughey and K. R. Poeppelmeier, *Chemistry of Materials*, 1993, **5**, 151-165.

32. J. P. Hodges, S. Short, J. D. Jorgensen, X. Xiong, B. Dabrowski, S. M. Mini and C. W. Kimball, *Journal of Solid State Chemistry*, 2000, **151**, 190-209.

33. B. O. Mysen and P. Richet, eds., *Silicate glasses and melts: properties and structure*, Elsevier, Amsterdam, 2005.

34. D. A. Muller, T. Sorsch, S. Moccio, F. H. Baumann, K. Evans-Lutterodt and G. Timp, *Nature*, 1999, **399**, 758-761.

35. M. T. Bohr, R. S. Chau, T. Ghani and K. Mistry, *IEEE Spectrum*, 2007, **44**, 29-35.

36. D. J. Griffiths, *Introduction to electrodynamics*, Prentice Hall, Upper Saddle River, NJ, 1999.

37. J. D. Jackson, *Classical electrodynamics*, Wiley, New York, 1999.

38. L. Smart and E. Moore, *Solid state chemistry: an introduction*, CRC Press, Boca Raton, FL, 2005.

39. J. Robertson, *Reports on Progress in Physics*, 2006, **69**, 327-396.

40. A. I. Kingon, J. P. Maria and S. K. Streiffer, *Nature*, 2000, **406**, 1032-1038.

41. C. H. Jan, P. Bai, S. Biswas, M. Buehler, Z. P. Chen, G. Curello, S. Gannavaram, W. Hafez, J. He, J. Hicks, U. Jalan, N. Lazo, J. Lin, N. Lindert, C. Litteken, M. Jones, M. Kang, K. Komeyli, A. Mezhiba, S. Naskar, S. Olson, J. Park, R. Parker, L. Pei, I. Post, N. Pradhan, C. Prasad, M. Prince, J. Rizk, G. Sacks, H. Tashiro, D. Towner, C. Tsai, Y. Wang, L. Yang, J. Y. Yeh, J. Yip and K. Mistry, in *IEEE International Electron Devices Meeting*, San Francisco, CA, 2008, pp. 637-640.

42. D. Brassard, D. K. Sarkar, M. A. El Khakani and L. Ouellet, *Journal of Vacuum Science & Technology A*, 2006, **24**, 600-605.

43. P. Broqvist and A. Pasquarello, *Applied Physics Letters*, 2007, **90**, 082907.

44. G. D. Wilk, R. M. Wallace and J. M. Anthony, *Journal of Applied Physics*, 2000, **87**, 484-492.

45. G.-M. Rignanese, in *Materials Fundamentals of Gate Dielectrics*, eds. A. A. Demkov and A. Navrotsky, Springer, Dordrecht, Netherlands, 2005, pp. 249-290.

46. A. Wannagon, N. Mishima, T. Wakasugi, R. Ota and J. Fukunaga, *Journal of the Ceramic Society of Japan*, 1997, **105**, 940-946.

47. G. W. Wallidge, R. Anderson, G. Mountjoy, D. M. Pickup, P. Gunawidjaja, R. J. Newport and M. E. Smith, *Journal of Materials Science*, 2004, **39**, 6743-6755.

48. H. Dislich, *Angewandte Chemie International Edition*, 1971, **10**, 363-370.

49. B. E. Yoldas, *Journal of Materials Science*, 1979, **14**, 1843-1849.

50. M. N. Rahaman, *Ceramic processing and sintering*, Marcel Dekker, New York, 2003.

51. C. J. Brinker and G. W. Scherer, *Sol-gel science: the physics and chemistry of sol-gel processing*, Academic Press, Boston, 1990.

52. K. Jiang, A. Zakutayev, J. Stowers, M. D. Anderson, J. Tate, D. H. McIntyre, D. C. Johnson and D. A. Keszler, *Solid State Sciences*, 2009, **11**, 1692-1699.

53. V. K. Pecharsky, P. Y. Zavalij and SpringerLink (Online service), Springer, New York, 2009, p. 741.

54. R. L. Opila, G. D. Wilk, M. A. Alam, R. B. van Dover and B. W. Busch, *Applied Physics Letters*, 2002, **81**, 1788-1790.

55. M. J. Guittet, J. P. Crocombette and M. Gautier-Soyer, *Physical Review B*, 2001, **63**, 125117.

56. D. Briggs, *Surface analysis of polymers by XPS and static SIMS*, Cambridge University Press, Cambridge, U.K., 1998.

57. F. de Groot and A. Kotani, *Core level spectroscopy of solids*, CRC Press, Boca Raton, FL, 2008.

58. D. A. Shirley, *Physical Review A*, 1973, **7**, 1520-1528.

59. D. A. Shirley, *Chemical Physics Letters*, 1972, **17**, 312-315.

60. J. C. Riviere and S. Myhra, eds., *Handbook of surface and interface analysis: methods for problem-solving*, Marcel Dekker, New York, 1998.

61. P. A. W. van der Heide, *Surface Science*, 2001, **490**, L619-L626.

62. S. Hufner, *Photoelectron spectroscopy: principles and applications*, Springer, Berlin, 2003.

63. C. J. Powell, A. Jablonski, I. S. Tilinin, S. Tanuma and D. R. Penn, *Journal of Electron Spectroscopy and Related Phenomena*, 1999, **99**, 1-15.

64. A. Jablonski and C. J. Powell, *Journal of Electron Spectroscopy and Related Phenomena*, 1999, **100**, 137-160.

65. C. Kittel, *Introduction to solid state physics*, Wiley, Hoboken, NJ, 2005.

66. M. T. Anthony and M. P. Seah, *Surface and Interface Analysis*, 1984, **6**, 95-106.

67. M. P. Seah, *Surface and Interface Analysis*, 1989, **14**, 488-488.

68. M. P. Seah, L. S. Gilmore and G. Beamson, *Surface and Interface Analysis*, 1998, **26**, 642-649.

69. M. P. Seah, I. S. Gilmore and S. J. Spencer, *Applied Surface Science*, 1999, **144-45**, 178-182.

70. J. F. Watts and J. Wolstenholme, *An introduction to surface analysis by XPS and AES*, Wiley, Chichester, U.K., 2003.

71. T. L. Barr and S. Seal, *Journal of Vacuum Science & Technology A*, 1995, **13**, 1239-1246.

72. J. G. Jenkin, R. C. G. Leckey and J. Liesegang, *Journal of Electron Spectroscopy and Related Phenomena*, 1977, **12**, 1-35.

73. A. P. Grosvenor, R. G. Cavell and A. Mar, *Journal of Solid State Chemistry*, 2008, **181**, 2549-2558.

74. K. Siegbahn, *Philosophical Transactions of the Royal Society of London, Series A: Mathematical, Physical and Engineering Sciences*, 1970, **268**, 33-57.

75. P. A. W. van der Heide, *Journal of Electron Spectroscopy and Related Phenomena*, 2006, **151**, 79-91.

76. T. D. Thomas and P. Weightman, *Physical Review B*, 1986, **33**, 5406-5413.

77. G. Moretti, *Journal of Electron Spectroscopy and Related Phenomena*, 1998, **95**, 95-144.

78. R. D. Leapman, L. A. Grunes and P. L. Fejes, *Physical Review B*, 1982, **26**, 614-635.

79. A. Nilsson, R. E. Palmer, H. Tillborg, B. Hernnas, R. J. Guest and N. Martensson, *Physical Review Letters*, 1992, **68**, 982-985.

80. P. E. R. Blanchard, A. P. Grosvenor, R. G. Cavell and A. Mar, *Chemistry of Materials*, 2008, **20**, 7081-7088.

81. P. E. R. Blanchard, A. P. Grosvenor, R. G. Cavell and A. Mar, *Journal of Materials Chemistry*, 2009, **19**, 6015-6022.

82. M. Dalzell, ed., *Canadian Light Source Activity Report 2009*, Canadian Light Source, Saskatoon, Canada, 2010.

83. R. Prins and D. C. Koningsberger, eds., *X-ray absorption: principles, applications, techniques of EXAFS, SEXAFS, and XANES*, Wiley, New York, 1988.

84. F. de Groot, *Chemical Reviews*, 2001, **101**, 1779-1808.

85. A. E. Russell and A. Rose, *Chemical Reviews*, 2004, **104**, 4613-4635.

86. D. E. Ramaker and D. C. Koningsberger, *Physical Chemistry Chemical Physics*, 2010, **12**, 5514-5534.

87. A. Thompson, D. Attwood, E. Gullikson, M. Howells, K.-J. Kim, J. Kirz, J. Kortright, I. Lindau, P. Pianetta, A. Robinson, J. Scofield, J. Underwood, D. Vaughan, G. Williams and H. Winick, *X-ray data booklet*, Lawrence Berkeley National Laboratory, Berkeley, CA, 2009.

88. F. M. F. de Groot, *Journal of Electron Spectroscopy and Related Phenomena*, 1994, **67**, 529-622.

89. A. J. Achkar, T. Z. Regier, H. Wadati, Y. J. Kim, H. Zhang and D. G. Hawthorn, *Physical Review B*, 2011, **83**.

90. G. Bunker, *Introduction to XAFS: a practical guide to X-ray absorption fine structure spectroscopy*, Cambridge University Press, Cambridge, U.K., 2010.

91. J. G. Chen, *Surface Science Reports*, 1997, **30**, 1-152.

92. K. Nakamura, K. Hagiwara, K. Hikasa, H. Murayama, M. Tanabashi, T. Watari, C. Amsler, M. Antonelli, D. M. Asner, H. Baer, H. R. Band, R. M. Barnett, T. Basaglia, E. Bergren, J. Beringer, G. Bernardi, W. Bertl, H. Bichsel, O. Biebel, E. Blucher, S. Blusk, R. N. Cahn, M. Carena, A. Ceccucci, D. Chakraborty, M. C. Chen, R. S. Chivukula, G. Cowan, O. Dahl, G. D'Ambrosio, T. Damour, D. de Florian, A. de Gouvea, T. DeGrand, G. Dissertori, B. Dobrescu, M. Doser, M. Drees, D. A. Edwards, S. Eidelman, J. Erler, V. V. Ezhela, W. Fetscher, B. D. Fields, B. Foster, T. K. Gaisser, L. Garren, H. J. Gerber, G. Gerbier, T. Gherghetta, C. F. Giudice, S. Golwala, M. Goodman, C. Grab, A. V. Gritsan, J. F. Grivaz, D. E. Groom, M. Grunewald, A. Gurtu, T. Gutsche, H. E. Haber, C. Hagmann, K. G. Hayes, M. Heffner, B. Heltsley, J. J. Hernandez-Rey, A. Hocker, J. Holder, J. Huston, J. D. Jackson, K. F. Johnson, T. Junk, A. Karle, D. Karlen, B. Kayser, D. Kirkby, S. R. Klein, C. Kolda, R. V. Kowalewski, B. Krusche, Y. V. Kuyanov, Y. Kwon, O. Lahav, P. Langacker, A. Liddle, Z. Ligeti, C. J. Lin, T. M. Liss, L. Littenberg, K. S. Lugovsky, S. B. Lugovsky, J. Lys, H. Mahlke, T. Mannel, A. V. Manohar, W. J. Marciano, A. D. Martin, A. Masoni, D. Milstead, R. Miquel, K. Monig, M. Narain, P. Nason, S. Navas, P. Nevski, Y. Nir, K. A. Olive, L. Pape, C. Patrignani, J. A. Peacock, S. T. Petcov, A. Piepke, G. Punzi, A. Quadt, S. Raby, G. Raffelt, B. N. Ratcliff, P. Richardson, S. Roesler, S. Rolli, A. Romaniouk, L. J. Rosenberg, J. L. Rosner, C. T. Sachrajda, Y. Sakai, G. P. Salam, S. Sarkar, F. Sauli, O. Schneider, K. Scholberg, D. Scott, W. G. Seligman, M. H. Shaevitz, M. Silari, T. Sjostrand, J. G. Smith, G. F. Smoot, S. Spanier, H. Spieler, A. Stahl, T. Stanev, S. L. Stone, T. Sumiyoshi, M. J. Syphers, J. Terning, M. Titov, N. P. Tkachenko, N. A. Tornqvist, D. Tovey, T. G. Trippe, G. Valencia, K. van Bibber, G. Venanzoni, M. G. Vincter, P. Vogel, A. Vogt, W. Walkowiak, C. W. Walter, D. R. Ward, B. R. Webber, G. Weiglein, E. J. Weinberg, J. D. Wells, A. Wheeler, L. R. Wiencke, C. G. Wohl, L. Wolfenstein, J. Womersley, C. L. Woody, R. L. Workman, A. Yamamoto, W. M. Yao, O. V. Zenin, J. Zhang, R. Y. Zhu, P. A. Zyla, G. Harper, V. S. Lugovsky and P. Schaffner, *Journal of Physics G: Nuclear and Particle Physics*, 2010, **37**, 1-1422.

93. L. Troger, D. Arvanitis, H. Rabus, L. Wenzel and K. Baberschke, *Physical Review B*, 1990, **41**, 7297-7300.

94. S. Eisebitt, T. Boske, J. E. Rubensson and W. Eberhardt, *Physical Review B*, 1993, **47**, 14103-14109.

95. M. Kasrai, W. N. Lennard, R. W. Brunner, G. M. Bancroft, J. A. Bardwell and K. H. Tan, *Applied Surface Science*, 1996, **99**, 303-312.

96. R. Nakajima, J. Stohr and Y. U. Idzerda, *Physical Review B*, 1999, **59**, 6421-6429.

97. J. Goulon, C. Goulonginet, R. Cortes and J. M. Dubois, *Journal de Physique*, 1982, **43**, 539-548.

98. A. Manceau, M. A. Marcus and N. Tamura, *Reviews in Mineralogy and Geochemistry*, 2002, **49**, 341-428.

99. R. Castaner and C. Prieto, *Journal de Physique III*, 1997, **7**, 337-349.

100. L. Troger, D. Arvanitis, K. Baberschke, H. Michaelis, U. Grimm and E. Zschech, *Physical Review B*, 1992, **46**, 3283-3289.

101. C. G. Barkla and C. A. Sadler, *Nature*, 1908, **78**, 245-245.

102. L. A. Grunes, *Physical Review B*, 1983, **27**, 2111-2131.

103. D. Cabaret, Y. Joly, H. Renevier and C. R. Natoli, *Journal of Synchrotron Radiation*, 1999, **6**, 258-260.

104. F. de Groot, G. Vanko and P. Glatzel, *Journal of Physics: Condensed Matter*, 2009, **21**, 104207.

105. M. Wilke, F. Farges, P. E. Petit, G. E. Brown and F. Martin, *American Mineralogist*, 2001, **86**, 714-730.

106. F. Farges, G. E. Brown and J. J. Rehr, *Physical Review B*, 1997, **56**, 1809-1819.

107. G. A. Waychunas, M. J. Apted and G. E. Brown, *Physics and Chemistry of Minerals*, 1983, **10**, 1-9.

108. G. A. Waychunas, *American Mineralogist*, 1987, **72**, 89-101.

109. F. Farges, *Journal of Non-Crystalline Solids*, 1996, **204**, 53-64.

110. F. Farges, *American Mineralogist*, 1997, **82**, 36-43.

111. A. P. Grosvenor and J. E. Greedan, *Journal of Physical Chemistry C*, 2009, **113**, 11366-11372.

112. M. W. Gaultois, J. E. Greedan and A. P. Grosvenor, *Journal of Electron Spectroscopy and Related Phenomena*, 2011, **184**, 192-195.

113. M. Schmidt, M. Hofmann and S. J. Campbell, *Journal of Physics: Condensed Matter*, 2003, **15**, 8691-8701.

114. A. L. Allred and E. G. Rochow, *Journal of Inorganic and Nuclear Chemistry*, 1958, **5**, 264-268.

115. H. H. Wang, C. Tablet, A. Feldhoff and J. Caro, *Advanced Materials*, 2005, **17**, 1785-1788.

116. D. R. Mullins, S. H. Overbury and D. R. Huntley, *Surface Science*, 1998, **409**, 307-319.

117. A. Feldhoff, J. Martynczuk, M. Arnold, M. Myndyk, I. Bergmann, V. Sepelak, W. Gruner, U. Vogt, A. Hahnel and J. Woltersdorf, *Journal of Solid State Chemistry*, 2009, **182**, 2961-2971.

118. T. J. B. Holland and S. A. T. Redfern, *Mineralogical Magazine*, 1997, **61**, 65-77.

119. K. Momma and F. Izumi, *Journal of Applied Crystallography*, 2008, **41**, 653-658.

120. T. Regier, J. Krochak, T. K. Sham, Y. F. Hu, J. Thompson and R. I. R. Blyth, *Nuclear Instruments & Methods in Physics Research Section A: Accelerators Spectrometers Detectors and Associated Equipment*, 2007, **582**, 93-95.

121. B. K. Woo, W. Chen, A. G. Joly and R. Sammynaiken, *Journal of Physical Chemistry C*, 2008, **112**, 14292-14296.

122. A. P. Grosvenor, F. Ramezanipour, S. Derakhshan, C. Maunders, G. A. Botton and J. E. Greedan, *Journal of Materials Chemistry*, 2009, **19**, 9213-9220.

123. B. Ravel and M. Newville, *Journal of Synchrotron Radiation*, 2005, **12**, 537-541.

124. A. P. Grosvenor, S. D. Wik, R. G. Cavell and A. Mar, *Inorganic Chemistry*, 2005, **44**, 8988-8998.

125. R. L. Martin and D. A. Shirley, *Journal of Chemical Physics*, 1976, **64**, 3685-3689.

126. S. McIntosh, J. F. Vente, W. G. Haije, D. H. A. Blank and H. J. M. Bouwmeester, *Chemistry of Materials*, 2006, **18**, 2187-2193.

127. T. Itoh, Y. Nishida, A. Tomita, Y. Fujie, N. Kitamura, Y. Idemoto, K. Osaka, I. Hirosawa and N. Igawa, *Solid State Communications*, 2009, **149**, 41-44.

128. R. D. Shannon, *Acta Crystallographica, Section A: Crystal Physics, Diffraction, Theoretical and General Crystallography*, 1976, **32**, 751-767.

129. H. G. Schnering and R. Hoppe, *Zeitschrift fur Anorganische und Allgemeine Chemie*, 1961, **312**, 87-98.

130. X. B. Yu, X. L. Xu, C. L. Zhou, J. F. Tang, X. D. Peng and S. P. Yang, *Materials Research Bulletin*, 2006, **41**, 1578-1583.

131. R. G. Shulman, Y. Yafet, P. Eisenberger and W. E. Blumberg, *Proceedings of the National Academy of Sciences of the United States of America*, 1976, **73**, 1384-1388.

132. O. Haas, U. F. Vogt, C. Soltmann, A. Braun, W. S. Yoon, X. Q. Yang and T. Graule, *Materials Research Bulletin*, 2009, **44**, 1397-1404.

133. A. Juhin, F. de Groot, G. Vanko, M. Calandra and C. Brouder, *Physical Review B*, 2010, **81**, 115115.

134. J. E. Hahn, R. A. Scott, K. O. Hodgson, S. Doniach, S. R. Desjardins and E. I. Solomon, *Chemical Physics Letters*, 1982, **88**, 595-598.

135. D. Cabaret, A. Bordage, A. Juhin, M. Arfaoui and E. Gaudry, *Physical Chemistry Chemical Physics*, 2010, **12**, 5619-5633.

136. T. E. Westre, P. Kennepohl, J. G. DeWitt, B. Hedman, K. O. Hodgson and E. I. Solomon, *Journal of the American Chemical Society*, 1997, **119**, 6297-6314.

137. P. E. Petit, F. Farges, M. Wilke and V. A. Sole, *Journal of Synchrotron Radiation*, 2001, **8**, 952-954.

138. T. Yamamoto, *X-Ray Spectrometry*, 2008, **37**, 572-584.

139. C. Brouder, *Journal of Physics: Condensed Matter*, 1990, **2**, 701-738.

140. J. Wong, F. W. Lytle, R. P. Messmer and D. H. Maylotte, *Physical Review B*, 1984, **30**, 5596-5610.

141. J. A. van Bokhoven, T. Nabi, H. Sambe, D. E. Ramaker and D. C. Koningsberger, *Journal of Physics: Condensed Matter*, 2001, **13**, 10247-10260.

142. C. Weigel, G. Calas, L. Cormier, L. Galoisy and G. S. Henderson, *Journal of Physics: Condensed Matter*, 2008, **20**, 135219.

143. I. S. Elfimov, V. I. Anisimov and G. A. Sawatzky, *Physical Review Letters*, 1999, **82**, 4264-4267.

144. R. le Toquin, W. Paulus, A. Cousson, C. Prestipino and C. Lamberti, *Journal of the American Chemical Society*, 2006, **128**, 13161-13174.

145. G. Berlier, G. Spoto, S. Bordiga, G. Ricchiardi, P. Fisicaro, A. Zecchina, I. Rossetti, E. Selli, L. Forni, E. Giamello and C. Lamberti, *Journal of Catalysis*, 2002, **208**, 64-82.

146. J. J. Rehr and R. C. Albers, *Reviews of Modern Physics*, 2000, **72**, 621-654.

147. G. van der Laan and I. W. Kirkman, *Journal of Physics: Condensed Matter*, 1992, **4**, 4189-4204.

148. M. Abbate, F. M. F. de Groot, J. C. Fuggle, A. Fujimori, O. Strebel, F. Lopez, M. Domke, G. Kaindl, G. A. Sawatzky, M. Takano, Y. Takeda, H. Eisaki and S. Uchida, *Physical Review B*, 1992, **46**, 4511-4519.

149. J. P. Crocombette, M. Pollak, F. Jollet, N. Thromat and M. Gautier-Soyer, *Physical Review B*, 1995, **52**, 3143-3150.

150. H. J. Lee, G. Kim, J. S. Kang, B. Dabrowski, S. W. Han, S. S. Lee, C. Hwang, M. C. Jung, H. J. Shin, H. G. Lee, J. Y. Kim and B. I. Min, *Journal of Applied Physics*, 2007, **101**, 09G523.

151. C. L. Chen, C. L. Dong, S. M. Rao, G. Chern, M. C. Chen, M. K. Wu and C. L. Chang, *Journal of Physics: Condensed Matter*, 2008, **20**, 255236.

152. F. M. F. de Groot, M. Grioni, J. C. Fuggle, J. Ghijsen, G. A. Sawatzky and H. Petersen, *Physical Review B*, 1989, **40**, 5715-5723.

153. L. Karvonen, M. Valkeapaa, R. S. Liu, J. M. Chen, H. Yamauchi and M. Karppinen, *Chemistry of Materials*, 2010, **22**, 70-76.

154. Z. Y. Wu, M. Benfatto, M. Pedio, R. Cimino, S. Mobilio, S. R. Barman, K. Maiti and D. D. Sarma, *Physical Review B*, 1997, **56**, 2228-2233.

155. F. Farges, S. Rossano, Y. Lefrere, M. Wilke and G. E. Brown, *Physica Scripta*, 2005, **T115**, 957-959.

156. L. Pauling, *The nature of the chemical bond and the structure of molecules and crystals: an introduction to modern structural chemistry*, Cornell University Press, Ithaca, NY, 1960.

157. R. T. Sanderson, *Journal of the American Chemical Society*, 1983, **105**, 2259-2261.

158. T. Kazahaya and M. Hirose, *Japanese Journal of Applied Physics, Part 2: Letters & Express Letters*, 1986, **25**, L75-L77.

159. E. Talik, A. Novosselov, M. Kulpa and A. Pajaczkowska, *Journal of Alloys and Compounds*, 2001, **321**, 24-26.

160. J. C. Slater, *Physical Review*, 1930, **36**, 57-64.

161. P. A. W. van der Heide, *Surface and Interface Analysis*, 2002, **33**, 414-425.

162. A. P. Grosvenor, B. A. Kobe and N. S. McIntyre, *Surface Science*, 2004, **572**, 217-227.

163. G. Mountjoy, D. M. Pickup, R. Anderson, G. W. Wallidge, M. A. Holland, R. J. Newport and M. E. Smith, *Physical Chemistry Chemical Physics*, 2000, **2**, 2455-2460.

164. K. Kamiya and S. Sakka, *Journal of Materials Science*, 1980, **15**, 2937-2939.

165. T. Hayashi, T. Yamada and H. Saito, *Journal of Materials Science*, 1983, **18**, 3137-3142.

166. K. Kamiya, S. Sakka and Y. Tatemichi, *Journal of Materials Science*, 1980, **15**, 1765-1771.

167. D. Poitras, S. Larouche and L. Martinu, *Applied Optics*, 2002, **41**, 5249-5255.

168. G. Mountjoy, M. A. Holland, G. W. Wallidge, P. Gunawidjaja, M. E. Smith, D. M. Pickup and R. J. Newport, *Journal of Physical Chemistry B*, 2003, **107**, 7557-7566.

169. R. J. Davis and Z. F. Liu, *Chemistry of Materials*, 1997, **9**, 2311-2324.

170. X. Z. Fu, L. A. Clark, Q. Yang and M. A. Anderson, *Environmental Science and Technology*, 1996, **30**, 647-653.

171. J. B. Miller, S. T. Johnston and E. I. Ko, *Journal of Catalysis*, 1994, **150**, 311-320.

172. J. A. Mejias, V. M. Jimenez, G. Lassaletta, A. Fernandez, J. P. Espinos and A. R. Gonzalez-Elipe, *Journal of Physical Chemistry*, 1996, **100**, 16255-16262.

173. G. Lassaletta, A. Fernandez, J. P. Espinos and A. R. Gonzalez-Elipe, *Journal of Physical Chemistry*, 1995, **99**, 1484-1490.

174. V. M. Jimenez, G. Lassaletta, A. Fernandez, J. P. Espinos and A. R. Gonzalez-Elipe, *Surface and Interface Analysis*, 1997, **25**, 292-294.

175. G. Lucovsky, Y. Zhang, G. B. Rayner, G. Appel, H. Ade and J. L. Whitten, *Journal of Vacuum Science & Technology B*, 2002, **20**, 1739-1747.

176. J. F. Damlencourt, O. Renault, D. Samour, A. M. Papon, C. Leroux, F. Martin, S. Marthon, M. N. Semeria and X. Garros, *Solid-State Electronics*, 2003, **47**, 1613-1616.

177. N. Barrett, O. Renault, J. F. Damlencourt and F. Martin, *Journal of Applied Physics*, 2004, **96**, 6362-6369.

178. R. P. Netterfield, P. J. Martin, C. G. Pacey, W. G. Sainty, D. R. McKenzie and G. Auchterlonie, *Journal of Applied Physics*, 1989, **66**, 1805-1809.

179. M. D. Ulrich, J. G. Hong, J. E. Rowe, G. Lucovsky, A. S. Y. Chan and T. E. Madey, *Journal of Vacuum Science & Technology B*, 2003, **21**, 1777-1782.

180. B. E. Yoldas, *Journal of Non-Crystalline Solids*, 1980, **38-9**, 81-86.

181. R. Anderson, G. Mountjoy, M. E. Smith and R. J. Newport, *Journal of Non-Crystalline Solids*, 1998, **232**, 72-79.

182. U. Wellbrock, W. Beier and G. H. Frischat, *Journal of Non-Crystalline Solids*, 1992, **147**, 350-355.

183. G. S. Henderson and M. E. Fleet, *Journal of Non-Crystalline Solids*, 1997, **211**, 214-221.

184. L. A. O'Dell, P. N. Gunawidjaja, M. A. Holland, G. Mountjoy, D. M. Pickup, R. J. Newport and M. E. Smith, *Solid State Nuclear Magnetic Resonance*, 2008, **33**, 16-24.

185. P. N. Gunawidjaja, M. A. Holland, G. Mountjoy, D. M. Pickup, R. J. Newport and M. E. Smith, *Solid State Nuclear Magnetic Resonance*, 2003, **23**, 88-106.

186. G. Mountjoy, R. Anderson, R. J. Newport and M. E. Smith, *Journal of Physics: Condensed Matter*, 2000, **12**, 3505-3519.

187. G. Mountjoy, D. M. Pickup, G. W. Wallidge, R. Anderson, J. M. Cole, R. J. Newport and M. E. Smith, *Chemistry of Materials*, 1999, **11**, 1253-1258.

188. G. S. Henderson, X. Liu and M. E. Fleet, *Physics and Chemistry of Minerals*, 2002, **29**, 32-42.

189. G. S. Henderson, X. Y. Liu and M. E. Fleet, *Mineralogical Magazine*, 2003, **67**, 597-607.

190. L. Q. Zhu, N. Barrett, P. Jegou, F. Martin, C. Leroux, E. Martinez, H. Grampeix, O. Renault and A. Chabli, *Journal of Applied Physics*, 2009, **105**, 024102.

191. A. Y. Stakheev, E. S. Shpiro and J. Apijok, *Journal of Physical Chemistry*, 1993, **97**, 5668-5672.

192. W. B. Kim, S. H. Choi and J. S. Lee, *Journal of Physical Chemistry B*, 2000, **104**, 8670-8678.

193. A. P. Grosvenor, R. G. Cavell and A. Mar, *Journal of Solid State Chemistry*, 2007, **180**, 2702-2712.

194. F. Farges, G. E. Brown and J. J. Rehr, *Geochimica et Cosmochimica Acta*, 1996, **60**, 3023-3038.

195. T. Yamamoto, T. Mizoguchi and I. Tanaka, *Physical Review B*, 2005, **71**, 245113.

196. G. N. Vayssilov, *Catalysis Reviews - Science and Engineering*, 1997, **39**, 209-251.

197. D. M. Pickup, G. Mountjoy, G. W. Wallidge, R. Anderson, J. M. Cole, R. J. Newport and M. E. Smith, *Journal of Materials Chemistry*, 1999, **9**, 1299-1305.

198. D. M. Pickup, G. Mountjoy, M. A. Holland, G. W. Wallidge, R. J. Newport and M. E. Smith, *Journal of Physics: Condensed Matter*, 2000, **12**, 9751-9760.

199. M. F. Best and R. A. Condrate, *Journal of Materials Science Letters*, 1985, **4**, 994-998.

200. G. S. Henderson and M. E. Fleet, *Canadian Mineralogist*, 1995, **33**, 399-408.

201. D. Li, G. M. Bancroft, M. Kasrai, M. E. Fleet, X. H. Feng and K. H. Tan, *American Mineralogist*, 1994, **79**, 785-788.

202. M. A. Villegas, A. de Pablos and J. M. Fernandez-Navarro, *Glass Technology*, 1994, **35**, 276-280.

203. W. Beier, A. A. Goktas and G. H. Frischat, *Journal of the American Ceramic Society*, 1986, **69**, C148-C150.

204. A. Wannagon, N. Mishima, R. Ota, T. Wakasugi and J. Fukunaga, *Materials Science Research International*, 1997, **3**, 210-215.

205. B. E. Yoldas, *Journal of Materials Science*, 1977, **12**, 1203-1208.

206. J. Livage, M. Henry and C. Sanchez, *Progress in Solid State Chemistry*, 1988, **18**, 259-341.

207. G. S. Henderson and J. C. St-Amour, *Chemical Geology*, 2004, **213**, 31-40.

208. S. Y. Savrasov and D. Y. Savrasov, *Physical Review B*, 1992, **46**, 12181-12195.

209. S. Y. Savrasov, *Physical Review B*, 1996, **54**, 16470-16486.

210. S. Y. Savrasov, *Zeitschrift fur Kristallographie*, 2005, **220**, 555-557.

211. J. P. Perdew and Y. Wang, *Physical Review B*, 1992, **45**, 13244-13249.

212. A. Sandell, B. Sanyal, L. E. Walle, P. Uvdal and A. Borg, *Journal of Electron Spectroscopy and Related Phenomena*, 2011, **183**, 107-113.

213. G. M. Rignanese, X. Rocquefelte, X. Gonze and A. Pasquarello, *International Journal of Quantum Chemistry*, 2005, **101**, 793-801.

214. O. Jepsen and O. K. Andersen, *Solid State Communications*, 1971, **9**, 1763-1767.

215. O. Jepsen and O. K. Andersen, *Physical Review B*, 1984, **29**, 5965-5965.

216. R. J. Finch, J. M. Hanchar, P. W. O. Hoskin and P. C. Burns, *American Mineralogist*, 2001, **86**, 681-689.

217. L. Gracia, A. Beltran and D. Errandonea, *Physical Review B*, 2009, **80**, 094105.

218. F. Farges, G. E. Brown, A. Navrotsky, H. Gan and J. J. Rehr, *Geochimica et Cosmochimica Acta*, 1996, **60**, 3039-3053.

219. D. M. Pickup, G. Mountjoy, G. W. Wallidge, R. J. Newport and M. E. Smith, *Physical Chemistry Chemical Physics*, 1999, **1**, 2527-2533.

220. P. S. Bagus, F. Illas, G. Pacchioni and F. Parmigiani, *Journal of Electron Spectroscopy and Related Phenomena*, 1999, **100**, 215-236.

221. R. J. Cole, D. A. C. Gregory and P. Weightman, *Physical Review B*, 1994, **49**, 5657-5661.

222. C. M. Pradier, C. Hinnen, K. Jansson, L. Dahl, M. Nygren and A. Flodstrom, *Journal of Materials Science*, 1998, **33**, 3187-3191.

223. E. J. Little and M. M. Jones, *Journal of Chemical Education*, 1960, **37**, 231-233.

224. J. P. Crocombette and F. Jollet, *Journal of Physics: Condensed Matter*, 1994, **6**, 10811-10821.

225. T. Hoche, P. Ohle, R. Keding, C. Russel, P. A. Van Aken, R. Schneider, H. J. Kleebe, X. Q. Wang, A. J. Jacobson and S. Stemmer, *Philosophical Magazine*, 2003, **83**, 165-178.

226. F. M. F. de Groot, J. C. Fuggle, B. T. Thole and G. A. Sawatzky, *Physical Review B*, 1990, **42**, 5459-5468.

227. F. De Groot, *Coordination Chemistry Reviews*, 2005, **249**, 31-63.

228. J. C. Fuggle and S. F. Alvarado, *Physical Review A*, 1980, **22**, 1615-1624.

229. Y. Iguchi, *Science of Light*, 1977, **26**, 161-181.

230. L. A. J. Garvie and P. R. Buseck, *American Mineralogist*, 1999, **84**, 946-964.

231. P. L. Hansen, R. Brydson and D. W. McComb, *Microscopy Microanalysis Microstructures*, 1992, **3**, 213-219.

232. D. Li, G. M. Bancroft, M. Kasrai, M. E. Fleet, X. H. Feng, K. H. Tan and B. X. Yang, *Solid State Communications*, 1993, **87**, 613-617.

233. L. A. Grunes, R. D. Leapman, C. N. Wilker, R. Hoffmann and A. B. Kunz, *Physical Review B*, 1982, **25**, 7157-7173.

234. H. Kurata, E. Lefevre, C. Colliex and R. Brydson, *Physical Review B*, 1993, **47**, 13763-13768.

235. C. D. Wagner, *Faraday Discussions of the Chemical Society*, 1975, **60**, 291-300.

236. T. D. Thomas, *Journal of Electron Spectroscopy and Related Phenomena*, 1980, **20**, 117-125.

237. N. D. Lang and A. R. Williams, *Physical Review B*, 1979, **20**, 1369-1376.

238. G. Hohlneicher, H. Pulm and H. J. Freund, *Journal of Electron Spectroscopy and Related Phenomena*, 1985, **37**, 209-224.

239. R. J. Cole, P. Weightman and J. A. D. Matthew, *Journal of Electron Spectroscopy and Related Phenomena*, 2003, **133**, 47-53.

240. P. S. Bagus, A. Wieckowski and H. Freund, *Chemical Physics Letters*, 2006, **420**, 42-46.

241. M. Satta and G. Moretti, *Journal of Electron Spectroscopy and Related Phenomena*, 2010, **178**, 123-127.

242. A. P. Grosvenor, B. A. Kobe, M. C. Biesinger and N. S. McIntyre, *Surface and Interface Analysis*, 2004, **36**, 1564-1574.

243. G. Silversmit, D. Depla, H. Poelman, G. B. Marin and R. De Gryse, *Journal of Electron Spectroscopy and Related Phenomena*, 2004, **135**, 167-175.

244. M. C. Biesinger, B. P. Payne, A. P. Grosvenor, L. W. M. Lau, A. R. Gerson and R. S. C. Smart, *Applied Surface Science*, 2011, **257**, 2717-2730.

245. A. F. Gaudette, A. W. Burns, J. R. Hayes, M. C. Smith, R. H. Bowker, T. Seda and M. E. Bussell, *Journal of Catalysis*, 2010, **272**, 18-27.

246. J. R. Hayes, R. H. Bowker, A. F. Gaudette, M. C. Smith, C. E. Moak, C. Y. Nam, T. K. Pratum and M. E. Bussell, *Journal of Catalysis*, 2010, **276**, 249-258.

247. S. T. Oyama, T. Gott, H. Zhao and Y.-K. Lee, *Catalysis Today*, 2009, **143**, 94-107.

248. J. Martynczuk, M. Arnold, H. Wang, J. Caro and A. Feldhoff, *Advanced Materials*, 2007, **19**, 2134-2140.

249. A. Feldhoff, M. Arnold, J. Martynczuk, T. M. Gesing and H. Wang, *Solid State Sciences*, 2008, **10**, 689-701.

250. Z. P. Shao, W. S. Yang, Y. Cong, H. Dong, J. H. Tong and G. X. Xiong, *Journal of Membrane Science*, 2000, **172**, 177-188.

251. P. Bouvier, E. Djurado, G. Lucazeau and T. le Bihan, *Physical Review B*, 2000, **62**, 8731-8737.

252. C. J. Howard, E. H. Kisi, R. B. Roberts and R. J. Hill, *Journal of the American Ceramic Society*, 1990, **73**, 2828-2833.

253. B. Bondars, G. Heidemane, J. Grabis, K. Laschke, H. Boysen, J. Schneider and F. Frey, *Journal of Materials Science*, 1995, **30**, 1621-1625.

254. R. E. Newnham, *Journal of the American Ceramic Society*, 1967, **50**, 216.

255. A. Yamamoto, T. Yamada, H. Ikawa, O. Fukunaga, K. Tanaka and F. Marumo, *Acta Crystallographica Section C: Crystal Structure Communications*, 1991, **47**, 1588-1591.

256. R. Christoffersen and P. K. Davies, *Journal of the American Ceramic Society*, 1992, **75**, 563-569.

257. W. L. Konijnendijk, *The structure of borosilicate glasses*, Centrex, Eindhoven, Netherlands, 1975.

258. D. Manara, A. Grandjean and D. R. Neuville, *American Mineralogist*, 2009, **94**, 777-784.

259. D. R. Neuville, G. S. Henderson, L. Cormier and D. Massiot, *American Mineralogist*, 2010, **95**, 1580-1589.

260. G. Calas, G. E. Brown, G. A. Waychunas and J. Petiau, *Physics and Chemistry of Minerals*, 1987, **15**, 19-29-29.

261. D. R. Neuville, L. Cormier, J. Roux, G. S. Henderson, D. de Ligny and A.-M. Flank, *AIP Conference Proceedings*, 2007, **882**, 419-421.

262. D. R. Neuville, L. Cormier and D. Massiot, *Chemical Geology*, 2006, **229**, 173-185.

263. G. S. Henderson, D. R. Neuville and L. Cormier, *Chemical Geology*, 2009, **259**, 54-62.

264. D. E. Li, G. M. Bancroft, M. E. Fleet, X. H. Feng and Y. Pan, *American Mineralogist*, 1995, **80**, 432-440.

265. D. Li, G. M. Bancroft, M. E. Fleet, P. C. Hess and Z. F. Yin, *American Mineralogist*, 1995, **80**, 873-877.

266. D. Li, G. M. Bancroft, M. E. Fleet and X. H. Feng, *Physics and Chemistry of Minerals*, 1995, **22**, 115-122-122.

267. M. E. Fleet and S. Muthupari, *Journal of Non-Crystalline Solids*, 1999, **255**, 233-241.

268. M. E. Fleet and S. Muthupari, *American Mineralogist*, 2000, **85**, 1009-1021.